The Dissertation Committee for Pisitpol Chirapongsananurak
Certifies that this is the approved version of the following dissertation:

Distribution Circuit Multi-Time-Scale Simulation Tool for Wind Turbine and Photovoltaic Integration Analysis

Committee:

Surya Santoso, Supervisor

Ross Baldick

Gary A. Hallock

Alexis Kwasinski

Raul G. Longoria

Distribution Circuit Multi-Time-Scale Simulation Tool for Wind Turbine and Photovoltaic Integration Analysis

by

Pisitpol Chirapongsananurak, B.E.; M.E.

DISSERTATION

Presented to the Faculty of the Graduate School of
The University of Texas at Austin
in Partial Fulfillment
of the Requirements
for the Degree of

DOCTOR OF PHILOSOPHY

THE UNIVERSITY OF TEXAS AT AUSTIN

May 2016

Dedicated to my beloved parents and grandparents
for their unconditional love and endless support.

Acknowledgments

First and foremost, I would like to express my deepest gratitude to Dr. Surya Santoso, my supervisor, for his guidance and direction throughout my PhD program. I have a heartfelt appreciation for all advice he gave me since the first time we met. I would like to thank him for giving me the valuable opportunity to work with him since my first semester. I would also like to acknowledge him for appointing me as a teaching assistant and research assistant during my PhD studies. Without his continued support and guidance, I could not have completed this dissertation.

I would like to offer my sincerest thanks to my dissertation committee members: Dr. Ross Baldick, Dr. Gary Hallock, Dr. Alexis Kwasinski, and Dr. Raul Longoria for agreeing to serve in my committee and for their valuable guidance and input throughout my PhD studies. I would also like to express my acknowledgment to Dr. Mircea Driga, my qualifying committee member, for his valuable comments and suggestions during my qualifying exam.

I wish to extend my warmest thanks to the staff members in the Electrical and Computer Engineering Department. My deepest thanks goes to Melanie Gulick and Melody Singleton for their assistance and advice throughout my PhD process. They always understand the difficulties graduate students encounter throughout the studies and always do their best to help.

I am deeply grateful to my fellow colleagues for their help and advice in ways both small and large. However, there are several people whom I would like to single out for special thanks for their support and assistance which contributed a lot to the completion of this dissertation: Swagata Das, Anamika Dubey, Jules Campbell, Mohit Singh, Alicia Allen, Duehee Lee, Min Lwin, David Jonsson, Jonas Traphoner,

Yichuan Niu, Kyung Woo Min, Tuan Ngo, Suma Jothibasu, Quan Nguyen, Harsha Vardhana Padullaparti, Wan Ki Cho, Hunter Estes, Vaidyanathan Krishnamurthy, and Miguel Hernandez.

I am very thankful to my Thai friends in Austin for their encouragement and advice, especially for helping me settle down in Austin. It would be difficult to acknowledge everyone who has in some way or another contributed to this dissertation. However, special gratitude goes out to Piyanuch Wonganan, Soraya Hengsawas, Touchanun Komonpaisarn, Jiraporn Chontichachalalauk, Arpamart Chanmeka, Nantinee Nualnim, Prasart Jongjaroenkamol, and Seepong Aiumjaroen.

I owe a great deal to my parents' friends, Nantana Rulon, Curt Rulon, Mukda Kowhakul, Ladda Campbell, and Tida Overway, for their continued support and hospitality since the first day I arrived in Austin. Without them, I would have had more difficulties, and my life in Austin would have been tough.

Last but not least, it would have been impossible for me to pursue a PhD without the support from my beloved family. I owe a debt of gratitude to my parents and grandparents for their unconditional love and endless support, without which, I would not have finished this dissertation.

Distribution Circuit Multi-Time-Scale Simulation Tool for Wind Turbine and Photovoltaic Integration Analysis

Pisitpol Chirapongsananurak, Ph.D.
The University of Texas at Austin, 2016

Supervisor: Surya Santoso

Power system phenomena can be characterized into three types according to their time scales. Firstly, electromagnetic transient phenomena, such as the effects of capacitor switching and lightning strikes, have a time scale range of microseconds to milliseconds. Secondly, electromechanical transient phenomena, such as short-circuit faults on distribution circuits and inertial and frequency response of the power system, have a time scale in the order of hundreds of milliseconds to tens of seconds. Lastly, quasi-steady-state phenomena, such as voltage regulation, voltage unbalance, and wind speed and solar irradiance variation, have a time scale of several minutes and longer. Currently, because the time scales of these phenomena vary greatly from fractions of cycles to a few hours, only power system simulation tools for specific time scales are available.

The objective of this research is to develop an integrated distribution circuit multi-time-scale simulation tool designed specifically for applications in wind turbine and photovoltaic (PV) integration analysis. This research contributes a multi-time-scale simulation tool for analysis and control of voltage regulation due to the variability of wind speed, solar irradiance, and load consumption, determining the maximum penetration of wind turbines and PVs, and sizing of energy storage for peak load shaving and power variability control.

The proposed multi-time-scale simulation tool developed in MATLAB^{TM} includes several distribution circuit components such as voltage sources, distribution lines, transformers, loads, capacitor banks, wind turbines, and PVs. Each equipment model in the proposed simulation tool consists of three models in different time scales, i.e., steady-state, electromechanical transient, and electromagnetic transient models. Therefore, the proposed tool is able to perform a long-term simulation involving power system phenomena spreading across time scales. Because distribution circuits are usually unbalanced, the proposed tool employs distribution circuit models with all three phases represented. The test circuit used to demonstrate the multi-time-scale simulation approach is the IEEE four-node test feeder with wind turbines and PVs connected at the feeder end. The results show that the proposed multi-time-scale simulation tool is able to simulate and analyze long-term power system phenomena spreading across time scales.

Table of Contents

Acknowledgments v

Abstract vii

List of Tables xii

List of Figures xiii

Chapter 1. Introduction 1

1.1 Background and Motivation 1

1.1.1 Power System Phenomena 2

1.1.2 Power System Simulation Tools 4

1.2 Contributions 7

1.3 Dissertation Outline 8

Chapter 2. Modeling of Typical Distribution Circuit Equipment 10

2.1 Steady-State Model 11

2.1.1 Fixed Impedance or Admittance Model 12

2.1.2 Distribution Line Model 12

2.1.3 Transformer Model 18

2.1.4 Distribution Network Solution 34

2.2 Electromechanical Transient Model 35

2.3 Electromagnetic Transient Model 35

2.3.1 Resistor Model 36

2.3.2 Inductor Model 36

2.3.3 Capacitor Model 37

2.3.4 Distribution Line Model 38

2.3.5 Transformer Model 46

2.3.6 Distribution Network Solution 50

Chapter 3. Modeling of Renewable Energy Sources in Distribution Circuits **52**
3.1 Models of Wind Turbines . . . 52
3.1.1 Aerodynamic System . . . 55
3.1.2 Mechanical System . . . 57
3.1.2.1 Electromagnetic Transient Model . . . 57
3.1.2.2 Electromechanical Transient Model . . . 58
3.1.2.3 Steady-State Model . . . 59
3.1.3 Generator . . . 59
3.1.3.1 Induction Generator . . . 59
3.1.3.2 Permanent Magnet Synchronous Generator . . . 67
3.1.4 Converter . . . 70
3.1.4.1 Electromagnetic Transient Model . . . 71
3.1.4.2 Electromechanical Transient Model . . . 72
3.1.4.3 Steady-State Model . . . 72
3.2 Models of PVs . . . 72
3.2.1 PV Array . . . 73
3.2.2 Inverter . . . 76

Chapter 4. Multi-Time-Scale Approach for Distribution Circuit Simulation **77**
4.1 Single-Time-Scale Simulation Models . . . 77
4.1.1 Steady-State Model . . . 78
4.1.1.1 FSWT Model . . . 79
4.1.1.2 WSWT Model . . . 80
4.1.1.3 DFIG and Full Converter Wind Turbine Model . . . 84
4.1.1.4 PV Model . . . 85
4.1.2 Electromechanical Transient Model . . . 86
4.1.2.1 FSWT Model . . . 86
4.1.2.2 WSWT Model . . . 87
4.1.2.3 DFIG and Full Converter Wind Turbine Model . . . 88
4.1.2.4 PV Model . . . 90
4.1.3 Electromagnetic Transient Model . . . 91
4.1.3.1 FSWT Model . . . 92
4.1.3.2 WSWT Model . . . 95
4.1.3.3 DFIG and Full Converter Wind Turbine Model . . . 95
4.1.3.4 PV Model . . . 97
4.2 Model Selection and Switching between Models . . . 97

Chapter 5. Simulation of Distribution Circuits **101**
5.1 Test Circuits 101
5.1.1 Four-Node Test Circuit for Wind Turbine Simulation 101
5.1.2 Three-Node Test Circuit for PV Simulation 104
5.2 Verification of Test Circuit Models 105
5.2.1 Verification of Test Circuit Model for Wind Turbine Simulation 106
5.2.2 Verification of Test Circuit Model for PV Simulation 108
5.3 Verification of Approach Used to Switch between Models 109
5.3.1 Switching between Models for an FSWT 111
5.3.2 Switching between Models for a WSWT 114
5.3.3 Switching between Models for DFIG and Full Converter Wind Turbines 116
5.3.4 Switching between Models for a PV 119
5.4 Simulation Results and Discussion 121
5.4.1 Simulation of an FSWT 122
5.4.1.1 Quasi-Steady-State Simulation of an FSWT 122
5.4.1.2 Multi-Time-Scale Simulation of an FSWT 124
5.4.2 Simulation of a WSWT 128
5.4.2.1 Quasi-Steady-State Simulation of a WSWT 129
5.4.2.2 Multi-Time-Scale Simulation of a WSWT 131
5.4.3 Simulation of DFIG and Full Converter Wind Turbines 133
5.4.3.1 Quasi-Steady-State Simulation of DFIG and Full Converter Wind Turbines 134
5.4.3.2 Multi-Time-Scale Simulation of DFIG and Full Converter Wind Turbines 135
5.4.4 Simulation of a PV 139
5.4.4.1 Quasi-Steady-State Simulation of a PV 140
5.4.4.2 Multi-Time-Scale Simulation of a PV 141

Chapter 6. Conclusion **146**

Bibliography **151**

List of Tables

4.1 Selected models for sample disturbances 98

5.1 Parameters of the mechanical system 103
5.2 Parameters of the SCIG 103
5.3 Parameters of the WRIG 104
5.4 Transformer data 105
5.5 Load data 105
5.6 Load data for the test circuit verification 106
5.7 Comparison of node voltage results for the four-node test circuit when the capacitor is offline 106
5.8 Comparison of node voltage results for the four-node test circuit when the capacitor is online 107
5.9 Comparison of node voltage results for the three-node test circuit when the capacitor is offline 109
5.10 Comparison of node voltage results for the three-node test circuit when the capacitor is online 109
5.11 Quasi-steady-state results of the FSWT simulation 122
5.12 Node voltage results of the FSWT simulation 123
5.13 Quasi-steady-state results of the WSWT simulation 129
5.14 Node voltage results of the WSWT simulation 130
5.15 Quasi-steady-state results of the DFIG and full converter wind turbine simulation 135
5.16 Node voltage results of the DFIG and full converter wind turbine simulation 136
5.17 Quasi-steady-state results of the PV simulation 140
5.18 Node voltage results of the PV simulation 141

6.1 Summary of distribution network, wind turbine, and PV models . . . 147

List of Figures

1.1 Time scales of power system phenomena 3

2.1 Distribution circuit equipment 11
2.2 Fixed impedance or admittance 12
2.3 Equivalent π model for a single-phase line 13
2.4 Equivalent-π model for a three-phase four-wire line 14
2.5 Steady-state model of a single-phase transformer 19
2.6 Configuration of a wye-wye transformer 20
2.7 Configuration of a wye-delta-center-tapped transformer 26
2.8 Injected currents and node voltages 34
2.9 Equivalent impedance network of a resistor 36
2.10 Equivalent impedance network of an inductor 37
2.11 Equivalent impedance network of a capacitor 38
2.12 Equivalent impedance network of a single-phase lossless line 39
2.13 Impedance network of a single-phase lossy line 40
2.14 Equivalent impedance network of a single-phase lossy line 41
2.15 Electromagnetic transient model of a single-phase transformer 46
2.16 Equivalent impedance network of a resistance-inductance series branch 49

3.1 Block diagram of an FSWT 53
3.2 Block diagram of a WSWT 54
3.3 Block diagram of a DFIG wind turbine 54
3.4 Block diagram of a full converter wind turbine 55
3.5 Rotor performance characteristic curve 57
3.6 Wind turbine drivetrain 58
3.7 Two-mass model 58
3.8 Electromagnetic transient model of an induction generator 60
3.9 Electromechanical transient model of the stator of an induction generator 65
3.10 Steady-state model of an induction generator 66
3.11 Electromagnetic transient model of a PMSG 68
3.12 Steady-state model of a PMSG 70

3.13 Maximum power point tracking curve 71
3.14 Block diagram of a PV 73
3.15 Equivalent circuit of a PV cell 74
3.16 Characteristic of a PV cell 75
3.17 Power output of a PV cell 75
3.18 Maximum power output of a PV cell 76

4.1 Interface of distribution network, wind turbine, and PV models . . . 78
4.2 Interface of distribution network, wind turbine, and PV models for a steady-state simulation 79
4.3 Block diagram for the steady-state model of an FSWT 80
4.4 Block diagram for the steady-state model of a WSWT 81
4.5 Positive-sequence steady-state model of a WRIG 82
4.6 Positive-sequence Thevenin equivalent circuit of a WRIG stator . . . 82
4.7 Simplified positive-sequence steady-state model of a WRIG 83
4.8 Block diagram for the steady-state model of DFIG and full converter wind turbines 85
4.9 Block diagram for the steady-state model of a PV 86
4.10 Block diagram for the electromechanical model of an FSWT 87
4.11 Block diagram for the electromechanical model of a WSWT 88
4.12 Block diagram for the electromechanical model of DFIG and full converter wind turbines 89
4.13 Block diagram for the electromechanical model of a PV 91
4.14 Interface of distribution network, wind turbine, and PV models for an electromagnetic transient simulation 92
4.15 Time line for a multi-time-scale simulation 99
4.16 Multi-time-scale simulation diagram 99

5.1 One-line diagram of the four-node test circuit for wind turbine simulations 102
5.2 One-line diagram of the three-node test circuit for PV simulations . . 104
5.3 Load voltage of the four-node test circuit in MATLAB™ 107
5.4 Load voltage of the four-node test circuit in PSCAD/EMTDC™ . . 108
5.5 Load voltage of the three-node test circuit in MATLAB™ 110
5.6 Load voltage of the three-node test circuit in PSCAD/EMTDC™ . . 110
5.7 Voltages at the FSWT when switching between the steady-state and electromagnetic transient models 112

5.8 Output currents of the FSWT when switching between the steady-state and electromagnetic transient models 112
5.9 Voltages at the FSWT when switching between the steady-state and electromechanical transient models 113
5.10 Output currents of the FSWT when switching between the steady-state and electromechanical transient models 113
5.11 Voltages at the WSWT when switching between the steady-state and electromagnetic transient models 114
5.12 Output currents of the WSWT when switching between the steady-state and electromagnetic transient models 115
5.13 Voltages at the WSWT when switching between the steady-state and electromechanical transient models 115
5.14 Output currents of the WSWT when switching between the steady-state and electromechanical transient models 116
5.15 Voltages at the wind turbine when switching between the steady-state and electromagnetic transient models 117
5.16 Output currents of the wind turbine when switching between the steady-state and electromagnetic transient models 117
5.17 Voltages at the wind turbine when switching between the steady-state and electromechanical transient models 118
5.18 Output currents of the wind turbine when switching between the steady-state and electromechanical transient models 118
5.19 Voltages at the PV bus when switching between the steady-state and electromagnetic transient models 119
5.20 Injected currents at the PV bus when switching between the steady-state and electromagnetic transient models 120
5.21 Voltages at the PV bus when switching between the steady-state and electromechanical transient models 120
5.22 Injected currents at the PV bus when switching between the steady-state and electromechanical transient models 121
5.23 Wind speed for the multi-time-scale simulation 125
5.24 Steady-state voltages at the FSWT 126
5.25 Transient voltages at the FSWT when the capacitor bank is turned on at 8:00 am 126
5.26 Transient voltages at the FSWT when the fault occurs at 2:00 pm . . 127
5.27 Transient voltages at the FSWT when the capacitor bank is turned off at 10:00 pm 128
5.28 Steady-state voltages at the WSWT 132
5.29 Transient voltages at the WSWT when the capacitor bank is turned on at 8:00 am 132
5.30 Transient voltages at the WSWT when the fault occurs at 2:00 pm . 133

5.31 Transient voltages at the WSWT when the capacitor bank is turned off at 10:00 pm 134
5.32 Steady-state voltages at the wind turbine 137
5.33 Transient voltages at the wind turbine when the capacitor bank is turned on at 8:00 am 138
5.34 Transient voltages at the wind turbine when the fault occurs at 2:00 pm 138
5.35 Transient voltages at the wind turbine when the capacitor bank is turned off at 10:00 pm 139
5.36 Solar irradiance for the multi-time-scale simulation 142
5.37 Steady-state voltages at the PV 143
5.38 Transient voltages at the PV when the capacitor bank is turned off at 8:00 am 143
5.39 Transient voltages at the PV when the fault occurs at 12:00 pm . . . 144
5.40 Transient voltages at the PV when the capacitor bank is turned on at 4:00 pm 144

Chapter 1

Introduction

1.1 Background and Motivation

Increasing penetration of renewable energy sources such as wind and solar raises concerns regarding their impacts on a power system. Although wind and solar power generation can reduce peak load demand and losses in a distribution circuit [1], these renewable energy sources may cause problems in a circuit such as voltage regulation [1–7], flicker [6, 8, 9], reverse power flow [1, 10], short-circuit current contribution [5, 6, 11–16], protection coordination [5], capacitor switching transients, and harmonics distortion [5, 6, 17–23].

Power system simulation programs have been employed to study and analyze the potential impacts of wind turbines and photovoltaics (PVs) to ensure that these renewable energy sources comply with interconnection standards such as ANSI C84.1-2011 [24], IEEE Std. 929-2000 [25], IEEE Std. 1021-1998 [26], and IEEE Std. 1547-2003 [27]. Simulation programs can help evaluate power quality phenomena such as voltage regulation, fault study, switching transients, and harmonics analysis. The simulation tool can also be used to perform the feasibility studies of operating wind turbines and PVs in a distribution system [28, 29], analyze the stability of a distribution system with wind and solar power [30–32], determine the maximum penetration or hosting capacity of wind turbines and PVs [33–36], evaluate the performance of wind turbine and PV control methods [37–40], and investigate the effects of energy storage systems [41–43] and reactive power sources such as capacitor banks, static var

compensators (SVCs), static synchronous compensators (STATCOMs) [41,44,45], and dynamic voltage restorers (DVRs) [46] to a distribution system having wind and PV generators.

Since the time scales of power system phenomena range from fractions of cycles to a few hours, only simulation tools for specific time scales are available. Therefore, the existing simulation tools are not capable of evaluating power system phenomena spreading across time scales. The motivation of this research is to improve power system simulation tools to allow power system analysis involving phenomena spreading across time scales.

The following section describes the background on power system phenomena and the state-of-the-art in power system simulation.

1.1.1 Power System Phenomena

Phenomena in power systems can be classified according to their time scales into three types: electromagnetic transient, electromechanical transient, and quasi-steady-state phenomena. Typical time scales of power system phenomena are shown in Fig. 1.1 [47].

Electromagnetic transient phenomena, such as effects of capacitor switching and lightning strikes on voltage and current, usually have a time scale in the range of microseconds to milliseconds. These phenomena involve energy exchange between electric and magnetic fields (inductors and capacitors) in the power system. Therefore, electric equipment, such as lines, transformers, capacitor banks, and generator windings, have to be modeled in detail, i.e., the effect of inductors and capacitors in transient conditions must be included. However, the dynamics of the mechanical systems of electromechanical machines, e.g., inertia of generators and motors, have

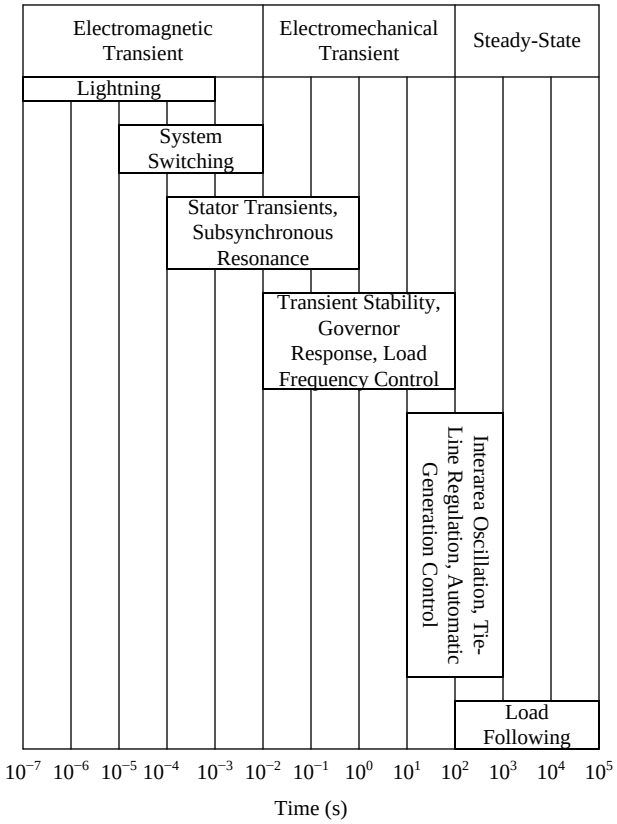

Figure 1.1: Time scales of power system phenomena

much longer time scales and may be neglected.

Electromechanical transient phenomena, such as effects of short-circuit faults, transient stability, inertial response, and frequency response, have a time scale from hundreds of milliseconds up to tens of seconds. Electromechanical transient phenomena usually involve energy exchange between electrical and mechanical systems (inductors, capacitors, and inertia) caused by a mismatch between power generation and consumption. Thus, the electromechanical components, e.g., generator and motor inertia, in the power system have to be modeled in great detail, i.e., the dynamics of rotating mass in electrical machines must be included. The models may neglect the

dynamics associating to electromagnetic transients in lines, transformers, capacitor banks, and stators of electrical machines.

Quasi-steady-state phenomena, such as voltage regulation, flicker, voltage unbalance, and wind speed, solar irradiance, and load demand variation, have a time scale of several minutes or longer. These phenomena are simulated by steady-state models disregarding all dynamics, both electromagnetic and electromechanical, of the power systems.

1.1.2 Power System Simulation Tools

Power system simulation tools can be classified into three types according to the time scales of power system phenomena, i.e., steady-state, electromechanical transient, and electromagnetic transient simulation tools.

Electromagnetic transient simulation tools are designed to simulate the dynamics of electric and magnetic fields. Since the time scales of electromagnetic transient phenomena are relatively short, i.e., from microseconds to milliseconds, complete models of electric equipment, such as lines, transformers, and capacitor banks, are employed. However, the dynamics of the mechanical systems, which have much longer time scales, may be neglected. The electromagnetic transient simulation tools are developed based on the electromagnetic transient program (EMTP) [48, 49]. The simulations are performed in a time domain, and the results are instantaneous values. These tools can be used to study the effects of capacitor switching and lightning strikes.

Electromechanical transient simulation tools are designed to simulate the dynamics of electrical and mechanical components of power systems, whose time scale is from a few seconds up to a few minutes. Any state variables that do not affect the behavior of the circuits in electromechanical transient conditions, such as tran-

sients in lines, transformers, and stator windings of electrical machines, are neglected. The electromechanical transient simulation tools are frequency-domain tools, which output results in the form of fundamental frequency magnitudes and phase angles. These tools can be used to study the stability of power systems. Hence, the tools are referred to as transient stability programs.

Steady-state simulation tools are designed to simulate quasi-steady-state phenomena in power systems. The time scale of these phenomena is several minutes or longer, so all derivative terms in the equations of the models can be neglected. Like the electromechanical transient tools, the steady-state tools are frequency-domain tools. These tools can be used to study voltage regulation, flicker, voltage unbalance, and wind and solar power variation. The most well-known approach for quasi-steady-state simulation is power-flow or load-flow programs. Although electromagnetic and electromechanical transient simulation tools are also able to simulate quasi-steady-state phenomena, the simulations take a long time to reach steady-state conditions.

Currently, since the time scales of each type of power system phenomena vary greatly from fractions of cycles up to a few hours, only simulation tools specific to each type of phenomena exist. These single-time-scale simulation tools have drawbacks because they can only simulate power system phenomena corresponding to their time scales.

PSCAD/EMTDC™ [50, 51] is a simulation tool designed specifically for electromagnetic transient simulations. PSCAD (Power Systems Computer Aided Design) is a graphical user interface to EMTDC (Electromagnetic Transients including DC) solver. EMTDC is used to solve differential equations in a time domain with a fixed time step. The solution approach used in EMTDC are based on EMTP approach. Although the simulation results are instantaneous values, the program can convert the results to a phasor form (magnitudes and phase angles). PSCAD/EMTDC™ can

also perform electromechanical transient and quasi-steady-state simulations. However, the time step is small because the electrical equipment such as inductors and capacitors are modeled in details. As a result, the simulation time is long.

OpenDSS™ [52] is a simulation tool designed specifically for quasi-steady-state simulations. OpenDSS™ classifies power system elements into two groups, i.e., power delivery and power conversion elements. Power delivery elements deliver electrical power from one group of terminals to another group of terminals of the elements, while power conversion elements convert electrical power to another form of power or vice versa. OpenDSS™ represents power delivery elements by impedances (frequency domain) in a nodal admittance matrix and represents power conversion elements by current source models. Iteration methods are used to solve the equations. Although OpenDSS™ is not designed specifically for electromechanical transient simulations, it can perform basic electromechanical transient analysis. However, OpenDSS™ is not able to perform electromagnetic transient simulations.

DIgSILENT PowerFactory™ [53] is a simulation tool for electromagnetic transient, electromechanical transient, and quasi-steady-state simulations. This program consists of two major simulation tools. The first tool developed by using a time-domain approach is used for electromagnetic transient simulations. The second tool developed by using a frequency-domain approach is used for electromechanical transient and quasi-steady-state simulations. Although DIgSILENT PowerFactory™ is able to simulate power system phenomena in all three time scales, this program can only simulate power system phenomena in their individual time scale, i.e., it cannot simulate power system phenomena spreading across time scales.

1.2 Contributions

This research contributes a multi-time-scale simulation tool for analyzing distribution circuits including wind generators and PV panels. The proposed multi-time-scale simulation tool developed in MATLAB^{TM} consists of models for typical distribution circuit equipment such as voltage sources, distribution lines, transformers, loads, and capacitor banks. Since distribution circuits are usually unbalanced due to single-phase loads and single-phase circuits in the systems, the proposed tool employs full circuit models with all three phases represented. In order to evaluate the impacts of renewable energy sources, the proposed simulation tool also has models of wind turbines and PVs.

Each equipment model in the proposed multi-time-scale simulation tool consists of three single-time-scale models in different time scales, i.e., steady-state, electromechanical transient, and electromagnetic transient models. Therefore, the proposed tool is able to perform a long-term simulation and evaluate power system phenomena spreading across time scales. The single-time-scale models are pre-selected according to the types of each disturbance occur in the distribution circuit before the simulation starts. When quasi-steady-state phenomena occur, the simulation is performed by using the steady-state model. When electromechanical transient phenomena occur, the proposed simulation tool employs the electromagnetic transient model to perform a simulation in an electromechanical transient period. As soon as the transient vanishes and the power system reaches a steady-state condition, the simulation tool switches back to the steady-state model. When electromagnetic transient phenomena occur, the proposed tool switches to the electromagnetic transient model to simulate the distribution circuit in an electromagnetic transient condition. After the circuit reaches a steady-state condition, the steady-state model is used again.

Note that in order to smoothly switch from one model to another model, the voltages and currents of all circuit elements must be the same before and after switching. Thus, the proposed multi-time-scale simulation tool only switches when the circuit is in a steady-state condition with no existing electromechanical or electromagnetic transient dynamics.

The specific objectives of this research are to develop the interface between the typical distribution circuit equipment and the renewable energy sources, i.e., wind turbines and PVs, and to integrate the steady-state, electromechanical transient, and electromagnetic transient models into the proposed multi-time-scale simulation tool. The first objective involves developing the approaches to connect the wind turbine and PV models to the typical distribution circuit models represented by an admittance matrix. Since the proposed multi-time-scale simulation tool consists of three models for three different time scales, an interface approach is developed for each single-time-scale model. The second objective involves developing the approaches to select which single-time-scale model to use for each disturbance and the approaches to switch between two single-time-scale models.

The proposed multi-time-scale simulation tool can be used for applications in wind turbine and PV integration including analysis and control of voltage regulation due to wind, solar, and load variability, determining the maximum penetration of wind turbines and PVs, and sizing of energy storage for peak load shaving and power variability control.

1.3 Dissertation Outline

This dissertation is organized as follows: Chapters 2 and 3 describe the electromagnetic transient, electromechanical transient, and steady-state models of distribu-

tion circuit equipment including voltage sources, lines, transformers, loads, capacitor banks, wind turbines, and PVs. Chapter 4 explains the proposed multi-time-scale simulation approach including the development of the single-time-scale simulation models and the integration of the single-time-scale models into the multi-time-scale simulation. Chapter 5 details the case study for the multi-time-scale simulation including the test circuit, simulation results, and discussion, followed by the conclusion in Chapter 6.

Chapter 2

Modeling of Typical Distribution Circuit Equipment

This chapter describes the modeling of typical distribution circuit equipment for the proposed multi-time-scale simulation tool. A typical distribution circuit consists of voltage sources, lines, transformers, loads, capacitor banks, and regulators distributed throughout the circuit. To accommodate renewable energy sources, future circuits may consist of synchronous machines, induction machines, energy storage systems, STATCOMs, wind turbines, and PV panels in addition to what a typical circuit has. Since distribution circuits are usually unbalanced due to the presence of single-phase loads and single-phase circuits in the systems, positive-sequence models do not capture all circuit behaviors. For this reason, distribution circuit models have to be full models with all three phases represented.

The equipment employed in distribution circuits can be classified into two types as shown in Fig. 2.1. The first type is the equipment that have fixed impedances or admittances, such as distribution feeders, transformers, capacitor banks, and constant impedance loads. These equipment are connected to each other and form a three-phase distribution network represented by a nodal admittance matrix. The second type is the equipment that contain voltage or current sources or have variable impedances or admittances, such as constant power loads, synchronous machines, induction machines, energy storage systems, STATCOMs, wind turbines, and PVs. These equipment are represented by voltage or current sources connected to a distri-

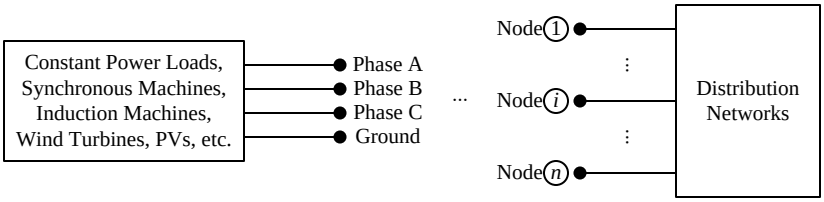

Figure 2.1: Distribution circuit equipment

bution network.

The following sections describe the development of models for three-phase distribution networks. Models of typical equipment in distribution networks including distribution feeders, transformers, capacitor banks, and loads are discussed. Each equipment model consists of three models for three different time scales, i.e., steady-state, electromechanical transient, and electromagnetic transient models. The approach presented in these sections can also be used to represent other equipment that can be modeled by a Thevenin or Norton equivalent circuit with a fixed impedance or admittance.

2.1 Steady-State Model

In a steady-state condition, all transient dynamics are neglected. Thus, the distribution circuit equipment, e.g., distribution feeders, transformers, capacitor banks, and constant impedance loads, can be represented by a fixed impedance in a frequency domain (phasor form). The equipment are connected to each other and form a three-phase distribution network represented by a nodal admittance matrix [54, 55]. The approach used to build the nodal admittance matrix for fixed impedances or admittances [54, 55], distribution lines [54–57], and transformers [58, 59] are described in the following sections.

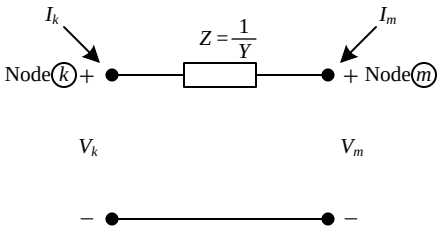

Figure 2.2: Fixed impedance or admittance

2.1.1 Fixed Impedance or Admittance Model

A capacitor bank and a constant impedance load can be represented by a fixed impedance (Z) or admittance (Y) as shown in Fig. 2.2. The currents injected to node k and m are calculated by

$$I_k = \frac{1}{Z}\left(V_k - V_m\right) = Y\left(V_k - V_m\right) \tag{2.1}$$

$$I_m = \frac{1}{Z}\left(V_m - V_k\right) = Y\left(V_m - V_k\right) \tag{2.2}$$

The nodal equation for a fixed impedance or admittance is

$$\begin{bmatrix} I_k \\ I_m \end{bmatrix} = \begin{bmatrix} \frac{1}{Z} & -\frac{1}{Z} \\ -\frac{1}{Z} & \frac{1}{Z} \end{bmatrix} \begin{bmatrix} V_k \\ V_m \end{bmatrix} = \begin{bmatrix} Y & -Y \\ -Y & Y \end{bmatrix} \begin{bmatrix} V_k \\ V_m \end{bmatrix} \tag{2.3}$$

For shunt elements, node m is connected to ground. Hence, the voltage at node m (V_m) is zero, and the current injected to node m is the ground current which is not interested. The nodal equation becomes

$$I_k = \frac{1}{Z}V_k = YV_k \tag{2.4}$$

2.1.2 Distribution Line Model

A single-phase distribution line can be represented by an equivalent-π model [54] as shown in Fig. 2.3. Note that the line parameter calculations are described in

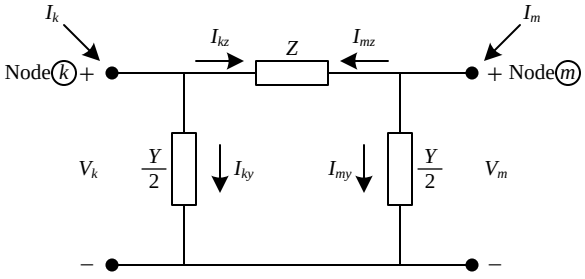

Figure 2.3: Equivalent π model for a single-phase line

[54,57]. The currents flowing through the series impedance (Z) and shunt admittances (Y) of the line can be calculated by

$$I_{kz} = \frac{1}{Z}\left(V_k - V_m\right) \tag{2.5}$$

$$I_{mz} = \frac{1}{Z}\left(V_m - V_k\right) \tag{2.6}$$

$$I_{ky} = \frac{Y}{2}V_k \tag{2.7}$$

$$I_{my} = \frac{Y}{2}V_m \tag{2.8}$$

The currents injected to node k and m are obtained by

$$I_k = I_{kz} + I_{ky} = \frac{1}{Z}\left(V_k - V_m\right) + \frac{Y}{2}V_k = \left(\frac{1}{Z} + \frac{Y}{2}\right)V_k - \frac{1}{Z}V_m \tag{2.9}$$

$$I_m = I_{mz} + I_{my} = \frac{1}{Z}\left(V_m - V_k\right) + \frac{Y}{2}V_m = \left(\frac{1}{Z} + \frac{Y}{2}\right)V_m - \frac{1}{Z}V_k \tag{2.10}$$

The nodal equation for a single-phase line is

$$\begin{bmatrix} I_k \\ I_m \end{bmatrix} = \begin{bmatrix} \frac{1}{Z} + \frac{Y}{2} & -\frac{1}{Z} \\ -\frac{1}{Z} & \frac{1}{Z} + \frac{Y}{2} \end{bmatrix} \begin{bmatrix} V_k \\ V_m \end{bmatrix} \tag{2.11}$$

For a three-phase four-wire line as shown in Fig. 2.4, the series impedance (Z_{branch}) and shunt admittances (Y_{branch}) in the equivalent-π model become 4-by-4 matrices as follows:

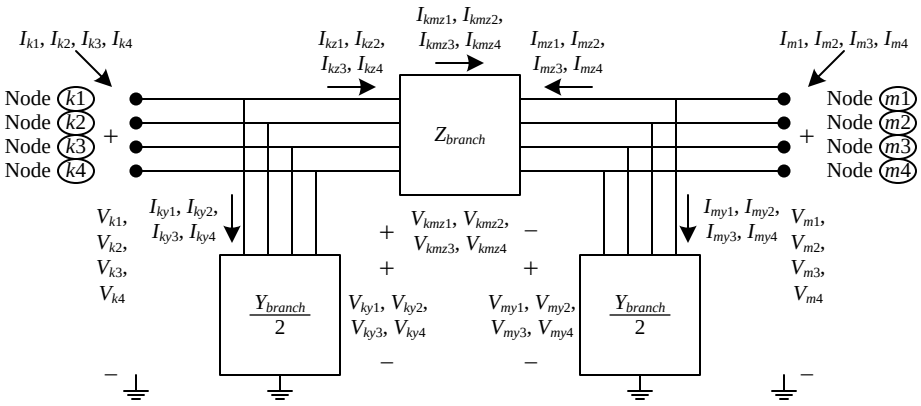

Figure 2.4: Equivalent-π model for a three-phase four-wire line

$$Z_{branch} = \begin{bmatrix} Z_{11} & Z_{12} & Z_{13} & Z_{14} \\ Z_{21} & Z_{22} & Z_{23} & Z_{24} \\ Z_{31} & Z_{32} & Z_{33} & Z_{34} \\ Z_{41} & Z_{42} & Z_{43} & Z_{44} \end{bmatrix} \tag{2.12}$$

$$Y_{branch} = \begin{bmatrix} Y_{11} & Y_{12} & Y_{13} & Y_{14} \\ Y_{21} & Y_{22} & Y_{23} & Y_{24} \\ Y_{31} & Y_{32} & Y_{33} & Y_{34} \\ Y_{41} & Y_{42} & Y_{43} & Y_{44} \end{bmatrix} \tag{2.13}$$

The approaches used to obtain Z_{branch} and Y_{branch} from the line parameters are described in [56]. The branch equation for the series impedance is given by

$$\begin{bmatrix} I_{kmz1} \\ I_{kmz2} \\ I_{kmz3} \\ I_{kmz4} \end{bmatrix} = \begin{bmatrix} Z_{11} & Z_{12} & Z_{13} & Z_{14} \\ Z_{21} & Z_{22} & Z_{23} & Z_{24} \\ Z_{31} & Z_{32} & Z_{33} & Z_{34} \\ Z_{41} & Z_{42} & Z_{43} & Z_{44} \end{bmatrix}^{-1} \begin{bmatrix} V_{kmz1} \\ V_{kmz2} \\ V_{kmz3} \\ V_{kmz4} \end{bmatrix} \tag{2.14}$$

The branch equation for the series impedance in (2.14) can be rewritten as

$$I_{z,branch} = Z_{branch}^{-1} V_{z,branch} \tag{2.15}$$

where $I_{z,branch}$ and $V_{z,branch}$ are defined by

$$I_{z,branch} = \begin{bmatrix} I_{kmz1} \\ I_{kmz2} \\ I_{kmz3} \\ I_{kmz4} \end{bmatrix} \tag{2.16}$$

$$V_{z,branch} = \begin{bmatrix} V_{kmz1} \\ V_{kmz2} \\ V_{kmz3} \\ V_{kmz4} \end{bmatrix} \tag{2.17}$$

The currents injected to the series impedance are calculated from the branch currents as follows:

$$\begin{bmatrix} I_{kz1} \\ I_{kz2} \\ I_{kz3} \\ I_{kz4} \\ I_{mz1} \\ I_{mz2} \\ I_{mz3} \\ I_{mz4} \end{bmatrix} = \begin{bmatrix} I_{kmz1} \\ I_{kmz2} \\ I_{kmz3} \\ I_{kmz4} \\ -I_{kmz1} \\ -I_{kmz2} \\ -I_{kmz3} \\ -I_{kmz4} \end{bmatrix} = \begin{bmatrix} 1 & 0 & 0 & 0 \\ 0 & 1 & 0 & 0 \\ 0 & 0 & 1 & 0 \\ 0 & 0 & 0 & 1 \\ -1 & 0 & 0 & 0 \\ 0 & -1 & 0 & 0 \\ 0 & 0 & -1 & 0 \\ 0 & 0 & 0 & -1 \end{bmatrix} \begin{bmatrix} I_{kmz1} \\ I_{kmz2} \\ I_{kmz3} \\ I_{kmz4} \end{bmatrix} \tag{2.18}$$

The branch voltages of the series impedance are calculated from the nodal voltages as follows:

$$\begin{bmatrix} V_{kmz1} \\ V_{kmz2} \\ V_{kmz3} \\ V_{kmz4} \end{bmatrix} = \begin{bmatrix} V_{k1} - V_{m1} \\ V_{k2} - V_{m2} \\ V_{k3} - V_{m3} \\ V_{k4} - V_{m4} \end{bmatrix} = \begin{bmatrix} 1 & 0 & 0 & 0 & -1 & 0 & 0 & 0 \\ 0 & 1 & 0 & 0 & 0 & -1 & 0 & 0 \\ 0 & 0 & 1 & 0 & 0 & 0 & -1 & 0 \\ 0 & 0 & 0 & 1 & 0 & 0 & 0 & -1 \end{bmatrix} \begin{bmatrix} V_{k1} \\ V_{k2} \\ V_{k3} \\ V_{k4} \\ V_{m1} \\ V_{m2} \\ V_{m3} \\ V_{m4} \end{bmatrix} \tag{2.19}$$

The relationship between the nodal and branch currents and voltages of the series impedance in (2.18) and (2.19) can be rewritten as

$$I_{z,node} = A^{\mathrm{T}} I_{z,branch} \tag{2.20}$$

$$V_{z,branch} = AV_{z,node} \tag{2.21}$$

where A is the incidence matrix of the series impedance. $I_{z,node}$, $V_{z,node}$, and A are defined by

$$I_{z,node} = \begin{bmatrix} I_{kz1} \\ I_{kz2} \\ I_{kz3} \\ I_{kz4} \\ I_{mz1} \\ I_{mz2} \\ I_{mz3} \\ I_{mz4} \end{bmatrix} \tag{2.22}$$

$$V_{z,node} = \begin{bmatrix} V_{k1} \\ V_{k2} \\ V_{k3} \\ V_{k4} \\ V_{m1} \\ V_{m2} \\ V_{m3} \\ V_{m4} \end{bmatrix} \tag{2.23}$$

$$A = \begin{bmatrix} 1 & 0 & 0 & 0 & -1 & 0 & 0 & 0 \\ 0 & 1 & 0 & 0 & 0 & -1 & 0 & 0 \\ 0 & 0 & 1 & 0 & 0 & 0 & -1 & 0 \\ 0 & 0 & 0 & 1 & 0 & 0 & 0 & -1 \end{bmatrix} \tag{2.24}$$

The nodal admittance equation of the series impedance is obtained from (2.15), (2.20), and (2.21) as follows:

$$I_{z,node} = A^{\mathrm{T}} Z_{branch}^{-1} A V_{z,node} \tag{2.25}$$

The branch equations for the shunt admittances are given by

$$\begin{bmatrix} I_{ky1} \\ I_{ky2} \\ I_{ky3} \\ I_{ky4} \end{bmatrix} = \frac{1}{2} \begin{bmatrix} Y_{11} & Y_{12} & Y_{13} & Y_{14} \\ Y_{21} & Y_{22} & Y_{23} & Y_{24} \\ Y_{31} & Y_{32} & Y_{33} & Y_{34} \\ Y_{41} & Y_{42} & Y_{43} & Y_{44} \end{bmatrix} \begin{bmatrix} V_{ky1} \\ V_{ky2} \\ V_{ky3} \\ V_{ky4} \end{bmatrix} \tag{2.26}$$

$$\begin{bmatrix} I_{my1} \\ I_{my2} \\ I_{my3} \\ I_{my4} \end{bmatrix} = \frac{1}{2} \begin{bmatrix} Y_{11} & Y_{12} & Y_{13} & Y_{14} \\ Y_{21} & Y_{22} & Y_{23} & Y_{24} \\ Y_{31} & Y_{32} & Y_{33} & Y_{34} \\ Y_{41} & Y_{42} & Y_{43} & Y_{44} \end{bmatrix} \begin{bmatrix} V_{my1} \\ V_{my2} \\ V_{my3} \\ V_{my4} \end{bmatrix} \tag{2.27}$$

The branch equations of the shunt admittances in (2.26) and (2.27) can be rewritten as

$$I_{y,branch} = \begin{bmatrix} \frac{1}{2}Y_{branch} & 0 \\ 0 & \frac{1}{2}Y_{branch} \end{bmatrix} V_{y,branch} \tag{2.28}$$

where $I_{y,branch}$ and $V_{y,branch}$ are defined by

$$I_{y,branch} = \begin{bmatrix} I_{ky1} \\ I_{ky2} \\ I_{ky3} \\ I_{ky4} \\ I_{my1} \\ I_{my2} \\ I_{my3} \\ I_{my4} \end{bmatrix} \tag{2.29}$$

$$V_{y,branch} = \begin{bmatrix} V_{ky1} \\ V_{ky2} \\ V_{ky3} \\ V_{ky4} \\ V_{my1} \\ V_{my2} \\ V_{my3} \\ V_{my4} \end{bmatrix} \tag{2.30}$$

The injected currents of the shunt admittances are the same as the branch currents, and the nodal voltages of the shunt admittances are the same as the branch voltages. Therefore, the incidence matrices of the shunt admittances are 4-by-4 identity matrices. The nodal admittance equations of the shunt admittances at nodes k and m are

$$I_{y,node} = \begin{bmatrix} \frac{1}{2}Y_{branch} & 0 \\ 0 & \frac{1}{2}Y_{branch} \end{bmatrix} V_{y,node} \tag{2.31}$$

The nodal equation for a three-phase four-wire line is

$$\begin{aligned} I_{node} &= I_{z,node} + I_{y,node} \\ &= A^{\mathrm{T}} Z_{branch}^{-1} A V_{z,node} + \begin{bmatrix} \frac{1}{2}Y_{branch} & 0 \\ 0 & \frac{1}{2}Y_{branch} \end{bmatrix} V_{y,node} \\ &= \left(A^{\mathrm{T}} Z_{branch}^{-1} A + \begin{bmatrix} \frac{1}{2}Y_{branch} & 0 \\ 0 & \frac{1}{2}Y_{branch} \end{bmatrix} \right) V_{node} \end{aligned} \tag{2.32}$$

where I_{node} and V_{node} are defined by

$$I_{node} = \begin{bmatrix} I_{k1} \\ I_{k2} \\ I_{k3} \\ I_{k4} \\ I_{m1} \\ I_{m2} \\ I_{m3} \\ I_{m4} \end{bmatrix} \tag{2.33}$$

$$V_{node} = \begin{bmatrix} V_{k1} \\ V_{k2} \\ V_{k3} \\ V_{k4} \\ V_{m1} \\ V_{m2} \\ V_{m3} \\ V_{m4} \end{bmatrix} \tag{2.34}$$

2.1.3 Transformer Model

The equivalent circuit of a single-phase transformer in a steady-state condition is shown in Fig. 2.5. Since the core-loss resistance (R_c) is much larger than the winding resistances (R_p and R_s), and the magnetizing reactance (X_m) is much larger than the leakage reactances (X_{lp} and X_{ls}), the core-loss resistance and magnetizing

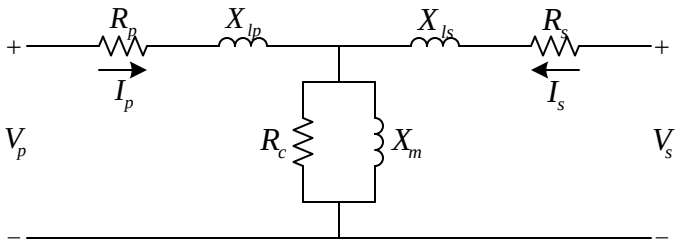

Figure 2.5: Steady-state model of a single-phase transformer

reactance can be neglected. Hence, the transformer impedance (Z_t) is obtained as follows:

$$Z_t = (R_p + R_s) + j\,(X_{lp} + X_{ls}) \tag{2.35}$$

A wye-wye transformer can be represented by three single-phase transformers connected in wye-wye configuration as shown in Fig. 2.6. The branch equation of the transformer impedances is given by

$$\begin{bmatrix} I_{kmb1} \\ I_{kmb2} \\ I_{kmb3} \end{bmatrix} = \begin{bmatrix} Z_{11} & Z_{12} & Z_{13} \\ Z_{21} & Z_{22} & Z_{23} \\ Z_{31} & Z_{32} & Z_{33} \end{bmatrix}^{-1} \begin{bmatrix} V_{kmb1} \\ V_{kmb2} \\ V_{kmb3} \end{bmatrix} \tag{2.36}$$

Note that the off-diagonal elements of the transformer impedance matrix (Z_{12}, Z_{13}, Z_{21}, Z_{23}, Z_{31}, and Z_{32}) are zero when there is no coupling among the single-phase transformers. The branch equation for the transformer impedances in (2.36) can be rewritten as

$$I_{kmb} = Z_b^{-1} V_{kmb} \tag{2.37}$$

where I_{kmb}, V_{kmb}, and Z_b are defined by

$$I_{kmb} = \begin{bmatrix} I_{kmb1} \\ I_{kmb2} \\ I_{kmb3} \end{bmatrix} \tag{2.38}$$

$$V_{kmb} = \begin{bmatrix} V_{kmb1} \\ V_{kmb2} \\ V_{kmb3} \end{bmatrix} \tag{2.39}$$

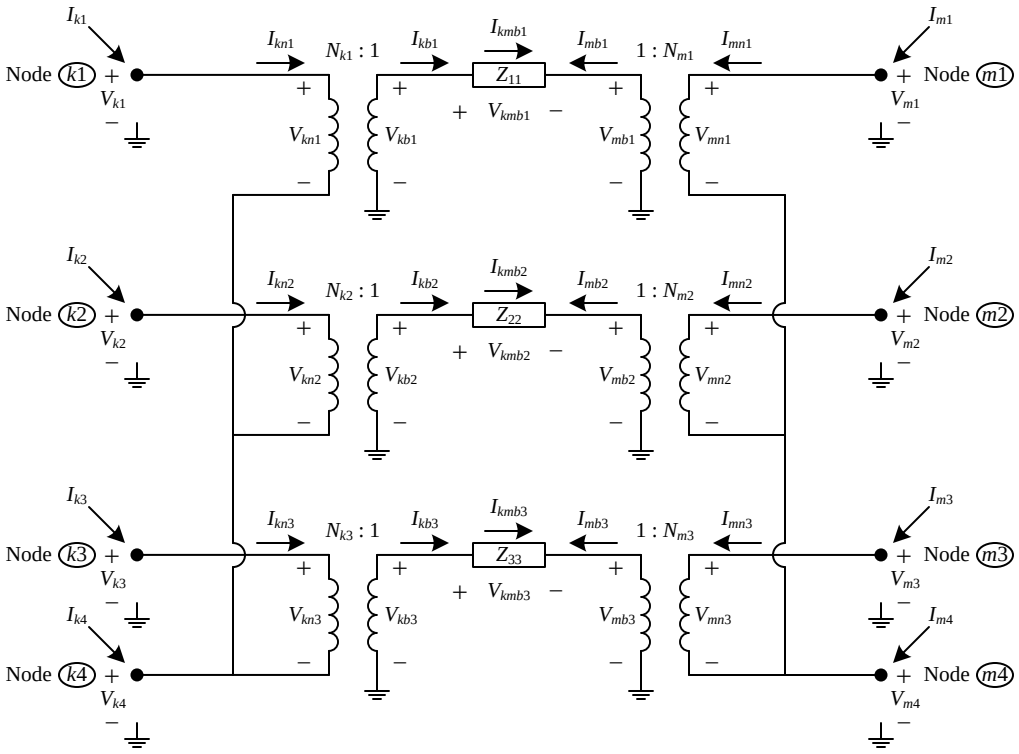

Figure 2.6: Configuration of a wye-wye transformer

$$Z_b = \begin{bmatrix} Z_{11} & Z_{12} & Z_{13} \\ Z_{21} & Z_{22} & Z_{23} \\ Z_{31} & Z_{32} & Z_{33} \end{bmatrix} \tag{2.40}$$

The currents injected to the transformer impedances at 1-V base are calculated from the branch currents as follows:

$$\begin{bmatrix} I_{kb1} \\ I_{kb2} \\ I_{kb3} \\ I_{mb1} \\ I_{mb2} \\ I_{mb3} \end{bmatrix} = \begin{bmatrix} I_{kmb1} \\ I_{kmb2} \\ I_{kmb3} \\ -I_{kmb1} \\ -I_{kmb2} \\ -I_{kmb3} \end{bmatrix} = \begin{bmatrix} 1 & 0 & 0 \\ 0 & 1 & 0 \\ 0 & 0 & 1 \\ -1 & 0 & 0 \\ 0 & -1 & 0 \\ 0 & 0 & -1 \end{bmatrix} \begin{bmatrix} I_{kmb1} \\ I_{kmb2} \\ I_{kmb3} \end{bmatrix} \tag{2.41}$$

The branch voltages of the transformer impedances are calculated from the nodal voltages at 1-V base as follows:

$$\begin{bmatrix} V_{kmb1} \\ V_{kmb2} \\ V_{kmb3} \end{bmatrix} = \begin{bmatrix} V_{kb1} - V_{mb1} \\ V_{kb2} - V_{mb2} \\ V_{kb3} - V_{mb3} \end{bmatrix} = \begin{bmatrix} 1 & 0 & 0 & -1 & 0 & 0 \\ 0 & 1 & 0 & 0 & -1 & 0 \\ 0 & 0 & 1 & 0 & 0 & -1 \end{bmatrix} \begin{bmatrix} V_{kb1} \\ V_{kb2} \\ V_{kb3} \\ V_{mb1} \\ V_{mb2} \\ V_{mb3} \end{bmatrix} \tag{2.42}$$

The relationship between the nodal and branch currents and voltages (at 1-V base) of the transformer impedances in (2.41) and (2.42) can be rewritten as

$$I_b = B^{\mathrm{T}} I_{kmb} \tag{2.43}$$

$$V_{kmb} = B V_b \tag{2.44}$$

where I_b, V_b, and B are defined by

$$I_b = \begin{bmatrix} I_{kb1} \\ I_{kb2} \\ I_{kb3} \\ I_{mb1} \\ I_{mb2} \\ I_{mb3} \end{bmatrix} \tag{2.45}$$

$$V_b = \begin{bmatrix} V_{kb1} \\ V_{kb2} \\ V_{kb3} \\ V_{mb1} \\ V_{mb2} \\ V_{mb3} \end{bmatrix} \tag{2.46}$$

$$B = \begin{bmatrix} 1 & 0 & 0 & -1 & 0 & 0 \\ 0 & 1 & 0 & 0 & -1 & 0 \\ 0 & 0 & 1 & 0 & 0 & -1 \end{bmatrix} \tag{2.47}$$

The nodal admittance equation of the transformer impedance at 1-V base is obtained from (2.37), (2.43), and (2.44) as follows:

$$I_b = B^{\mathrm{T}} Z_b^{-1} B V_b \tag{2.48}$$

The currents injected to the primary and secondary of the transformer are calculated from the currents injected to the transformer impedances at 1-V base as follows:

$$\begin{bmatrix} I_{kn1} \\ I_{kn2} \\ I_{kn3} \\ I_{mn1} \\ I_{mn2} \\ I_{mn3} \end{bmatrix} = \begin{bmatrix} \frac{I_{kb1}}{N_{k1}} \\ \frac{I_{kb2}}{N_{k2}} \\ \frac{I_{kb3}}{N_{k3}} \\ \frac{I_{mb1}}{N_{m1}} \\ \frac{I_{mb2}}{N_{m2}} \\ \frac{I_{mb3}}{N_{m3}} \end{bmatrix} = \begin{bmatrix} \frac{1}{N_{k1}} & 0 & 0 & 0 & 0 & 0 \\ 0 & \frac{1}{N_{k2}} & 0 & 0 & 0 & 0 \\ 0 & 0 & \frac{1}{N_{k3}} & 0 & 0 & 0 \\ 0 & 0 & 0 & \frac{1}{N_{m1}} & 0 & 0 \\ 0 & 0 & 0 & 0 & \frac{1}{N_{m2}} & 0 \\ 0 & 0 & 0 & 0 & 0 & \frac{1}{N_{m3}} \end{bmatrix} \begin{bmatrix} I_{kb1} \\ I_{kb2} \\ I_{kb3} \\ I_{mb1} \\ I_{mb2} \\ I_{mb3} \end{bmatrix} \tag{2.49}$$

The nodal voltages at 1-V base are calculated from the primary and secondary nodal voltages as follows:

$$\begin{bmatrix} V_{kb1} \\ V_{kb2} \\ V_{kb3} \\ V_{mb1} \\ V_{mb2} \\ V_{mb3} \end{bmatrix} = \begin{bmatrix} \frac{V_{kn1}}{N_{k1}} \\ \frac{V_{kn2}}{N_{k2}} \\ \frac{V_{kn3}}{N_{k3}} \\ \frac{V_{mn1}}{N_{m1}} \\ \frac{V_{mn2}}{N_{m2}} \\ \frac{V_{mn3}}{N_{m3}} \end{bmatrix} = \begin{bmatrix} \frac{1}{N_{k1}} & 0 & 0 & 0 & 0 & 0 \\ 0 & \frac{1}{N_{k2}} & 0 & 0 & 0 & 0 \\ 0 & 0 & \frac{1}{N_{k3}} & 0 & 0 & 0 \\ 0 & 0 & 0 & \frac{1}{N_{m1}} & 0 & 0 \\ 0 & 0 & 0 & 0 & \frac{1}{N_{m2}} & 0 \\ 0 & 0 & 0 & 0 & 0 & \frac{1}{N_{m3}} \end{bmatrix} \begin{bmatrix} V_{kn1} \\ V_{kn2} \\ V_{kn3} \\ V_{mn1} \\ V_{mn2} \\ V_{mn3} \end{bmatrix} \tag{2.50}$$

The relationship between the primary and secondary nodal currents and voltages and the nodal currents and voltages at 1-V base in (2.49) and (2.50) can be rewritten as

$$I_n = N^{\mathrm{T}} I_b \tag{2.51}$$

$$V_b = N V_n \tag{2.52}$$

where I_n, V_n, and N are defined by

$$I_n = \begin{bmatrix} I_{kn1} \\ I_{kn2} \\ I_{kn3} \\ I_{mn1} \\ I_{mn2} \\ I_{mn3} \end{bmatrix} \tag{2.53}$$

$$V_n = \begin{bmatrix} V_{kn1} \\ V_{kn2} \\ V_{kn3} \\ V_{mn1} \\ V_{mn2} \\ V_{mn3} \end{bmatrix} \tag{2.54}$$

$$N = \begin{bmatrix} \frac{1}{N_{k1}} & 0 & 0 & 0 & 0 & 0 \\ 0 & \frac{1}{N_{k2}} & 0 & 0 & 0 & 0 \\ 0 & 0 & \frac{1}{N_{k3}} & 0 & 0 & 0 \\ 0 & 0 & 0 & \frac{1}{N_{m1}} & 0 & 0 \\ 0 & 0 & 0 & 0 & \frac{1}{N_{m2}} & 0 \\ 0 & 0 & 0 & 0 & 0 & \frac{1}{N_{m3}} \end{bmatrix} \tag{2.55}$$

The nodal admittance equation of the transformer at the primary and secondary is obtained from (2.48), (2.51), and (2.52) as follows:

$$I_n = N^{\mathrm{T}} B^{\mathrm{T}} Z_b^{-1} B N V_n \tag{2.56}$$

The currents injected to nodes $k1$, $k2$, $k3$, $k4$, $m1$, $m2$, $m3$, and $m4$ are calculated from the currents injected to the primary and secondary of the transformer as follows:

$$\begin{bmatrix} I_{k1} \\ I_{k2} \\ I_{k3} \\ I_{k4} \\ I_{m1} \\ I_{m2} \\ I_{m3} \\ I_{m4} \end{bmatrix} = \begin{bmatrix} I_{kn1} \\ I_{kn2} \\ I_{kn3} \\ -I_{kn1} - I_{kn2} - I_{kn3} \\ I_{mn1} \\ I_{mn2} \\ I_{mn3} \\ -I_{mn1} - I_{mn2} - I_{mn3} \end{bmatrix} = \begin{bmatrix} 1 & 0 & 0 & 0 & 0 & 0 \\ 0 & 1 & 0 & 0 & 0 & 0 \\ 0 & 0 & 1 & 0 & 0 & 0 \\ -1 & -1 & -1 & 0 & 0 & 0 \\ 0 & 0 & 0 & 1 & 0 & 0 \\ 0 & 0 & 0 & 0 & 1 & 0 \\ 0 & 0 & 0 & 0 & 0 & 1 \\ 0 & 0 & 0 & -1 & -1 & -1 \end{bmatrix} \begin{bmatrix} I_{kn1} \\ I_{kn2} \\ I_{kn3} \\ I_{mn1} \\ I_{mn2} \\ I_{mn3} \end{bmatrix} \tag{2.57}$$

The primary and secondary nodal voltages are calculated from the voltages at nodes $k1$, $k2$, $k3$, $k4$, $m1$, $m2$, $m3$, and $m4$ as follows:

$$\begin{bmatrix} V_{kn1} \\ V_{kn2} \\ V_{kn3} \\ V_{mn1} \\ V_{mn2} \\ V_{mn3} \end{bmatrix} = \begin{bmatrix} V_{k1} - V_{k4} \\ V_{k2} - V_{k4} \\ V_{k3} - V_{k4} \\ V_{m1} - V_{m4} \\ V_{m2} - V_{m4} \\ V_{m3} - V_{m4} \end{bmatrix} = \begin{bmatrix} 1 & 0 & 0 & -1 & 0 & 0 & 0 & 0 \\ 0 & 1 & 0 & -1 & 0 & 0 & 0 & 0 \\ 0 & 0 & 1 & -1 & 0 & 0 & 0 & 0 \\ 0 & 0 & 0 & 0 & 1 & 0 & 0 & -1 \\ 0 & 0 & 0 & 0 & 0 & 1 & 0 & -1 \\ 0 & 0 & 0 & 0 & 0 & 0 & 1 & -1 \end{bmatrix} \begin{bmatrix} V_{k1} \\ V_{k2} \\ V_{k3} \\ V_{k4} \\ V_{m1} \\ V_{m2} \\ V_{m3} \\ V_{m4} \end{bmatrix} \tag{2.58}$$

The relationship between the currents and voltages at nodes $k1$, $k2$, $k3$, $k4$, $m1$, $m2$, $m3$, and $m4$ and the primary and secondary nodal currents and voltages in (2.57) and (2.58) can be rewritten as

$$I_{node} = A^{\mathrm{T}} I_n \tag{2.59}$$

$$V_n = A V_{node} \tag{2.60}$$

where I_{node}, V_{node}, and A are defined by

$$I_{node} = \begin{bmatrix} I_{k1} \\ I_{k2} \\ I_{k3} \\ I_{k4} \\ I_{m1} \\ I_{m2} \\ I_{m3} \\ I_{m4} \end{bmatrix} \tag{2.61}$$

$$V_{node} = \begin{bmatrix} V_{k1} \\ V_{k2} \\ V_{k3} \\ V_{k4} \\ V_{m1} \\ V_{m2} \\ V_{m3} \\ V_{m4} \end{bmatrix} \tag{2.62}$$

$$A = \begin{bmatrix} 1 & 0 & 0 & -1 & 0 & 0 & 0 & 0 \\ 0 & 1 & 0 & -1 & 0 & 0 & 0 & 0 \\ 0 & 0 & 1 & -1 & 0 & 0 & 0 & 0 \\ 0 & 0 & 0 & 0 & 1 & 0 & 0 & -1 \\ 0 & 0 & 0 & 0 & 0 & 1 & 0 & -1 \\ 0 & 0 & 0 & 0 & 0 & 0 & 1 & -1 \end{bmatrix} \tag{2.63}$$

The nodal admittance equation of the transformer is obtained from (2.56), (2.59), and (2.60) as follows:

$$I_{node} = A^{\mathrm{T}} N^{\mathrm{T}} B^{\mathrm{T}} Z_b^{-1} B N A V_{node} \tag{2.64}$$

The incidence matrix of the wye-wye transformer is defined by

$$T = BNA \tag{2.65}$$

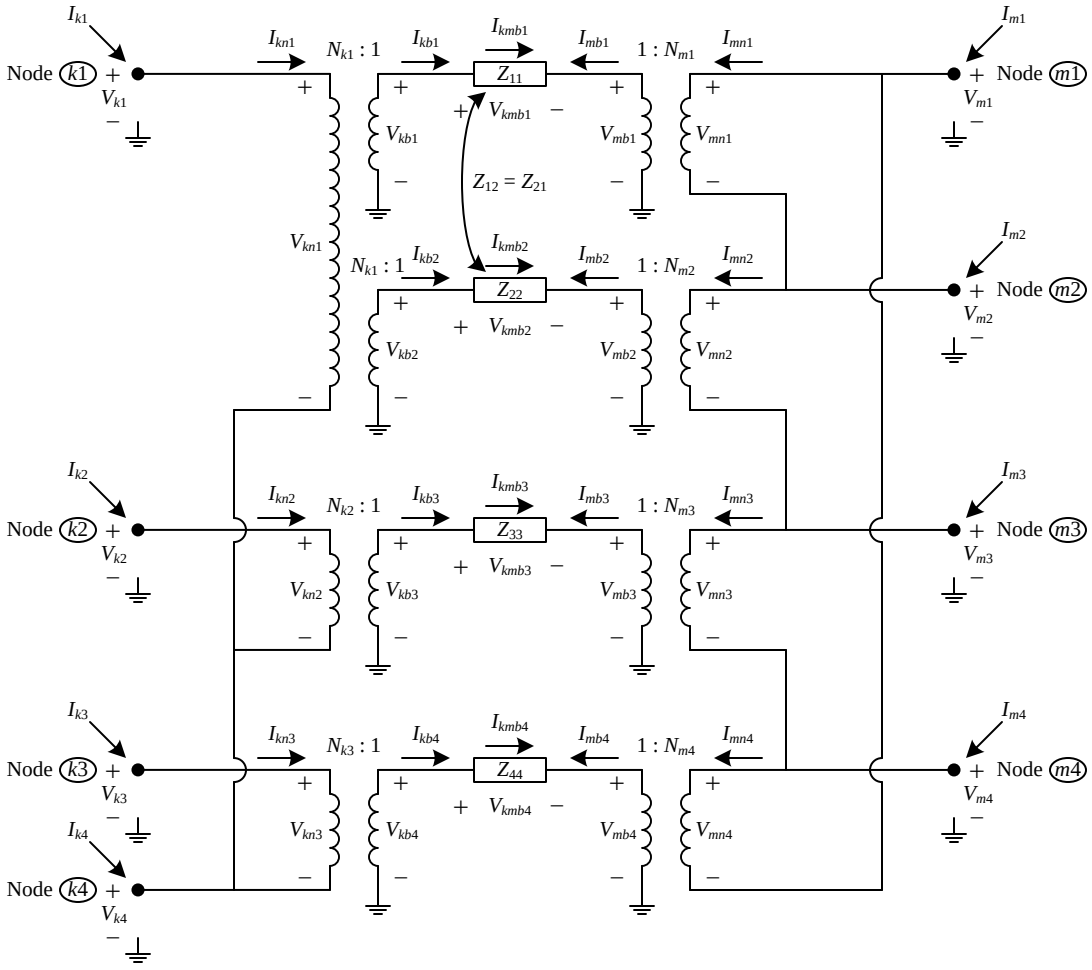

Figure 2.7: Configuration of a wye-delta-center-tapped transformer

where T is the incidence matrix of the wye-wye transformer. The nodal admittance equation of the transformer in (2.64) becomes

$$I_{node} = T^{\mathrm{T}} Z_b^{-1} T V_{node} \tag{2.66}$$

A wye-delta-center-tapped transformer can be represented by a single-phase three-winding transformer and two single-phase two-winding transformers as shown in Fig. 2.7. The branch equation of the transformer impedances is given by

$$\begin{bmatrix} I_{kmb1} \\ I_{kmb2} \\ I_{kmb3} \\ I_{kmb4} \end{bmatrix} = \begin{bmatrix} Z_{11} & Z_{12} & Z_{13} & Z_{14} \\ Z_{21} & Z_{22} & Z_{23} & Z_{24} \\ Z_{31} & Z_{32} & Z_{33} & Z_{34} \\ Z_{41} & Z_{42} & Z_{43} & Z_{44} \end{bmatrix}^{-1} \begin{bmatrix} V_{kmb1} \\ V_{kmb2} \\ V_{kmb3} \\ V_{kmb4} \end{bmatrix} \tag{2.67}$$

Note that Z_{13}, Z_{14}, Z_{23}, Z_{24}, Z_{31}, Z_{32}, Z_{34}, Z_{41}, Z_{42}, and Z_{43} are zero when there is no coupling among the single-phase transformers. However, Z_{12} and Z_{21} are not zero because of the coupling among the windings of the three-winding transformer. The branch equation for the transformer impedances in (2.67) can be rewritten as

$$I_{kmb} = Z_b^{-1} V_{kmb} \tag{2.68}$$

where I_{kmb}, V_{kmb}, and Z_b are defined by

$$I_{kmb} = \begin{bmatrix} I_{kmb1} \\ I_{kmb2} \\ I_{kmb3} \\ I_{kmb4} \end{bmatrix} \tag{2.69}$$

$$V_{kmb} = \begin{bmatrix} V_{kmb1} \\ V_{kmb2} \\ V_{kmb3} \\ V_{kmb4} \end{bmatrix} \tag{2.70}$$

$$Z_b = \begin{bmatrix} Z_{11} & Z_{12} & Z_{13} & Z_{14} \\ Z_{21} & Z_{22} & Z_{23} & Z_{24} \\ Z_{31} & Z_{32} & Z_{33} & Z_{34} \\ Z_{41} & Z_{42} & Z_{43} & Z_{44} \end{bmatrix} \tag{2.71}$$

The currents injected to the transformer impedances at 1-V base are calculated from the branch currents as follows:

$$\begin{bmatrix} I_{kb1} \\ I_{kb2} \\ I_{kb3} \\ I_{kb4} \\ I_{mb1} \\ I_{mb2} \\ I_{mb3} \\ I_{mb4} \end{bmatrix} = \begin{bmatrix} I_{kmb1} \\ I_{kmb2} \\ I_{kmb3} \\ I_{kmb4} \\ -I_{kmb1} \\ -I_{kmb2} \\ -I_{kmb3} \\ -I_{kmb4} \end{bmatrix} = \begin{bmatrix} 1 & 0 & 0 & 0 \\ 0 & 1 & 0 & 0 \\ 0 & 0 & 1 & 0 \\ 0 & 0 & 0 & 1 \\ -1 & 0 & 0 & 0 \\ 0 & -1 & 0 & 0 \\ 0 & 0 & -1 & 0 \\ 0 & 0 & 0 & -1 \end{bmatrix} \begin{bmatrix} I_{kmb1} \\ I_{kmb2} \\ I_{kmb3} \\ I_{kmb4} \end{bmatrix} \tag{2.72}$$

The branch voltages of the transformer impedances are calculated from the nodal voltages at 1-V base as follows:

$$\begin{bmatrix} V_{kmb1} \\ V_{kmb2} \\ V_{kmb3} \\ V_{kmb4} \end{bmatrix} = \begin{bmatrix} V_{kb1} - V_{mb1} \\ V_{kb2} - V_{mb2} \\ V_{kb3} - V_{mb3} \\ V_{kb4} - V_{mb4} \end{bmatrix} = \begin{bmatrix} 1 & 0 & 0 & 0 & -1 & 0 & 0 & 0 \\ 0 & 1 & 0 & 0 & 0 & -1 & 0 & 0 \\ 0 & 0 & 1 & 0 & 0 & 0 & -1 & 0 \\ 0 & 0 & 0 & 1 & 0 & 0 & 0 & -1 \end{bmatrix} \begin{bmatrix} V_{kb1} \\ V_{kb2} \\ V_{kb3} \\ V_{kb4} \\ V_{mb1} \\ V_{mb2} \\ V_{mb3} \\ V_{mb4} \end{bmatrix} \tag{2.73}$$

The relationship between the nodal and branch currents and voltages (at 1-V base) of the transformer impedances in (2.72) and (2.73) can be rewritten as

$$I_b = B^{\mathrm{T}} I_{kmb} \tag{2.74}$$

$$V_{kmb} = B V_b \tag{2.75}$$

where I_b, V_b, and B are defined by

$$I_b = \begin{bmatrix} I_{kb1} \\ I_{kb2} \\ I_{kb3} \\ I_{kb4} \\ I_{mb1} \\ I_{mb2} \\ I_{mb3} \\ I_{mb4} \end{bmatrix} \tag{2.76}$$

$$V_b = \begin{bmatrix} V_{kb1} \\ V_{kb2} \\ V_{kb3} \\ V_{kb4} \\ V_{mb1} \\ V_{mb2} \\ V_{mb3} \\ V_{mb4} \end{bmatrix} \tag{2.77}$$

$$B = \begin{bmatrix} 1 & 0 & 0 & 0 & -1 & 0 & 0 & 0 \\ 0 & 1 & 0 & 0 & 0 & -1 & 0 & 0 \\ 0 & 0 & 1 & 0 & 0 & 0 & -1 & 0 \\ 0 & 0 & 0 & 1 & 0 & 0 & 0 & -1 \end{bmatrix} \tag{2.78}$$

The nodal admittance equation of the transformer impedance at 1-V base is obtained from (2.68), (2.74), and (2.75) as follows:

$$I_b = B^{\mathrm{T}} Z_b^{-1} B V_b \tag{2.79}$$

The currents injected to the primary and secondary of the transformer are calculated from the currents injected to the transformer impedances at 1-V base as follows:

$$\begin{bmatrix} I_{kn1} \\ I_{kn2} \\ I_{kn3} \\ I_{mn1} \\ I_{mn2} \\ I_{mn3} \\ I_{mn4} \end{bmatrix} = \begin{bmatrix} \frac{I_{kb1}+I_{kb2}}{N_{k1}} \\ \frac{I_{kb3}}{N_{k2}} \\ \frac{I_{kb4}}{N_{k3}} \\ \frac{I_{mb1}}{N_{m1}} \\ \frac{I_{mb2}}{N_{m2}} \\ \frac{I_{mb3}}{N_{m3}} \\ \frac{I_{mb4}}{N_{m4}} \end{bmatrix} = \begin{bmatrix} \frac{1}{N_{k1}} & \frac{1}{N_{k1}} & 0 & 0 & 0 & 0 & 0 & 0 \\ 0 & 0 & \frac{1}{N_{k2}} & 0 & 0 & 0 & 0 & 0 \\ 0 & 0 & 0 & \frac{1}{N_{k3}} & 0 & 0 & 0 & 0 \\ 0 & 0 & 0 & 0 & \frac{1}{N_{m1}} & 0 & 0 & 0 \\ 0 & 0 & 0 & 0 & 0 & \frac{1}{N_{m2}} & 0 & 0 \\ 0 & 0 & 0 & 0 & 0 & 0 & \frac{1}{N_{m3}} & 0 \\ 0 & 0 & 0 & 0 & 0 & 0 & 0 & \frac{1}{N_{m4}} \end{bmatrix} \begin{bmatrix} I_{kb1} \\ I_{kb2} \\ I_{kb3} \\ I_{kb4} \\ I_{mb1} \\ I_{mb2} \\ I_{mb3} \\ I_{mb4} \end{bmatrix} \tag{2.80}$$

The nodal voltages at 1-V base are calculated from the primary and secondary nodal voltages as follows:

$$\begin{bmatrix} V_{kb1} \\ V_{kb2} \\ V_{kb3} \\ V_{kb4} \\ V_{mb1} \\ V_{mb2} \\ V_{mb3} \\ V_{mb4} \end{bmatrix} = \begin{bmatrix} \frac{V_{kn1}}{N_{k1}} \\ \frac{V_{kn1}}{N_{k1}} \\ \frac{V_{kn2}}{N_{k2}} \\ \frac{V_{kn3}}{N_{k3}} \\ \frac{V_{mn1}}{N_{m1}} \\ \frac{V_{mn2}}{N_{m2}} \\ \frac{V_{mn3}}{N_{m3}} \\ \frac{V_{mn4}}{N_{m4}} \end{bmatrix} = \begin{bmatrix} \frac{1}{N_{k1}} & 0 & 0 & 0 & 0 & 0 & 0 \\ \frac{1}{N_{k1}} & 0 & 0 & 0 & 0 & 0 & 0 \\ 0 & \frac{1}{N_{k2}} & 0 & 0 & 0 & 0 & 0 \\ 0 & 0 & \frac{1}{N_{k3}} & 0 & 0 & 0 & 0 \\ 0 & 0 & 0 & \frac{1}{N_{m1}} & 0 & 0 & 0 \\ 0 & 0 & 0 & 0 & \frac{1}{N_{m2}} & 0 & 0 \\ 0 & 0 & 0 & 0 & 0 & \frac{1}{N_{m3}} & 0 \\ 0 & 0 & 0 & 0 & 0 & 0 & \frac{1}{N_{m4}} \end{bmatrix} \begin{bmatrix} V_{kn1} \\ V_{kn2} \\ V_{kn3} \\ V_{mn1} \\ V_{mn2} \\ V_{mn3} \\ V_{mn4} \end{bmatrix} \tag{2.81}$$

The relationship between the primary and secondary nodal currents and voltages and the nodal currents and voltages at 1-V base in (2.80) and (2.81) can be rewritten as

$$I_n = N^{\mathrm{T}} I_b \tag{2.82}$$

$$V_b = N V_n \tag{2.83}$$

where I_n, V_n, and N are defined by

$$I_n = \begin{bmatrix} I_{kn1} \\ I_{kn2} \\ I_{kn3} \\ I_{mn1} \\ I_{mn2} \\ I_{mn3} \\ I_{mn4} \end{bmatrix} \tag{2.84}$$

$$V_n = \begin{bmatrix} V_{kn1} \\ V_{kn2} \\ V_{kn3} \\ V_{mn1} \\ V_{mn2} \\ V_{mn3} \\ V_{mn4} \end{bmatrix} \tag{2.85}$$

$$N = \begin{bmatrix} \frac{1}{N_{k1}} & 0 & 0 & 0 & 0 & 0 & 0 \\ \frac{1}{N_{k1}} & 0 & 0 & 0 & 0 & 0 & 0 \\ 0 & \frac{1}{N_{k2}} & 0 & 0 & 0 & 0 & 0 \\ 0 & 0 & \frac{1}{N_{k3}} & 0 & 0 & 0 & 0 \\ 0 & 0 & 0 & \frac{1}{N_{m1}} & 0 & 0 & 0 \\ 0 & 0 & 0 & 0 & \frac{1}{N_{m2}} & 0 & 0 \\ 0 & 0 & 0 & 0 & 0 & \frac{1}{N_{m3}} & 0 \\ 0 & 0 & 0 & 0 & 0 & 0 & \frac{1}{N_{m4}} \end{bmatrix} \tag{2.86}$$

The nodal admittance equation of the transformer at the primary and secondary is obtained from (2.79), (2.82), and (2.83) as follows:

$$I_n = N^{\mathrm{T}} B^{\mathrm{T}} Z_b^{-1} B N V_n \tag{2.87}$$

The currents injected to nodes $k1$, $k2$, $k3$, $k4$, $m1$, $m2$, $m3$, and $m4$ are calculated from the currents injected to the primary and secondary of the transformer as follows:

$$\begin{bmatrix} I_{k1} \\ I_{k2} \\ I_{k3} \\ I_{k4} \\ I_{m1} \\ I_{m2} \\ I_{m3} \\ I_{m4} \end{bmatrix} = \begin{bmatrix} I_{kn1} \\ I_{kn2} \\ I_{kn3} \\ -I_{kn1} - I_{kn2} - I_{kn3} \\ I_{mn1} - I_{mn4} \\ I_{mn2} - I_{mn1} \\ I_{mn3} - I_{mn2} \\ I_{mn4} - I_{mn3} \end{bmatrix} = \begin{bmatrix} 1 & 0 & 0 & 0 & 0 & 0 & 0 \\ 0 & 1 & 0 & 0 & 0 & 0 & 0 \\ 0 & 0 & 1 & 0 & 0 & 0 & 0 \\ -1 & -1 & -1 & 0 & 0 & 0 & 0 \\ 0 & 0 & 0 & 1 & 0 & 0 & -1 \\ 0 & 0 & 0 & -1 & 1 & 0 & 0 \\ 0 & 0 & 0 & 0 & -1 & 1 & 0 \\ 0 & 0 & 0 & 0 & 0 & -1 & 1 \end{bmatrix} \begin{bmatrix} I_{kn1} \\ I_{kn2} \\ I_{kn3} \\ I_{mn1} \\ I_{mn2} \\ I_{mn3} \\ I_{mn4} \end{bmatrix} \tag{2.88}$$

The primary and secondary nodal voltages are calculated from the voltages at nodes $k1$, $k2$, $k3$, $k4$, $m1$, $m2$, $m3$, and $m4$ as follows:

$$\begin{bmatrix} V_{kn1} \\ V_{kn2} \\ V_{kn3} \\ V_{mn1} \\ V_{mn2} \\ V_{mn3} \end{bmatrix} = \begin{bmatrix} V_{k1} - V_{k4} \\ V_{k2} - V_{k4} \\ V_{k3} - V_{k4} \\ V_{m1} - V_{m2} \\ V_{m2} - V_{m3} \\ V_{m3} - V_{m4} \\ V_{m4} - V_{m1} \end{bmatrix} = \begin{bmatrix} 1 & 0 & 0 & -1 & 0 & 0 & 0 & 0 \\ 0 & 1 & 0 & -1 & 0 & 0 & 0 & 0 \\ 0 & 0 & 1 & -1 & 0 & 0 & 0 & 0 \\ 0 & 0 & 0 & 0 & 1 & -1 & 0 & 0 \\ 0 & 0 & 0 & 0 & 0 & 1 & -1 & 0 \\ 0 & 0 & 0 & 0 & 0 & 0 & 1 & -1 \\ 0 & 0 & 0 & 0 & -1 & 0 & 0 & 1 \end{bmatrix} \begin{bmatrix} V_{k1} \\ V_{k2} \\ V_{k3} \\ V_{k4} \\ V_{m1} \\ V_{m2} \\ V_{m3} \\ V_{m4} \end{bmatrix} \tag{2.89}$$

The relationship between the currents and voltages at nodes $k1$, $k2$, $k3$, $k4$, $m1$, $m2$, $m3$, and $m4$ and the primary and secondary nodal currents and voltages in (2.88) and (2.89) can be rewritten as

$$I_{node} = A^{\mathrm{T}} I_n \tag{2.90}$$

$$V_n = A V_{node} \tag{2.91}$$

where I_{node}, V_{node}, and A are defined by

$$I_{node} = \begin{bmatrix} I_{k1} \\ I_{k2} \\ I_{k3} \\ I_{k4} \\ I_{m1} \\ I_{m2} \\ I_{m3} \\ I_{m4} \end{bmatrix} \tag{2.92}$$

$$V_{node} = \begin{bmatrix} V_{k1} \\ V_{k2} \\ V_{k3} \\ V_{k4} \\ V_{m1} \\ V_{m2} \\ V_{m3} \\ V_{m4} \end{bmatrix} \tag{2.93}$$

$$A = \begin{bmatrix} 1 & 0 & 0 & -1 & 0 & 0 & 0 & 0 \\ 0 & 1 & 0 & -1 & 0 & 0 & 0 & 0 \\ 0 & 0 & 1 & -1 & 0 & 0 & 0 & 0 \\ 0 & 0 & 0 & 0 & 1 & -1 & 0 & 0 \\ 0 & 0 & 0 & 0 & 0 & 1 & -1 & 0 \\ 0 & 0 & 0 & 0 & 0 & 0 & 1 & -1 \\ 0 & 0 & 0 & 0 & -1 & 0 & 0 & 1 \end{bmatrix} \tag{2.94}$$

The nodal admittance equation of the transformer is obtained from (2.87), (2.90), and (2.91) as follows:

$$I_{node} = A^{\mathrm{T}} N^{\mathrm{T}} B^{\mathrm{T}} Z_b^{-1} B N A V_{node} \tag{2.95}$$

The incidence matrix of the wye-delta-center-tapped transformer is defined by

$$T = BNA \tag{2.96}$$

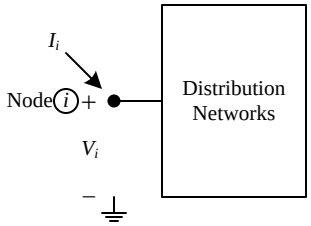

Figure 2.8: Injected currents and node voltages

where T is the incidence matrix of the wye-delta-center-tapped transformer. The nodal admittance equation of the transformer in (2.95) becomes

$$I_{node} = T^{\mathrm{T}} Z_b^{-1} T V_{node} \tag{2.97}$$

2.1.4 Distribution Network Solution

The admittance matrices of each equipment are then combined to obtain the nodal admittance matrix of the distribution network. For three-phase systems, one bus has four nodes, i.e., Phase A, Phase B, Phase C, and ground nodes. The admittance matrix of the distribution network relates voltages at each node and currents injected into each node (Fig. 2.8) as follows:

$$I = Y_{bus} V \tag{2.98}$$

where Y_{bus} is a nodal admittance matrix. For a circuit having n nodes, a vector of injected currents, I, and a vector of nod voltages, V, are defined as follows:

$$I = \begin{bmatrix} I_1 \\ \vdots \\ I_i \\ \vdots \\ I_n \end{bmatrix} \tag{2.99}$$

$$V = \begin{bmatrix} V_1 \\ \vdots \\ V_i \\ \vdots \\ V_n \end{bmatrix} \tag{2.100}$$

where I_i is current injected into node i, and V_i is voltage at node i.

For each node, only one variable, either voltage or current, is known, while the other variable is not known. Therefore, (2.98) can be written as

$$\begin{bmatrix} I_{unknown} \\ I_{known} \end{bmatrix} = \begin{bmatrix} Y_{bus,a} & Y_{bus,b} \\ Y_{bus,c} & Y_{bus,d} \end{bmatrix} \begin{bmatrix} V_{known} \\ V_{unknown} \end{bmatrix} \tag{2.101}$$

The unknown voltages and currents can be obtained from

$$\begin{bmatrix} I_{unknown} \\ V_{unknown} \end{bmatrix} = \begin{bmatrix} Y_{bus,a} - Y_{bus,b}Y_{bus,d}^{-1}Y_{bus,c} & Y_{bus,b}Y_{bus,d}^{-1} \\ -Y_{bus,d}^{-1}Y_{bus,c} & Y_{bus,d}^{-1} \end{bmatrix} \begin{bmatrix} V_{known} \\ I_{known} \end{bmatrix} \tag{2.102}$$

2.2 Electromechanical Transient Model

Distribution networks consisting of distribution feeders, transformers, capacitor banks, and constant impedance loads contain only dynamics associated with electromagnetic transients (inductors and capacitors), but the networks have no dynamics associated with electromechanical transients because the distribution networks do not have any mechanical components. Since the electromagnetic transient dynamics are neglected in the electromechanical transient models, the electromechanical transient models of distribution networks are simply the steady-state models.

2.3 Electromagnetic Transient Model

Distribution networks including distribution feeders, transformers, capacitor banks, and constant impedance loads are modeled by using the EMTP based approach

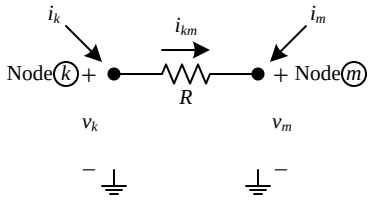

Figure 2.9: Equivalent impedance network of a resistor

[48, 49]. In this approach, the differential equations representing each element in the distribution network in a time domain are integrated via the trapezoidal method and become algebraic equations. Then, the algebraic equations are rearranged to describe the relation between the node voltage and injected current at each terminal of the equipment (nodal equation). The following sections describe the approach used to build the nodal admittance matrix for resistors, inductors, capacitors, distribution lines, and transformers [48, 49, 60].

2.3.1 Resistor Model

The branch equation for a resistor is given by

$$i_{km} = \frac{1}{R}\left(v_k - v_m\right) \tag{2.103}$$

The nodal equation for a resistor is

$$\begin{bmatrix} i_k\left(t\right) \\ i_m\left(t\right) \end{bmatrix} = \begin{bmatrix} \frac{1}{R} & -\frac{1}{R} \\ -\frac{1}{R} & \frac{1}{R} \end{bmatrix} \begin{bmatrix} v_k\left(t\right) \\ v_m\left(t\right) \end{bmatrix} \tag{2.104}$$

The equivalent impedance network of a resistor is shown in Fig. 2.9.

2.3.2 Inductor Model

The branch equation for an inductor is given by

$$i_{km}\left(t\right) = \frac{1}{L}\int_{t-\Delta t}^{t}\left(v_k - v_m\right)dt + i_{km}\left(t - \Delta t\right) \tag{2.105}$$

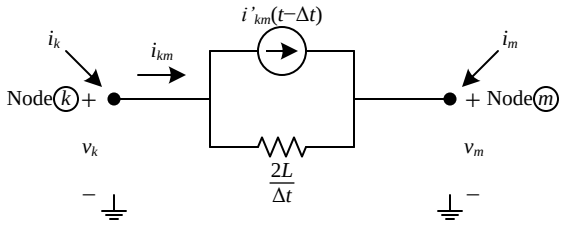

Figure 2.10: Equivalent impedance network of an inductor

Applying the trapezoidal method yields

$$i_{km}(t) = \frac{\Delta t}{2L}\left[v_k(t) - v_m(t)\right] + i'_{km}(t - \Delta t) \tag{2.106}$$

where the history term is defined as

$$i'_{km}(t - \Delta t) = i_{km}(t - \Delta t) + \frac{\Delta t}{2L}\left[v_k(t - \Delta t) - v_m(t - \Delta t)\right] \tag{2.107}$$

Substituting $i_{km}(t - \Delta t)$ from (2.106) into (2.107) yields

$$i'_{km}(t - \Delta t) = i'_{km}(t - 2\Delta t) + 2\left(\frac{\Delta t}{2L}\right)\left[v_k(t - \Delta t) - v_m(t - \Delta t)\right] \tag{2.108}$$

The nodal equation for an inductor is

$$\begin{bmatrix} i_k(t) \\ i_m(t) \end{bmatrix} = \begin{bmatrix} \frac{\Delta t}{2L} & -\frac{\Delta t}{2L} \\ -\frac{\Delta t}{2L} & \frac{\Delta t}{2L} \end{bmatrix} \begin{bmatrix} v_k(t) \\ v_m(t) \end{bmatrix} + \begin{bmatrix} i'_{km}(t - \Delta t) \\ -i'_{km}(t - \Delta t) \end{bmatrix} \tag{2.109}$$

The equivalent impedance network of an inductor is shown in Fig. 2.10.

2.3.3 Capacitor Model

The branch equation for a capacitor is given by

$$v_k(t) - v_m(t) = \frac{1}{C}\int_{t-\Delta t}^{t} i_{km}dt + v_k(t - \Delta t) - v_m(t - \Delta t) \tag{2.110}$$

Applying the trapezoidal method yields

$$i_{km}(t) = \frac{2C}{\Delta t}\left[v_k(t) - v_m(t)\right] + i'_{km}(t - \Delta t) \tag{2.111}$$

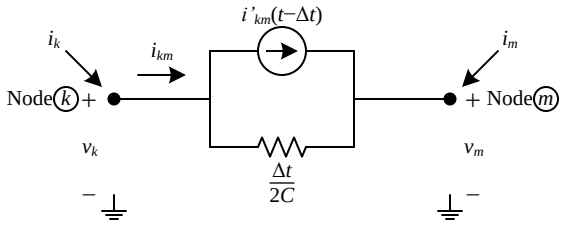

Figure 2.11: Equivalent impedance network of a capacitor

where the history term is defined as

$$i'_{km}(t-\Delta t) = -i_{km}(t-\Delta t) - \frac{2C}{\Delta t}\left[v_k(t-\Delta t) - v_m(t-\Delta t)\right] \tag{2.112}$$

Substituting $i_{km}(t-\Delta t)$ from (2.111) into (2.112) yields

$$i'_{km}(t-\Delta t) = -i'_{km}(t-2\Delta t) - 2\left(\frac{2C}{\Delta t}\right)\left[v_k(t-\Delta t) - v_m(t-\Delta t)\right] \tag{2.113}$$

The nodal equation for a capacitor is

$$\begin{bmatrix} i_k(t) \\ i_m(t) \end{bmatrix} = \begin{bmatrix} \frac{2C}{\Delta t} & -\frac{2C}{\Delta t} \\ -\frac{2C}{\Delta t} & \frac{2C}{\Delta t} \end{bmatrix} \begin{bmatrix} v_k(t) \\ v_m(t) \end{bmatrix} + \begin{bmatrix} i'_{km}(t-\Delta t) \\ -i'_{km}(t-\Delta t) \end{bmatrix} \tag{2.114}$$

The equivalent impedance network of a capacitor is shown in Fig. 2.11.

2.3.4 Distribution Line Model

A distribution line is represented by the traveling wave model. For a single-phase lossless line, the traveling wave equations are

$$\frac{\partial v}{\partial x} = -l\frac{\partial i}{\partial t} \tag{2.115}$$

$$\frac{\partial i}{\partial x} = -c\frac{\partial v}{\partial t} \tag{2.116}$$

where l is the inductance per unit length of the line, and c is the capacitance per unit length of the line. Solving the traveling wave equations yields

$$i_k(t) = \frac{1}{Z_c}v_k(t) + i'_k(t-\tau) \tag{2.117}$$

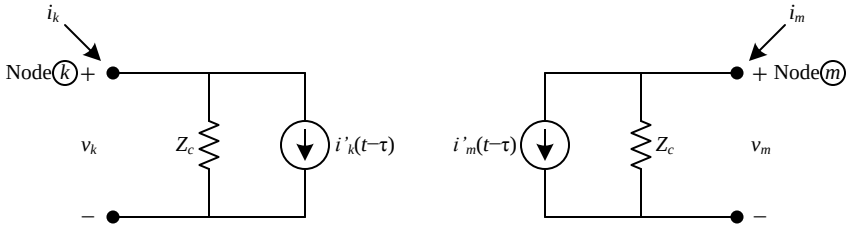

Figure 2.12: Equivalent impedance network of a single-phase lossless line

$$i_m(t) = \frac{1}{Z_c} v_m(t) + i'_m(t-\tau) \tag{2.118}$$

where Z_c is the surge impedance of the line, and τ is the travel time of the line. Z_c and τ are calculated as follows:

$$Z_c = \sqrt{\frac{l}{c}} \tag{2.119}$$

$$\tau = d\sqrt{lc} \tag{2.120}$$

where d is the length of the line. The history terms are defined as

$$i'_k(t-\tau) = -i_m(t-\tau) - \frac{1}{Z_c} v_m(t-\tau) \tag{2.121}$$

$$i'_m(t-\tau) = -i_k(t-\tau) - \frac{1}{Z_c} v_k(t-\tau) \tag{2.122}$$

Substituting $i_k(t-\tau)$ and $i_m(t-\tau)$ from (2.117) and (2.118) into (2.121) and (2.122) yields

$$i'_k(t-\tau) = -i'_m(t-2\tau) - \frac{2}{Z_c} v_m(t-\tau) \tag{2.123}$$

$$i'_m(t-\tau) = -i'_k(t-2\tau) - \frac{2}{Z_c} v_k(t-\tau) \tag{2.124}$$

The nodal equation for a single-phase lossless line is given by

$$\begin{bmatrix} i_k(t) \\ i_m(t) \end{bmatrix} = \begin{bmatrix} \frac{1}{Z_c} & 0 \\ 0 & \frac{1}{Z_c} \end{bmatrix} \begin{bmatrix} v_k(t) \\ v_m(t) \end{bmatrix} + \begin{bmatrix} i'_k(t-\tau) \\ i'_m(t-\tau) \end{bmatrix} \tag{2.125}$$

The equivalent impedance network of a single-phase lossless line is shown in Fig. 2.12.

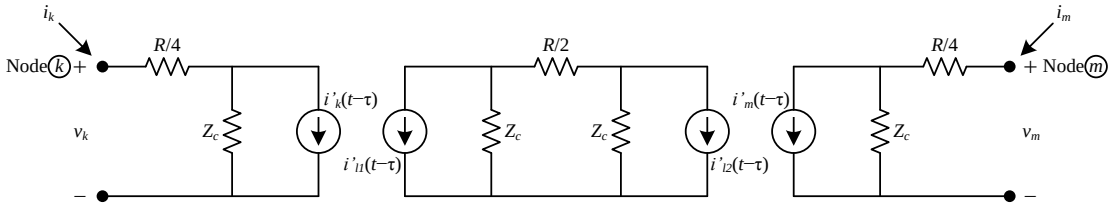

Figure 2.13: Impedance network of a single-phase lossy line

For a single-phase lossy line, the shunt conductances are assumed to be negligible, and the series resistances are lumped to $\frac{R}{4}$ at the ends and $\frac{R}{2}$ in the middle of the line as shown in Fig. 2.13. Note that R is the total series resistance. The currents $i_k(t)$ and $i_m(t)$ become

$$i_k(t) = \frac{1}{Z_c + \frac{R}{4}} v_k(t) + i'_k(t-\tau) \tag{2.126}$$

$$i_m(t) = \frac{1}{Z_c + \frac{R}{4}} v_m(t) + i'_m(t-\tau) \tag{2.127}$$

where the history terms are defined as

$$\begin{aligned} i'_k(t-\tau) = &-\frac{Z_c}{\left(Z_c + \frac{R}{4}\right)^2}\left[\left(Z_c - \frac{R}{4}\right) i_m(t-\tau) + v_m(t-\tau)\right] \\ &+ \frac{\frac{R}{4}}{\left(Z_c + \frac{R}{4}\right)^2}\left[\left(Z_c - \frac{R}{4}\right) i_k(t-\tau) + v_k(t-\tau)\right] \end{aligned} \tag{2.128}$$

$$\begin{aligned} i'_m(t-\tau) = &-\frac{Z_c}{\left(Z_c + \frac{R}{4}\right)^2}\left[\left(Z_c - \frac{R}{4}\right) i_k(t-\tau) + v_k(t-\tau)\right] \\ &+ \frac{\frac{R}{4}}{\left(Z_c + \frac{R}{4}\right)^2}\left[\left(Z_c - \frac{R}{4}\right) i_m(t-\tau) + v_m(t-\tau)\right] \end{aligned} \tag{2.129}$$

Substituting $i_k(t-\tau)$ and $i_m(t-\tau)$ from (2.126) and (2.127) into (2.128) and (2.129)

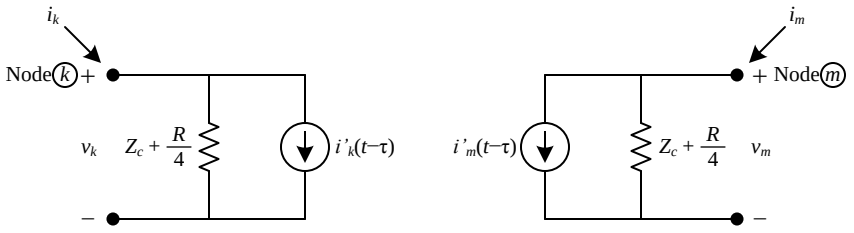

Figure 2.14: Equivalent impedance network of a single-phase lossy line

yields

$$i'_k(t-\tau) = -\frac{Z_c}{\left(Z_c+\frac{R}{4}\right)^2}\left[\left(Z_c-\frac{R}{4}\right)i'_m(t-2\tau)+\frac{2Z_c}{Z_c+\frac{R}{4}}v_m(t-\tau)\right] + \frac{\frac{R}{4}}{\left(Z_c+\frac{R}{4}\right)^2}\left[\left(Z_c-\frac{R}{4}\right)i'_k(t-2\tau)+\frac{2Z_c}{Z_c+\frac{R}{4}}v_k(t-\tau)\right] \quad (2.130)$$

$$i'_m(t-\tau) = -\frac{Z_c}{\left(Z_c+\frac{R}{4}\right)^2}\left[\left(Z_c-\frac{R}{4}\right)i'_k(t-2\tau)+\frac{2Z_c}{Z_c+\frac{R}{4}}v_k(t-\tau)\right] + \frac{\frac{R}{4}}{\left(Z_c+\frac{R}{4}\right)^2}\left[\left(Z_c-\frac{R}{4}\right)i'_m(t-2\tau)+\frac{2Z_c}{Z_c+\frac{R}{4}}v_m(t-\tau)\right] \quad (2.131)$$

The nodal equation for a single-phase lossy line is given by

$$\begin{bmatrix} i_k(t) \\ i_m(t) \end{bmatrix} = \begin{bmatrix} \frac{1}{Z_c+\frac{R}{4}} & 0 \\ 0 & \frac{1}{Z_c+\frac{R}{4}} \end{bmatrix} \begin{bmatrix} v_k(t) \\ v_m(t) \end{bmatrix} + \begin{bmatrix} i'_k(t-\tau) \\ i'_m(t-\tau) \end{bmatrix} \quad (2.132)$$

The equivalent impedance network of a single-phase lossy line is shown in Fig. 2.14.

For a three-phase lossless line, the traveling wave equations are

$$\frac{\partial v_{phase}}{\partial x} = -l_{phase}\frac{\partial i_{phase}}{\partial t} \quad (2.133)$$

$$\frac{\partial i_{phase}}{\partial x} = -c_{phase}\frac{\partial v_{phase}}{\partial t} \quad (2.134)$$

where l_{phase} is the matrix of inductance per unit length of the line in a phase domain, and c_{phase} is the matrix of capacitance per unit length of the line in a phase domain.

In order to solve the traveling wave equations, the modal analysis approach is used to decouple the equations for Phases A, B, and C. The phase currents and voltages are transformed to the modal currents and voltages by using the transformation matrices as follows:

$$i_{phase} = T_i i_{mode} \tag{2.135}$$

$$v_{phase} = T_v v_{mode} \tag{2.136}$$

where T_i and T_v are the transformation matrices for the current and voltage, respectively. Note that T_i is the matrix of eigenvectors of the matrix product $c_{phase}l_{phase}$, and T_v is the matrix of eigenvectors of the matrix product $l_{phase}c_{phase}$. T_i and T_v relate to each other by

$$T_i^{-1} = T_v^{\mathrm{T}} \tag{2.137}$$

The phase inductance and capacitance matrices are transformed to the modal inductance and capacitance matrices as follows:

$$l_{mode} = T_i^{\mathrm{T}} l_{phase} T_i \tag{2.138}$$

$$c_{mode} = T_v^{\mathrm{T}} c_{phase} T_v \tag{2.139}$$

where l_{mode} is the matrix of inductance per unit length of the line in a modal domain, and c_{mode} is the matrix of capacitance per unit length of the line in a modal domain. Note that both l_{mode} and c_{mode} are diagonal matrices. Solving the modal traveling wave equations yields

$$i_{k,mode}(t) = Z_{c,mode}^{-1} v_{k,mode}(t) + i'_{k,mode}(t - \tau_{mode}) \tag{2.140}$$

$$i_{m,mode}(t) = Z_{c,mode}^{-1} v_{m,mode}(t) + i'_{m,mode}(t - \tau_{mode}) \tag{2.141}$$

where $Z_{c,mode}$ is the surge impedance matrix of the line in a modal domain, and τ_{mode} is the travel time of the line. For a four-wire line, $Z_{c,mode}$ is defined by

$$Z_{c,mode} = \begin{bmatrix} Z_{c,mode,1} & 0 & 0 & 0 \\ 0 & Z_{c,mode,2} & 0 & 0 \\ 0 & 0 & Z_{c,mode,3} & 0 \\ 0 & 0 & 0 & Z_{c,mode,4} \end{bmatrix} \tag{2.142}$$

where $Z_{c,mode}$ for mode i is calculated as follows:

$$Z_{c,mode,i} = \sqrt{\frac{l_{mode,ii}}{c_{mode,ii}}} \tag{2.143}$$

τ_{mode} for mode i is calculated as follows:

$$\tau_{mode,i} = d\sqrt{\lambda_i} \tag{2.144}$$

where λ_i is the eigenvalue for mode i of the matrix product $c_{phase}l_{phase}$ or $l_{phase}c_{phase}$. Note that each mode has a different travel time. The history terms are defined as

$$i'_{k,mode}\left(t-\tau_{mode}\right) = -i_{m,mode}\left(t-\tau_{mode}\right) - Z^{-1}_{c,mode}v_{m,mode}\left(t-\tau_{mode}\right) \tag{2.145}$$

$$i'_{m,mode}\left(t-\tau_{mode}\right) = -i_{k,mode}\left(t-\tau_{mode}\right) - Z^{-1}_{c,mode}v_{k,mode}\left(t-\tau_{mode}\right) \tag{2.146}$$

Substituting $i_k\left(t-\tau_{mode}\right)$ and $i_m\left(t-\tau_{mode}\right)$ from (2.140) and (2.141) into (2.145) and (2.146) yields

$$i'_{k,mode}\left(t-\tau_{mode}\right) = -i'_{m,mode}\left(t-2\tau_{mode}\right) - 2Z^{-1}_{c,mode}v_{m,mode}\left(t-\tau_{mode}\right) \tag{2.147}$$

$$i'_{m,mode}\left(t-\tau_{mode}\right) = -i'_{k,mode}\left(t-2\tau_{mode}\right) - 2Z^{-1}_{c,mode}v_{k,mode}\left(t-\tau_{mode}\right) \tag{2.148}$$

The nodal equation for a three-phase lossless line in a modal domain is given by

$$\begin{bmatrix} i_{k,mode}\left(t\right) \\ i_{m,mode}\left(t\right) \end{bmatrix} = \begin{bmatrix} Z^{-1}_{c,mode} & 0 \\ 0 & Z^{-1}_{c,mode} \end{bmatrix} \begin{bmatrix} v_{k,mode}\left(t\right) \\ v_{m,mode}\left(t\right) \end{bmatrix} + \begin{bmatrix} i'_{k,mode}\left(t-\tau_{mode}\right) \\ i'_{m,mode}\left(t-\tau_{mode}\right) \end{bmatrix} \tag{2.149}$$

The modal currents and voltages in (2.149) are converted to the phase currents and voltages by using (2.135) and (2.136). Therefore, the nodal equation for a three-phase lossless line in a phase domain is given by

$$\begin{bmatrix} i_{k,phase}(t) \\ i_{m,phase}(t) \end{bmatrix} = \begin{bmatrix} T_i Z_{c,mode}^{-1} T_i^{\mathrm{T}} & 0 \\ 0 & T_i Z_{c,mode}^{-1} T_i^{\mathrm{T}} \end{bmatrix} \begin{bmatrix} v_{k,phase}(t) \\ v_{m,phase}(t) \end{bmatrix} + \begin{bmatrix} T_i i'_{k,mode}(t-\tau_{mode}) \\ T_i i'_{m,mode}(t-\tau_{mode}) \end{bmatrix} \tag{2.150}$$

For a three-phase lossy line, the currents $i_{k,mode}(t)$ and $i_{m,mode}(t)$ become

$$i_{k,mode}(t) = \left(Z_{c,mode} + \frac{R_{mode}}{4}\right)^{-1} v_{k,mode}(t) + i'_{k,mode}(t-\tau_{mode}) \tag{2.151}$$

$$i_{m,mode}(t) = \left(Z_{c,mode} + \frac{R_{mode}}{4}\right)^{-1} v_{m,mode}(t) + i'_{m,mode}(t-\tau_{mode}) \tag{2.152}$$

where R_{mode} is the matrix of total resistance of the line in a modal domain. The modal resistance matrix is obtained from the phase resistance matrix as follows:

$$R_{mode} = T_i^{\mathrm{T}} R_{phase} T_i \tag{2.153}$$

where R_{phase} is the matrix of total resistance of the line in a phase domain. Note that R_{mode} is not a diagonal matrix. The history terms are defined as

$$\begin{aligned} i'_{k,mode}(t-\tau_{mode}) = &- \left(Z_{c,mode} + \frac{R_{mode}}{4}\right)^{-1} Z_{c,mode} \left(Z_{c,mode} + \frac{R_{mode}}{4}\right)^{-1} \\ &\left[\left(Z_{c,mode} - \frac{R_{mode}}{4}\right) i_{m,mode}(t-\tau_{mode}) + v_{m,mode}(t-\tau_{mode})\right] \\ &+ \left(Z_{c,mode} + \frac{R_{mode}}{4}\right)^{-1} \frac{R_{mode}}{4} \left(Z_{c,mode} + \frac{R_{mode}}{4}\right)^{-1} \\ &\left[\left(Z_{c,mode} - \frac{R_{mode}}{4}\right) i_{k,mode}(t-\tau_{mode}) + v_{k,mode}(t-\tau_{mode})\right] \end{aligned} \tag{2.154}$$

$$
\begin{aligned}
i'_{m,mode}\left(t-\tau_{mode}\right) = &-\left(Z_{c,mode}+\frac{R_{mode}}{4}\right)^{-1} Z_{c,mode}\left(Z_{c,mode}+\frac{R_{mode}}{4}\right)^{-1} \\
&\left[\left(Z_{c,mode}-\frac{R_{mode}}{4}\right) i_{k,mode}\left(t-\tau_{mode}\right)+v_{k,mode}\left(t-\tau_{mode}\right)\right] \\
&+\left(Z_{c,mode}+\frac{R_{mode}}{4}\right)^{-1} \frac{R_{mode}}{4}\left(Z_{c,mode}+\frac{R_{mode}}{4}\right)^{-1} \\
&\left[\left(Z_{c,mode}-\frac{R_{mode}}{4}\right) i_{m,mode}\left(t-\tau_{mode}\right)+v_{m,mode}\left(t-\tau_{mode}\right)\right]
\end{aligned} \tag{2.155}
$$

Substituting $i_{k,mode}\left(t-\tau_{mode}\right)$ and $i_{m,mode}\left(t-\tau_{mode}\right)$ from (2.151) and (2.152) into (2.154) and (2.155) yields

$$
\begin{aligned}
i'_{k,mode}\left(t-\tau_{mode}\right) = &-\left(Z_{c,mode}+\frac{R_{mode}}{4}\right)^{-1} Z_{c,mode}\left(Z_{c,mode}+\frac{R_{mode}}{4}\right)^{-1} \\
&\left[\left(Z_{c,mode}-\frac{R_{mode}}{4}\right) i'_{m,mode}\left(t-2\tau_{mode}\right)\right. \\
&\left.+2Z_{c,mode}\left(Z_{c,mode}+\frac{R_{mode}}{4}\right)^{-1} v_{m,mode}\left(t-\tau_{mode}\right)\right] \\
&+\left(Z_{c,mode}+\frac{R_{mode}}{4}\right)^{-1} \frac{R_{mode}}{4}\left(Z_{c,mode}+\frac{R_{mode}}{4}\right)^{-1} \\
&\left[\left(Z_{c,mode}-\frac{R_{mode}}{4}\right) i'_{k,mode}\left(t-2\tau_{mode}\right)\right. \\
&\left.+2Z_{c,mode}\left(Z_{c,mode}+\frac{R_{mode}}{4}\right)^{-1} v_{k,mode}\left(t-\tau_{mode}\right)\right]
\end{aligned} \tag{2.156}
$$

$$
\begin{aligned}
i'_{m,mode}\left(t-\tau_{mode}\right) = &-\left(Z_{c,mode}+\frac{R_{mode}}{4}\right)^{-1} Z_{c,mode}\left(Z_{c,mode}+\frac{R_{mode}}{4}\right)^{-1} \\
&\left[\left(Z_{c,mode}-\frac{R_{mode}}{4}\right) i'_{k,mode}\left(t-2\tau_{mode}\right)\right. \\
&\left.+2Z_{c,mode}\left(Z_{c,mode}+\frac{R_{mode}}{4}\right)^{-1} v_{k,mode}\left(t-\tau_{mode}\right)\right] \\
&+\left(Z_{c,mode}+\frac{R_{mode}}{4}\right)^{-1} \frac{R_{mode}}{4}\left(Z_{c,mode}+\frac{R_{mode}}{4}\right)^{-1} \\
&\left[\left(Z_{c,mode}-\frac{R_{mode}}{4}\right) i'_{m,mode}\left(t-2\tau_{mode}\right)\right. \\
&\left.+2Z_{c,mode}\left(Z_{c,mode}+\frac{R_{mode}}{4}\right)^{-1} v_{m,mode}\left(t-\tau_{mode}\right)\right]
\end{aligned} \tag{2.157}
$$

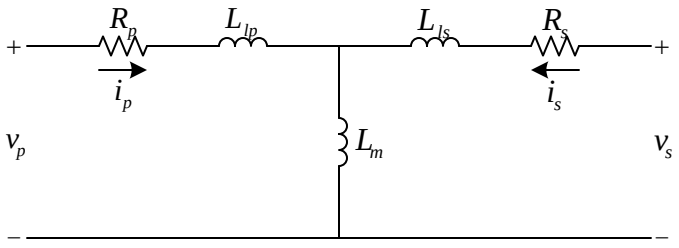

Figure 2.15: Electromagnetic transient model of a single-phase transformer

The nodal equation for a three-phase lossy line in a modal domain is given by

$$\begin{bmatrix} i_{k,mode}(t) \\ i_{m,mode}(t) \end{bmatrix} = \begin{bmatrix} \left(Z_{c,mode} + \frac{R_{mode}}{4}\right)^{-1} & 0 \\ 0 & \left(Z_{c,mode} + \frac{R_{mode}}{4}\right)^{-1} \end{bmatrix} \begin{bmatrix} v_{k,mode}(t) \\ v_{m,mode}(t) \end{bmatrix} + \begin{bmatrix} i'_{k,mode}(t - \tau_{mode}) \\ i'_{m,mode}(t - \tau_{mode}) \end{bmatrix} \tag{2.158}$$

The modal currents and voltages in (2.158) are converted to the phase currents and voltages by using (2.135) and (2.136). Therefore, the nodal equation for a three-phase lossy line in a phase domain is given by

$$\begin{bmatrix} i_{k,phase}(t) \\ i_{m,phase}(t) \end{bmatrix} = \begin{bmatrix} T_i \left(Z_{c,mode} + \frac{R_{mode}}{4}\right)^{-1} T_i^{\mathrm{T}} & 0 \\ 0 & T_i \left(Z_{c,mode} + \frac{R_{mode}}{4}\right)^{-1} T_i^{\mathrm{T}} \end{bmatrix} \begin{bmatrix} v_{k,phase}(t) \\ v_{m,phase}(t) \end{bmatrix} + \begin{bmatrix} T_i i'_{k,mode}(t - \tau_{mode}) \\ T_i i'_{m,mode}(t - \tau_{mode}) \end{bmatrix} \tag{2.159}$$

2.3.5 Transformer Model

The equivalent circuit of a single-phase transformer in an electromagnetic transient condition is shown in Fig. 2.15. The transformer model consists of voltage equations and flux linkage equations as follows: [61, 62]

The voltage equations are given by

$$v_p = R_p i_p + \frac{d}{dt}\lambda_p \tag{2.160}$$

$$v_s = R_s i_s + \frac{d}{dt}\lambda_s \tag{2.161}$$

where v_p and v_s are the primary and secondary voltages, i_p and i_s are the primary and secondary currents, λ_p and λ_s are the primary and secondary flux linkages, and R_p and R_s are the primary and secondary resistances.

The flux linkage equations are given by

$$\lambda_p = (L_{lp} + L_m)\, i_p + L_m i_s \tag{2.162}$$

$$\lambda_s = (L_{ls} + L_m)\, i_s + L_m i_p \tag{2.163}$$

where L_{lp} and L_{ls} are the primary and secondary leakage inductances, and L_m is the mutual or magnetizing inductance.

Combining the voltage equations and the flux linkage equations yields

$$v_p = R_p i_p + (L_{lp} + L_m)\, \frac{d}{dt} i_p + L_m \frac{d}{dt} i_s \tag{2.164}$$

$$v_s = R_s i_s + (L_{ls} + L_m)\, \frac{d}{dt} i_s + L_m \frac{d}{dt} i_p \tag{2.165}$$

The voltage drop across the transformer is given by

$$v_{ps} = v_p - v_s = R_p i_p - R_s i_s + L_{lp} \frac{d}{dt} i_p - L_{ls} \frac{d}{dt} i_s \tag{2.166}$$

where v_{ps} is the voltage drop across a transformer. Since L_m is much larger than L_{lp} and L_{ls}, the current flowing in L_m is neglectable. Thus, the primary and secondary currents can be approximated by

$$i_p \approx i_{ps} \tag{2.167}$$

$$i_s \approx -i_{ps} \tag{2.168}$$

where i_{ps} is the current flowing through a transformer. The voltage drop across a transformer in (2.166) becomes

$$v_{ps} = (R_p + R_s)\, i_{ps} + (L_{lp} + L_{ls})\, \frac{d}{dt} i_{ps} \tag{2.169}$$

As suggested by (2.169), a single-phase transformer can be represented by the combined winding resistances ($R = R_p + R_s$) in series with the combined leakage inductances ($L = L_p + L_s$). The branch equation for a single-phase resistance in series with a single-phase inductance is given by

$$i_{km}(t) = \frac{1}{L}\int_{t-\Delta t}^{t}(v_k - v_m)\,dt - \frac{R}{L}\int_{t-\Delta t}^{t} i_{km}dt + i_{km}(t-\Delta t) \tag{2.170}$$

Applying the trapezoidal method yields

$$i_{km}(t) = \frac{1}{R + \frac{2L}{\Delta t}}\left[v_k(t) - v_m(t)\right] + i'_{km}(t-\Delta t) \tag{2.171}$$

where the history term is defined as

$$i'_{km}(t-\Delta t) = -\frac{R - \frac{2L}{\Delta t}}{R + \frac{2L}{\Delta t}} i_{km}(t-\Delta t) + \frac{1}{R + \frac{2L}{\Delta t}}\left[v_k(t-\Delta t) - v_m(t-\Delta t)\right] \tag{2.172}$$

Substituting $i_{km}(t-\Delta t)$ from (2.171) into (2.172) yields

$$i'_{km}(t-\Delta t) = -\frac{R - \frac{2L}{\Delta t}}{R + \frac{2L}{\Delta t}} i'_{km}(t-2\Delta t) + \frac{2\left(\frac{2L}{\Delta t}\right)}{\left(R + \frac{2L}{\Delta t}\right)^2}\left[v_k(t-\Delta t) - v_m(t-\Delta t)\right] \tag{2.173}$$

The nodal equation for a single-phase resistance in series with a single-phase inductance is given by

$$\begin{bmatrix} i_k(t) \\ i_m(t) \end{bmatrix} = \begin{bmatrix} \frac{1}{R+\frac{2L}{\Delta t}} & -\frac{1}{R+\frac{2L}{\Delta t}} \\ -\frac{1}{R+\frac{2L}{\Delta t}} & \frac{1}{R+\frac{2L}{\Delta t}} \end{bmatrix} \begin{bmatrix} v_k(t) \\ v_m(t) \end{bmatrix} + \begin{bmatrix} i'_{km}(t-\Delta t) \\ -i'_{km}(t-\Delta t) \end{bmatrix} \tag{2.174}$$

The equivalent impedance network of a single-phase resistance in series with a single-phase inductance is shown in Fig. 2.16.

A three-phase transformer can be represented by a three-phase winding resistance (R) in series with a three-phase leakage inductance (L). Note that R and L are 3-by-3 matrices for a wye-wye transformer, while they are 4-by-4 matrices for a wye-delta-center-tapped transformer. The branch equation for a three-phase resistance in

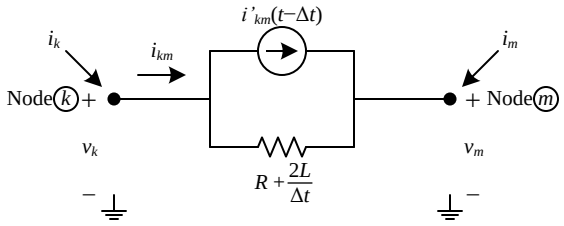

Figure 2.16: Equivalent impedance network of a resistance-inductance series branch

series with a three-phase inductance is given by

$$i_{kmb}(t) = L^{-1}\int_{t-\Delta t}^{t}(v_{kb}-v_{mb})\,dt - L^{-1}R\int_{t-\Delta t}^{t} i_{kmb}dt + i_{kmb}(t-\Delta t) \tag{2.175}$$

Applying the trapezoidal method yields

$$i_{kmb}(t) = \left(R+\frac{2L}{\Delta t}\right)^{-1}\left[v_{kb}(t)-v_{mb}(t)\right] + i'_{kmb}(t-\Delta t) \tag{2.176}$$

where the history term is defined as

$$\begin{aligned} i'_{kmb}(t-\Delta t) = &-\left(R+\frac{2L}{\Delta t}\right)^{-1}\left(R-\frac{2L}{\Delta t}\right) i_{kmb}(t-\Delta t) \\ &+\left(R+\frac{2L}{\Delta t}\right)^{-1}\left[v_{kb}(t-\Delta t)-v_{mb}(t-\Delta t)\right] \end{aligned} \tag{2.177}$$

Substituting $i_{kmb}(t-\Delta t)$ from (2.176) into (2.177) yields

$$\begin{aligned} i'_{kmb}(t-\Delta t) = &-\left(R+\frac{2L}{\Delta t}\right)^{-1}\left(R-\frac{2L}{\Delta t}\right) i'_{kmb}(t-2\Delta t) \\ &+\left[\left(R+\frac{2L}{\Delta t}\right)^{-1} - \left(R+\frac{2L}{\Delta t}\right)^{-1}\left(R-\frac{2L}{\Delta t}\right)\left(R+\frac{2L}{\Delta t}\right)^{-1}\right] \\ &\left[v_{kb}(t-\Delta t)-v_{mb}(t-\Delta t)\right] \end{aligned} \tag{2.178}$$

The nodal equation for a three-phase resistance in series with a three-phase inductance is given by

$$\begin{bmatrix} i_{kb}(t) \\ i_{mb}(t) \end{bmatrix} = \begin{bmatrix} \left(R+\frac{2L}{\Delta t}\right)^{-1} & -\left(R+\frac{2L}{\Delta t}\right)^{-1} \\ -\left(R+\frac{2L}{\Delta t}\right)^{-1} & \left(R+\frac{2L}{\Delta t}\right)^{-1} \end{bmatrix} \begin{bmatrix} v_{kb}(t) \\ v_{mb}(t) \end{bmatrix} + \begin{bmatrix} i'_{kmb}(t-\Delta t) \\ -i'_{kmb}(t-\Delta t) \end{bmatrix} \tag{2.179}$$

The relationship between the currents injected to the resistance-inductance series branch and the currents injected to the transformer and the relationship between the nodal voltages at the resistance-inductance series branch and the nodal voltages at the transformer are as follows:

$$\begin{bmatrix} i_k(t) \\ i_m(t) \end{bmatrix} = T^{\mathrm{T}} \begin{bmatrix} i_{kb}(t) \\ i_{mb}(t) \end{bmatrix} \tag{2.180}$$

$$\begin{bmatrix} v_{kb}(t) \\ v_{mb}(t) \end{bmatrix} = T \begin{bmatrix} v_k(t) \\ v_m(t) \end{bmatrix} \tag{2.181}$$

where T is an incidence matrix of the transformer defined by (2.65) and (2.96). Hence, the nodal equation for a three-phase transformer becomes

$$\begin{aligned} \begin{bmatrix} i_k(t) \\ i_m(t) \end{bmatrix} = T^{\mathrm{T}} & \begin{bmatrix} \left(R+\frac{2L}{\Delta t}\right)^{-1} & -\left(R+\frac{2L}{\Delta t}\right)^{-1} \\ -\left(R+\frac{2L}{\Delta t}\right)^{-1} & \left(R+\frac{2L}{\Delta t}\right)^{-1} \end{bmatrix} T \begin{bmatrix} v_k(t) \\ v_m(t) \end{bmatrix} \\ & + T^{\mathrm{T}} \begin{bmatrix} i'_{kmb}(t-\Delta t) \\ -i'_{kmb}(t-\Delta t) \end{bmatrix} \end{aligned} \tag{2.182}$$

2.3.6 Distribution Network Solution

The nodal equation of the system is then obtained by combining all nodal equations of elements, similar to the nodal admittance matrix for the steady-state simulation. The nodal equation of the system is in the following form

$$I(t) = YV(t) + I' \tag{2.183}$$

where Y is a nodal admittance matrix, $I(t)$ is the vector of injected currents, $V(t)$ is the vector of node voltages, and I' is the vector of known history currents. The approach used to solve (2.98) can also be used to solve (2.183). The nodal equation can be written as

$$\begin{bmatrix} I_{unknown} \\ I_{known} \end{bmatrix} = \begin{bmatrix} Y_a & Y_b \\ Y_c & Y_d \end{bmatrix} \begin{bmatrix} V_{known} \\ V_{unknown} \end{bmatrix} + \begin{bmatrix} I'_1 \\ I'_2 \end{bmatrix} \tag{2.184}$$

The unknown voltages and currents can be obtained from

$$\begin{bmatrix} I_{unknown} \\ V_{unknown} \end{bmatrix} = \begin{bmatrix} Y_a - Y_b Y_d^{-1} Y_c & Y_b Y_d^{-1} \\ -Y_d^{-1} Y_c & Y_d^{-1} \end{bmatrix} \begin{bmatrix} V_{known} \\ I_{known} - I_2' \end{bmatrix} + \begin{bmatrix} I_1' \\ 0 \end{bmatrix} \tag{2.185}$$

Chapter 3

Modeling of Renewable Energy Sources in Distribution Circuits

Distribution equipment models including distribution lines, transformers, capacitor banks, and loads have been described in Chapter 2. This chapter describes the development of models for renewable energy sources including wind turbines and PVs that are connected to distribution circuits.

3.1 Models of Wind Turbines

Wind turbines can be categorized into four technologies: a fixed-speed wind turbine (FSWT), a wide-slip wind turbine (WSWT), a doubly-fed induction generator (DFIG) wind turbine, and a full converter wind turbine [63–66]. These wind turbine technologies are commonly referred to as type-1, 2, 3, and 4 wind turbines, respectively. Each technology has a different configuration and therefore contributes differently to problems in distribution systems.

An FSWT is the simplest wind turbine technology. This configuration consists of a squirrel cage induction generator (SCIG) directly connected to the grid as shown in Fig. 3.1. This wind turbine technology is "fixed-speed" because the wind turbine always operates at almost the same rotor speed regardless of the wind speed. The generator slip is usually less than 1 %. The advantage of the FSWT is that this technology is simple, robust, and relatively inexpensive. However, the disadvantage is that the SCIG always consumes reactive power. Therefore, a capacitor bank is needed

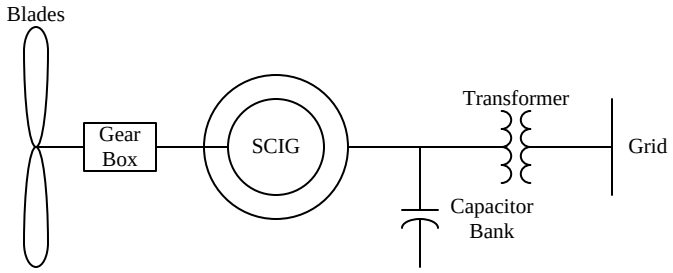

Figure 3.1: Block diagram of an FSWT

to compensate for the reactive power. Another disadvantage is that the variation of wind speed can cause high fluctuation of power output because this technology has no power control, which is the result of the fixed-speed operation.

A WSWT is one of the variable-speed wind turbine technologies. This means that the wind turbine can operate in a wide range of rotor speeds. Normally, the generator slip is up to 10-15 %. The WSWT consists of a wound rotor induction generator (WRIG) and a variable external rotor resistor as presented in Fig. 3.2. At wind speed between cut-in and rated speed, the external rotor resistance is set to zero, and the pitch angle is set to the optimum value. Thus, the WSWT works like the FSWT and also encounters the wind power fluctuation problem. To maintain constant power output between rated and cut-out wind speed, the torque-speed curve is modified using an external rotor resistor and the rotor performance characteristics are modified using a pitch angle control. Adjusting the external rotor resistance is faster than adjusting the pitch angle. However, there is a power loss due to the loss in the additional rotor resistor.

A DFIG wind turbine is also one of the variable-speed wind turbine technologies. The DFIG wind turbine consists of a WRIG and a back-to-back converter. The stator winding of a WRIG is directly connected to the grid, while the rotor wind-

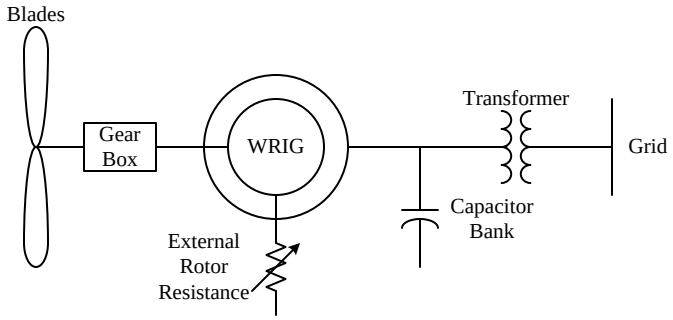

Figure 3.2: Block diagram of a WSWT

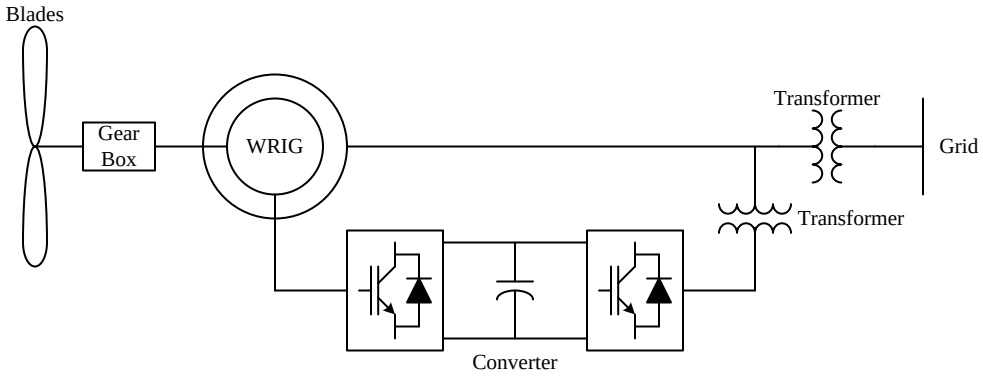

Figure 3.3: Block diagram of a DFIG wind turbine

ing is connected through a converter as illustrated in Fig. 3.3. The generator is "doubly-fed" because both stator and rotor are connected to the grid. The converter enables decoupling of real and reactive power control, which is the main advantage of the DFIG wind turbine. Since only 20-30 % of the total power passes through the converter, the required converter size is only 20-30 % of the rated power output, hence making the turbine technology relatively affordable. However, since a reduced size converter is employed, the DFIG wind turbine is able to operate in a slip range of only 20-30 %.

A full converter wind turbine is also one of the variable-speed wind turbine

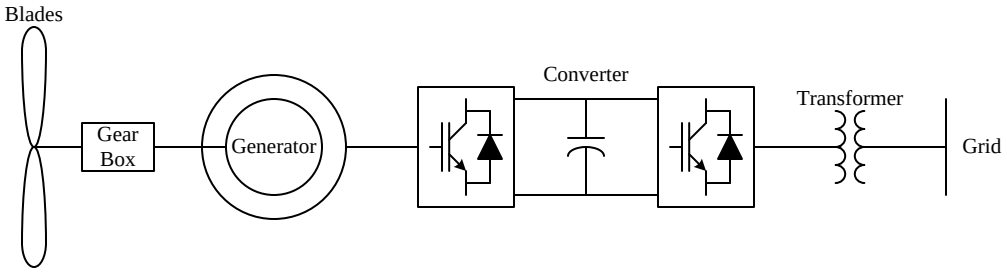

Figure 3.4: Block diagram of a full converter wind turbine

technologies. The full converter wind turbine consists of a generator and a back-to-back converter. The generator can be a synchronous generator or an induction generator. The converter is connected between the stator of the generator and the grid as described in Fig. 3.4. Like the DFIG wind turbine, the full converter wind turbine can also decouple real and reactive power control. Additionally, the full converter wind turbine can operate in a full speed range since the stator is connected to the grid via a full converter. However, a full sized converter is required, making the full converter wind turbine technology more expensive than the DFIG wind turbine technology.

A wind turbine model consists of four major parts: aerodynamic, mechanical, generator, and converter components. Each component consists of its electromagnetic transient, electromechanical transient, and steady-state models as described in the following sections.

3.1.1 Aerodynamic System

The aerodynamic system represents wind turbine blades which convert the kinetic energy available in the wind into mechanical rotational energy. The power

available in the wind P_{wind} is given by [65–69]

$$P_{wind} = \frac{1}{2}\rho A v_{wind}^3 \tag{3.1}$$

where ρ is the air density, A is the rotor swept area, and v_{wind} is the wind speed. Note that the rotor swept area is calculated by

$$A = \pi R^2 \tag{3.2}$$

where R is the blade radius.

Unfortunately, a wind turbine cannot extract all of the power available in the wind. Rotor performance characteristic C_p is defined as a ratio of the power extracted from wind P_{aero} to the power available in the wind as follows: [65–69]

$$C_p = \frac{P_{aero}}{P_{wind}} \tag{3.3}$$

According to Betz, the maximum limit of C_p is 0.593. C_p can be defined as a function of the tip speed ratio λ and the pitch angle θ. Fig. 3.5 shows a sample of the C_p curve. The tip speed ratio is a ratio of the tip speed of the blade to the wind speed as follows:

$$\lambda = \frac{\omega_{blade} R}{v_{wind}} \tag{3.4}$$

where ω_{blade} is the rotational speed of the blades referred to the blade side.

The aerodynamic torque referred to the generator side Γ'_{aero} is given by

$$\Gamma'_{aero} = \frac{P_{aero}}{\omega'_{blade}} \tag{3.5}$$

where ω'_{blade} is the rotational speed of the blades referred to the generator side.

The aerodynamic model for electromagnetic transient, electromechanical transient, and steady-state conditions are the same because (3.1)-(3.5) are algebraic equations, and therefore have no dynamics.

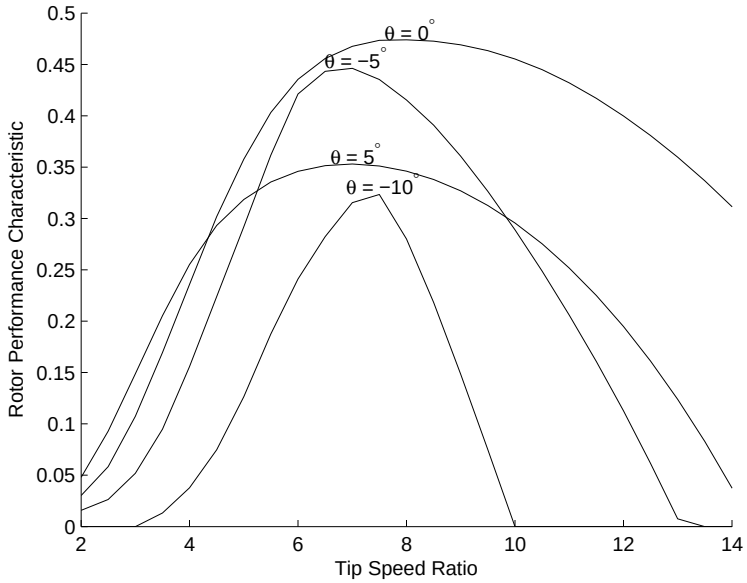

Figure 3.5: Rotor performance characteristic curve

3.1.2 Mechanical System

The mechanical components of a wind turbine consist of blade inertia, generator inertia, a gearbox, and shafts as shown in Fig. 3.6. The gearbox is assumed to be a parallel gear. The blade inertia and the blade shaft can be brought to the generator reference frame. Then, the rotor and generator shafts are combined (Fig. 3.7). As this model contains two inertia, it is referred a two-mass model. The two-mass model consists of three models associated with each time scales, i.e., electromagnetic transient, electromechanical transient, and steady-state models.

3.1.2.1 Electromagnetic Transient Model

For electromagnetic transient simulation, the simulation time is very short, so the rotating mass maintains essentially the same speed. As a result, the speed of the blades (ω_{blade}) and the generator (ω_{gen}) can be assumed to be constant.

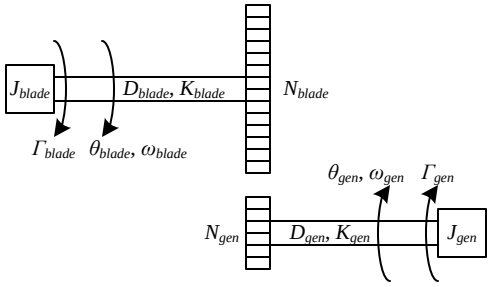

Figure 3.6: Wind turbine drivetrain

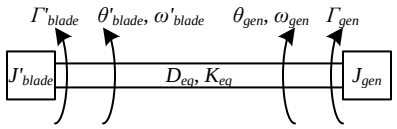

Figure 3.7: Two-mass model

3.1.2.2 Electromechanical Transient Model

Applying Newton's second law for rotation, the torque equations referring to the generator side are given as follows:

$$J'_{blade}\frac{d\omega'_{blade}}{dt} = \Gamma'_{aero} - D_{eq}\left(\omega'_{blade} - \omega_{gen}\right) - K_{eq}\left(\theta'_{blade} - \theta_{gen}\right) \tag{3.6}$$

$$J_{gen}\frac{d\omega_{gen}}{dt} = \Gamma_{gen} - D_{eq}\left(\omega_{gen} - \omega'_{blade}\right) - K_{eq}\left(\theta_{gen} - \theta'_{blade}\right) \tag{3.7}$$

where Γ_{gen} is the generator torque referred to the generator side, ω_{gen} is the rotational speed of the generator referred to the generator side, J'_{blade} and J_{gen} are the inertia of the blades and generator referred to the generator side, and D_{eq} and K_{eq} are the equivalent damping constant and stiffness of the shafts referred to the generator side. D_{eq} and K_{eq} are calculated by

$$D_{eq} = \frac{D'_{blade}D_{gen}}{D'_{blade} + D_{gen}} \tag{3.8}$$

$$K_{eq} = \frac{K'_{blade}K_{gen}}{K'_{blade} + K_{gen}} \tag{3.9}$$

where D'_{blade} and D_{gen} are the damping constant of the blade and generator shafts referred to the generator side, and K'_{blade} and K_{gen} are the stiffness of the blade and generator shafts referred to the generator side.

3.1.2.3 Steady-State Model

In a steady-state condition, the derivatives of ω_{blade} and ω_{gen} in (3.6)-(3.7) are set to zero. Hence, the aerodynamic and generator torques referred to the generator side are equal with an opposite direction, i.e.,

$$\Gamma'_{aero} = -\Gamma_{gen} \tag{3.10}$$

3.1.3 Generator

As discussed earlier in this chapter, an FSWT employs a SCIG. Note that the rotor of the SCIG is shorted. A WSWT and a DFIG wind turbine employ a WRIG. For a WSWT, a variable external rotor resistor is connected to the rotor of the WRIG. For a DFIG wind turbine, the rotor of the WRIG is connected to the grid through a back-to-back converter. A full converter wind turbine can employ either a synchronous generator or an induction generator. In this research, a permanent magnet synchronous generator (PMSG) is used.

3.1.3.1 Induction Generator

An induction generator model can be classified into three types: electromagnetic transient, electromechanical transient, and steady-state models.

Electromagnetic Transient Model: The electromagnetic transient model is a complete model considering both stator and rotor transients. The equivalent circuits

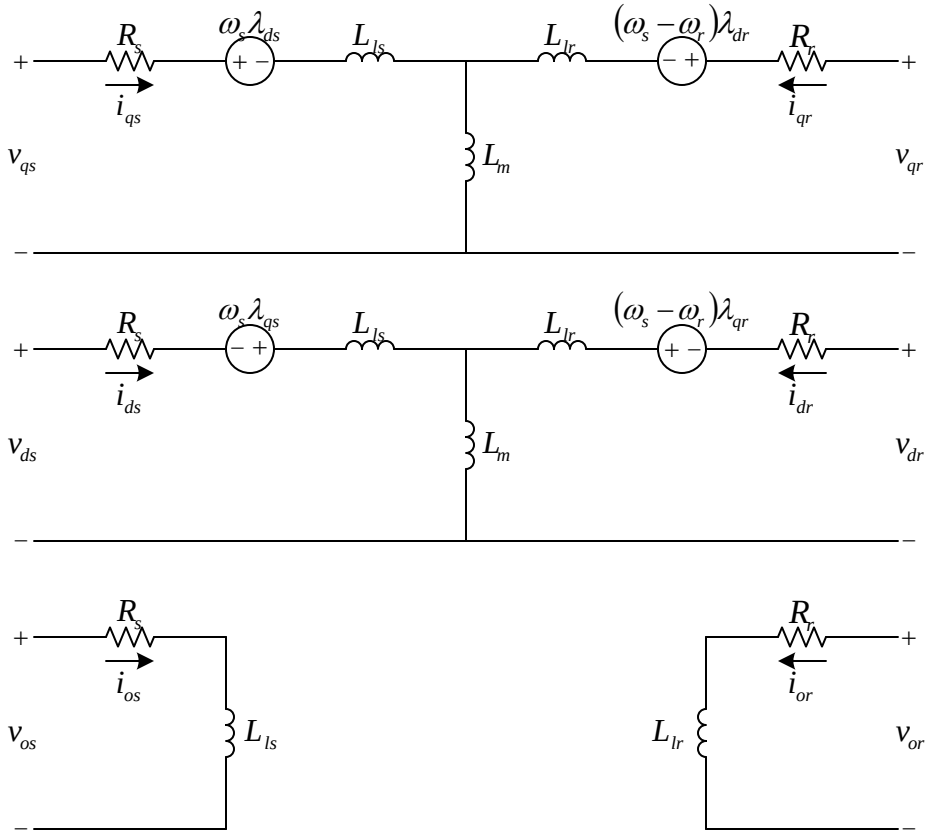

Figure 3.8: Electromagnetic transient model of an induction generator

in a qdo synchronous reference frame are shown in Fig. 3.8. The model equations are as follows: [61, 62, 66, 70]

The voltage equations referring to the stator side in a qdo synchronous reference frame are given by

$$v_{qs} = R_s i_{qs} + \frac{d}{dt}\lambda_{qs} + \omega_s \lambda_{ds} \tag{3.11}$$

$$v_{ds} = R_s i_{ds} + \frac{d}{dt}\lambda_{ds} - \omega_s \lambda_{qs} \tag{3.12}$$

$$v_{os} = R_s i_{os} + \frac{d}{dt}\lambda_{os} \tag{3.13}$$

$$v_{qr} = R_r i_{qr} + \frac{d}{dt}\lambda_{qr} + (\omega_s - \omega_r)\,\lambda_{dr} \tag{3.14}$$

$$v_{dr} = R_r i_{dr} + \frac{d}{dt}\lambda_{dr} - (\omega_s - \omega_r)\,\lambda_{qr} \tag{3.15}$$

$$v_{or} = R_r i_{or} + \frac{d}{dt}\lambda_{or} \tag{3.16}$$

where v_{qs}, v_{ds}, and v_{os} are the stator voltages in q-, d-, and o-axes; v_{qr}, v_{dr}, and v_{or} are the rotor voltages in q-, d-, and o-axes; i_{qs}, i_{ds}, and i_{os} are the stator currents in q-, d-, and o-axes; i_{qr}, i_{dr}, and i_{or} are the rotor currents in q-, d-, and o-axes; λ_{qs}, λ_{ds}, and λ_{os} are the stator flux linkages in q-, d-, and o-axes; λ_{qr}, λ_{dr}, and λ_{or} are the rotor flux linkages in q-, d-, and o-axes; R_s and R_r are the stator and rotor resistances; and ω_s is the synchronous speed.

The flux linkage equations referring to the stator side in a qdo synchronous reference frame are given by

$$\lambda_{qs} = (L_{ls} + L_m)\, i_{qs} + L_m i_{qr} \tag{3.17}$$

$$\lambda_{ds} = (L_{ls} + L_m)\, i_{ds} + L_m i_{dr} \tag{3.18}$$

$$\lambda_{os} = L_{ls} i_{os} \tag{3.19}$$

$$\lambda_{qr} = (L_{lr} + L_m)\, i_{qr} + L_m i_{qs} \tag{3.20}$$

$$\lambda_{dr} = (L_{lr} + L_m)\, i_{dr} + L_m i_{ds} \tag{3.21}$$

$$\lambda_{or} = L_{lr} i_{or} \tag{3.22}$$

where L_m is the mutual or magnetizing inductance, and L_{ls} and L_{lr} are the stator and rotor leakage inductances.

The torque equation referring to the stator side in a qdo synchronous reference frame is given as

$$\Gamma_{gen} = \frac{3}{2} P L_m \left(i_{qs} i_{dr} - i_{ds} i_{qr}\right) \tag{3.23}$$

where P is the number of pole pairs.

Electromechanical Transient Model: The electromechanical transient model is a reduced model obtained by neglecting stator transients. This model is suitable for power system stability studies [70]. The model consists of positive-, negative-, and zero-sequence circuits. The model equations are as follows: [61, 62, 70]

The positive-sequence voltage and flux linkage equations referring to the stator side in a qdo synchronous reference frame are given by

$$\frac{d}{dt}E'_{q1} = -\frac{1}{T'_{ro}}\left[E'_{q1} - (X_s - X'_s)\, i_{ds1}\right] - (\omega_s - \omega_r)\, E'_{d1} \tag{3.24}$$

$$\frac{d}{dt}E'_{d1} = -\frac{1}{T'_{ro}}\left[E'_{d1} + (X_s - X'_s)\, i_{qs1}\right] + (\omega_s - \omega_r)\, E'_{q1} \tag{3.25}$$

$$v_{qs1} = R_s i_{qs1} + X'_s i_{ds1} + E'_{q1} \tag{3.26}$$

$$v_{ds1} = R_s i_{ds1} - X'_s i_{qs1} + E'_{d1} \tag{3.27}$$

where i_{qs1} and i_{ds1} are the positive-sequence stator currents in q- and d-axes, and v_{qs1} and v_{ds1} are the positive-sequence stator voltages in q- and d-axes. E'_{q1}, E'_{d1}, X_s, X'_s, and T'_{ro} are defined as follows:

$$E'_{q1} = \frac{\omega_s L_m}{L_{lr} + L_m}\lambda_{dr1} \tag{3.28}$$

$$E'_{d1} = -\frac{\omega_s L_m}{L_{lr} + L_m}\lambda_{qr1} \tag{3.29}$$

$$X_s = \omega_s\left(L_{ls} + L_m\right) \tag{3.30}$$

$$X'_s = \omega_s\left(L_{ls} + \frac{L_{lr}L_m}{L_{lr} + L_m}\right) \tag{3.31}$$

$$T'_{ro} = \frac{L_{lr} + L_m}{R_r} \tag{3.32}$$

where λ_{qr1} and λ_{dr1} are the positive-sequence rotor flux linkages in q- and d-axes.

The positive-sequence voltage and flux linkage equations in (3.24)-(3.27) can be written in a phasor form as follows:

$$\frac{d}{dt}E'_1 = -\frac{1}{T'_{ro}}\left[E'_1 - j\,(X_s - X'_s)\, i_{s1}\right] - j\,(\omega_s - \omega_r)\, E'_1 \tag{3.33}$$

$$v_{s1} = (R_s + jX'_s)\, i_{s1} + E'_1 \tag{3.34}$$

where i_{s1}, v_{s1}, and E'_1 are defined as follows:

$$i_{s1} = i_{qs1} - j i_{ds1} \tag{3.35}$$

$$v_{s1} = v_{qs1} - j v_{ds1} \tag{3.36}$$

$$E'_1 = E'_{q1} - j E'_{d1} \tag{3.37}$$

The negative-sequence voltage and flux linkage equations referring to the stator side in a qdo synchronous reference frame are given by

$$\frac{d}{dt}E'_{q2} = -\frac{1}{T'_{ro}}\left[E'_{q2} + (X_s - X'_s)\, i_{ds2}\right] - (-\omega_s - \omega_r)\, E'_{d2} \tag{3.38}$$

$$\frac{d}{dt}E'_{d2} = -\frac{1}{T'_{ro}}\left[E'_{d2} - (X_s - X'_s)\, i_{qs2}\right] + (-\omega_s - \omega_r)\, E'_{q2} \tag{3.39}$$

$$v_{qs2} = R_s i_{qs2} - X'_s i_{ds2} + E'_{q2} \tag{3.40}$$

$$v_{ds2} = R_s i_{ds2} + X'_s i_{qs2} + E'_{d2} \tag{3.41}$$

where i_{qs2} and i_{ds2} are the negative-sequence stator currents in q- and d-axes, and v_{qs2} and v_{ds2} are the negative-sequence stator voltages in q- and d-axes. E'_{q2} and E'_{d2} are defined as follows:

$$E'_{q2} = -\frac{\omega_s L_m}{L_{lr} + L_m}\lambda_{dr2} \tag{3.42}$$

$$E'_{d2} = \frac{\omega_s L_m}{L_{lr} + L_m}\lambda_{qr2} \tag{3.43}$$

where λ_{qr2} and λ_{dr2} are the negative-sequence rotor flux linkages in q- and d-axes. X_s, X'_s, and T'_{ro} are defined in (3.30)-(3.32)

The negative-sequence voltage and flux linkage equations in (3.38)-(3.41) can be written in a phasor form as follows:

$$\frac{d}{dt}E'_2 = -\frac{1}{T'_{ro}}\left[E'_2 - j\,(X_s - X'_s)\, i_{s2}\right] + j\,(-\omega_s - \omega_r)\, E'_2 \tag{3.44}$$

$$v_{s2} = (R_s + jX'_s)\, i_{s2} + E'_2 \tag{3.45}$$

where i_{s2}, v_{s2}, and E'_2 are defined as follows:

$$i_{s2} = i_{qs2} + ji_{ds2} \tag{3.46}$$

$$v_{s2} = v_{qs2} + jv_{ds2} \tag{3.47}$$

$$E'_2 = E'_{q2} + jE'_{d2} \tag{3.48}$$

The zero-sequence voltage and flux linkage equations referring to the stator side in a qdo synchronous reference frame are given by

$$\frac{d}{dt}\lambda_{r0} = -\frac{R_r}{L_{lr}}\lambda_{r0} \tag{3.49}$$

$$v_{s0} = (R_s + jX_{ls})\, i_{s0} \tag{3.50}$$

where λ_{r0} is the zero-sequence rotor flux linkage, i_{s0} is the zero-sequence stator current, and v_{s0} is the zero-sequence stator voltage. X_{ls} is defined by

$$X_{ls} = \omega_s L_{ls} \tag{3.51}$$

The sequence equivalent circuits of the stator of an induction generator shown in Fig. 3.9 are obtained from the stator equations in (3.34), (3.45), and (3.50).

The torque equation referring to the stator side in qdo synchronous reference frame is given as

$$\begin{aligned}\Gamma_{gen} = \frac{3}{2}\frac{P}{\omega_s}\Big[&\left(E'_{q1}i_{qs1} + E'_{d1}i_{ds1} - E'_{q2}i_{qs2} - E'_{d2}i_{ds2}\right) \\ &+ \left(E'_{q1}i_{qs2} - E'_{d1}i_{ds2} - E'_{q2}i_{qs1} + E'_{d2}i_{ds1}\right)\cos\left(2\omega_s t\right) \\ &+ \left(E'_{q1}i_{ds2} + E'_{d1}i_{qs2} - E'_{q2}i_{ds1} - E'_{d2}i_{qs1}\right)\sin\left(2\omega_s t\right)\Big]\end{aligned} \tag{3.52}$$

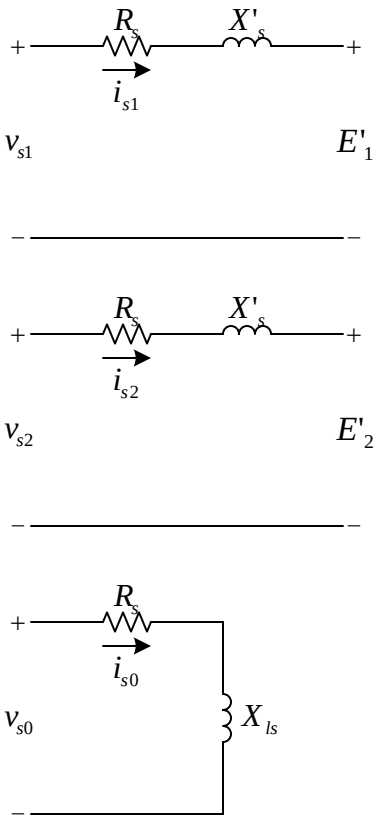

Figure 3.9: Electromechanical transient model of the stator of an induction generator

Steady-State Model: The steady-state model is obtained by neglecting all dynamics, i.e., setting all derivative terms to be zero. The model consists of positive-, negative-, and zero-sequence circuits. The sequence equivalent circuits are shown in Fig. 3.10. The model equations are as follows:

The positive-sequence equations referring to the stator side are

$$V_{s1} = (R_s + jX_{ls})\, I_{s1} + jX_m\, (I_{s1} + I_{r1}) \tag{3.53}$$

$$V_{r1} = \left(\frac{R_r}{s_1} + jX_{lr}\right) I_{r1} + jX_m\, (I_{r1} + I_{s1}) \tag{3.54}$$

The negative-sequence equations referring to the stator side are

$$V_{s2} = (R_s + jX_{ls})\, I_{s2} + jX_m\, (I_{s2} + I_{r2}) \tag{3.55}$$

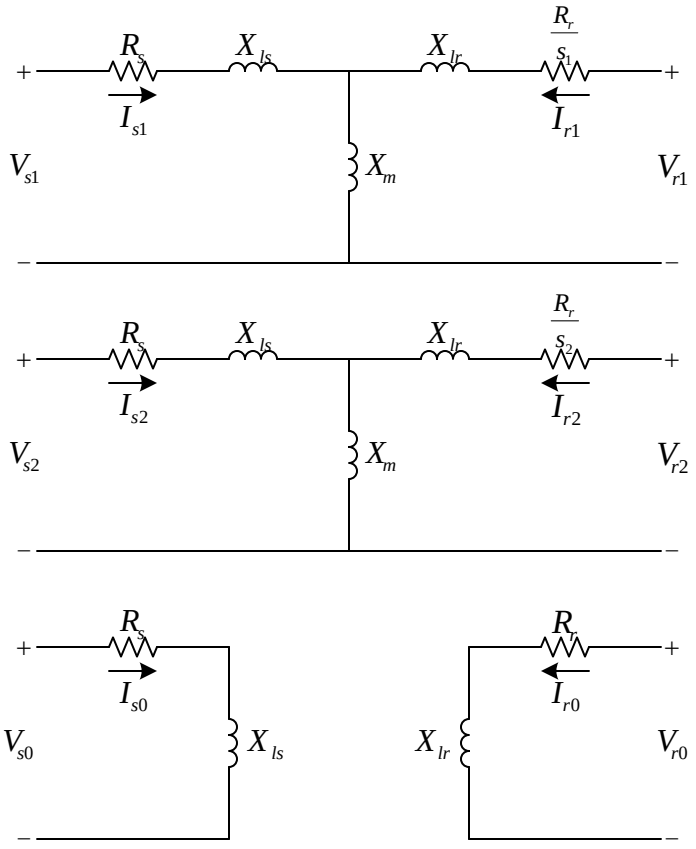

Figure 3.10: Steady-state model of an induction generator

$$V_{r2} = \left(\frac{R_r}{s_2} + jX_{lr}\right) I_{r2} + jX_m \left(I_{r2} + I_{s2}\right) \tag{3.56}$$

The zero-sequence equations referring to the stator side are

$$V_{s0} = \left(R_s + jX_{ls}\right) I_{s0} \tag{3.57}$$

$$V_{r0} = \left(R_r + jX_{lr}\right) I_{r0} \tag{3.58}$$

X_{ls}, X_{lr}, X_m, s_1 and s_2 are defined as

$$X_{ls} = \omega_s L_{ls} \tag{3.59}$$

$$X_{lr} = \omega_s L_{lr} \tag{3.60}$$

$$X_m = \omega_s L_m \tag{3.61}$$

$$s_1 = \frac{\omega_s - \omega_r}{\omega_s} \tag{3.62}$$

$$s_2 = \frac{-\omega_s - \omega_r}{-\omega_s} \tag{3.63}$$

The torque equation referring to the stator side is given as

$$\Gamma_{gen} = 3\frac{PX_m}{\omega_s}\Re\left[j\left(I_{s1}^* I_{r1} - I_{s2}^* I_{r2}\right)\right] \tag{3.64}$$

3.1.3.2 Permanent Magnet Synchronous Generator

A PMSG model can be classified into three types: electromagnetic transient, electromechanical transient, and steady-state models.

Electromagnetic Transient Model: The equivalent circuits of a PMSG in a qdo rotor reference frame are shown in Fig. 3.11. The permanent magnet is represented by a constant current source (I_f). The model equations which neglect the dynamics of damper windings are as follows: [61, 62, 66, 70]

The voltage equations referring to the stator side in a qdo rotor reference frame are given as follows:

$$v_{qs} = R_s i_{qs} + \frac{d}{dt}\lambda_{qs} + \omega_r \lambda_{ds} \tag{3.65}$$

$$v_{ds} = R_s i_{ds} + \frac{d}{dt}\lambda_{ds} - \omega_r \lambda_{qs} \tag{3.66}$$

$$v_{os} = R_s i_{os} + \frac{d}{dt}\lambda_{os} \tag{3.67}$$

where v_{qs}, v_{ds}, and v_{os} are the stator voltages in q-, d-, and o-axes; i_{qs}, i_{ds}, and i_{os} are the stator currents in q-, d-, and o-axes; λ_{qs}, λ_{ds}, and λ_{os} are the stator flux linkages in q-, d-, and o-axes; and R_s is the stator resistance.

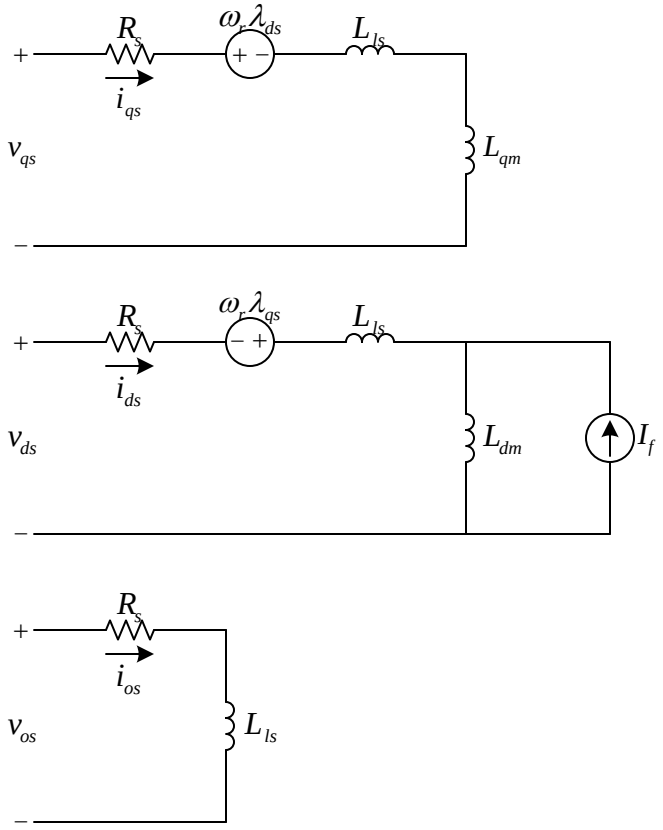

Figure 3.11: Electromagnetic transient model of a PMSG

The flux linkage equations referring to the stator side in a qdo rotor reference frame are given as follows:

$$\lambda_{qs} = (L_{ls} + L_{qm})\, i_{qs} \tag{3.68}$$

$$\lambda_{ds} = (L_{ls} + L_{dm})\, i_{ds} + \lambda_r \tag{3.69}$$

$$\lambda_{os} = L_{ls} i_{os} \tag{3.70}$$

where L_{qm} and L_{dm} are the mutual or magnetizing inductance in q- and d-axes, L_{ls} is the stator leakage inductance, and λ_r is the rotor flux linkage which is defined by

$$\lambda_r = L_{dm} I_f \tag{3.71}$$

The torque equation referring to the stator side in a qdo synchronous reference frame are given as follows:

$$\Gamma_{gen} = \frac{3}{2} P \left[\lambda_r i_{qs} + \left(L_{dm} - L_{qm} \right) i_{ds} i_{qs} \right] \tag{3.72}$$

where P is the number of pole pairs.

Electromechanical Transient Model: The electromechanical transient model of a PMSG is the same as the electromagnetic transient model because the electromagnetic transient model equations do not include the dynamics of damper windings that affect a power system in an electromagnetic transient condition.

Steady-State Model: The equivalent circuits of a PMSG in a qdo rotor reference frame are shown in Fig. 3.12. The model equations in a qdo rotor reference frame are as follows: [61, 62, 66]

$$v_{qs} = R_s i_{qs} + \omega_r \left(L_d i_{ds} + \lambda_r \right) \tag{3.73}$$

$$v_{ds} = R_s i_{ds} - \omega_r L_q i_{qs} \tag{3.74}$$

$$v_{os} = \left(R_s + j \omega_r L_{ls} \right) i_{os} \tag{3.75}$$

where L_q and L_d are defined as follows:

$$L_q = L_{ls} + L_{qm} \tag{3.76}$$

$$L_d = L_{ls} + L_{dm} \tag{3.77}$$

The torque equation are the same as the torque for the electromagnetic transient model described in (3.72).

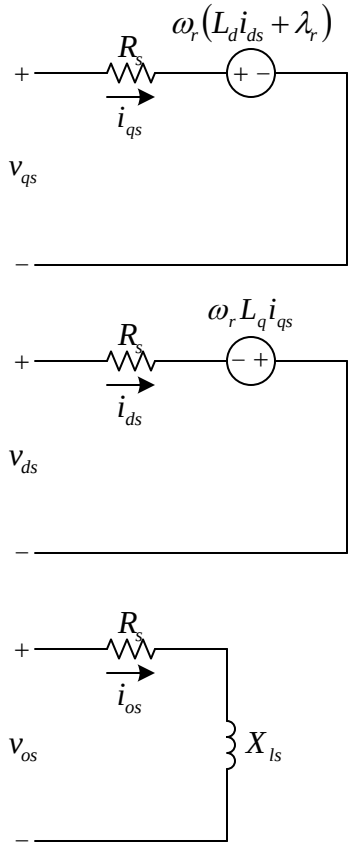

Figure 3.12: Steady-state model of a PMSG

3.1.4 Converter

A converter is employed by DFIG and full converter wind turbines. For a DFIG wind turbine, a converter connects the rotor of the WRIG to the grid. For a full converter wind turbine, a converter connects the stator of the generator to the grid. The converter employed by both types of wind turbines enables decoupling of real and reactive power control. The real power control is used to obtain the maximum power output from the wind turbine. Fig. 3.13 shows the maximum power point tracking (MPPT) curve. For each wind speed, the real power output of the wind turbine is regulated to match the MPPT curve. The reactive power control is used to regulate

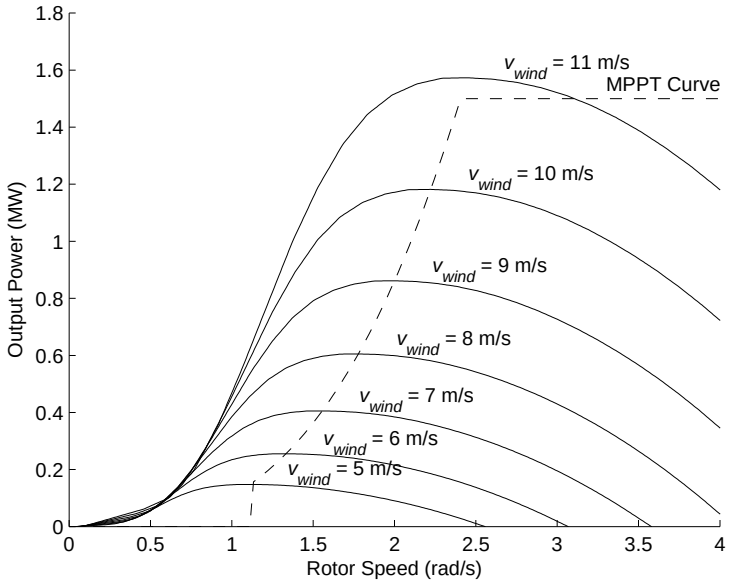

Figure 3.13: Maximum power point tracking curve

the reactive power output, power factor, or terminal voltage of the wind turbine. Note that the control approaches for wind turbines are presented in [37, 40, 66]. The converter is assumed to produce only positive-sequence current at the fundamental frequency, and the harmonic currents are neglected. The converter model consists of three models, i.e., electromagnetic transient, electromechanical transient, and steady-state models.

3.1.4.1 Electromagnetic Transient Model

For an electromagnetic transient simulation, the converters are represented by a current source model. The current of the current source model is controlled by the same approach as the converter control. Since the real and reactive power output of the wind turbines are independently controlled by the converter, the current of the current source model are separated into the components on q- and d-axes. The q-axis

current component is used to control the real power output of the wind turbine, while the d-axis current component is used to control the reactive power output of the wind turbine. Each current component is controlled by a PI controller similar to the PI controller employed by the converter control.

3.1.4.2 Electromechanical Transient Model

Because the time scale of the converter control is close to the border between the electromechanical and electromagnetic transient phenomena, the converter model for electromechanical transient simulation is identical to the model for electromagnetic transient simulation, i.e., the converter is represented by a current source model with two PI controllers for real and reactive power controls.

3.1.4.3 Steady-State Model

Since DFIG and full converter wind turbines employs a converter to control the real and reactive power output, the converters can be represented by a constant power load in a steady-state condition. The real power of the constant power load model is obtained from the real power control set point (MPPT curve), while the reactive power of the constant power load model is obtained from the reactive power control set point. Note that the power in the constant power load model is negative because the wind turbines generates power.

3.2 Models of PVs

PV systems consist of PV arrays and inverters [71] as shown in Fig. 3.14. Since PV is a DC source connected to an AC grid, inverters are employed to connect PV arrays to the grid. The main advantage of the inverter is that it has an ability

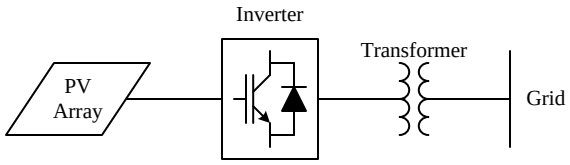

Figure 3.14: Block diagram of a PV

to perform an MPPT control. Because the power output of the PV varies with the terminal voltage, the inverter is employed to perform the MPPT so that the PV always generates the highest amount of power. However, if the voltages in the circuit are too high, volt/watt control may be implemented to curtail the power output of the PV [72]. In addition to the real power controls, the inverter also enables reactive power controls. Hence, additional PV reactive power controls such as fixed power factor, variable power factor, volt/var, and dynamic reactive current controls can also be implemented [72–75].

A PV model consists of two major components, i.e., PV array and inverter. Each component consists of its electromagnetic transient, electromechanical transient, and steady-state models as described in the following sections.

3.2.1 PV Array

The PV array consists of PV cells which convert solar energy to electricity. In order to increase the output voltage, PV cells are connected in series. In addition, PV cells are connected in parallel to increase the output current.

The equivalent circuit of a PV cell is shown in Fig. 3.15 [65, 68, 76, 77]. Since the series resistance (R_s), shunt resistance (R_p), and shunt capacitance (C_p) are very small, they are neglected. Thus, the equivalent circuit of an ideal PV cell consists of a current source and a diode. Note that the Shockley ideal diode equation is given

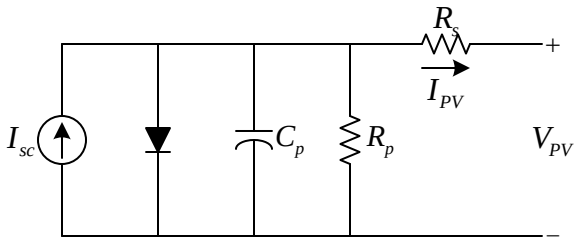

Figure 3.15: Equivalent circuit of a PV cell

by

$$I_d = I_0 \left(e^{\frac{qV_d}{kT}} - 1 \right) \tag{3.78}$$

where I_d is the diode current, V_d is the diode voltage, I_0 is the reverse bias saturation current, q is the electron charge, k is the Boltzmann's constant, and T is the absolute temperature. The output current of a PV cell is obtained as [65, 68, 69]

$$I_{PV} = I_{sc} - I_d = I_{sc} - I_0 \left(e^{\frac{qV_{PV}}{kT}} - 1 \right) \tag{3.79}$$

where I_{PV} is the output current of a PV cell, I_{sc} is the short-circuit current of a PV cell, and V_{PV} is the output voltage of a PV cell. Fig. 3.16 shows the characteristic of a PV cell with the reverse saturation current (I_0) of 10^{-10} A and at 25°C. For each PV curve in Fig. 3.16, there is a maximum power point as shown in Fig. 3.17. The maximum power output of PV is almost proportional to the short-circuit current of the PV as presented in Fig. 3.18. Note that the short-circuit current of the PV is proportional to the solar irradiance.

Because (3.79) has no dynamics, the electromagnetic transient, electromechanical transient, and steady-state models of PV arrays are identical. Note that the shunt capacitance (C_p) is neglected.

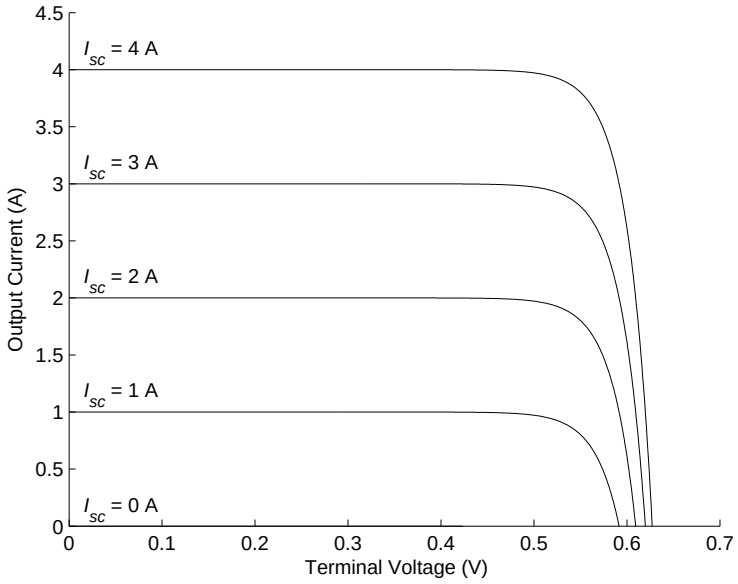

Figure 3.16: Characteristic of a PV cell

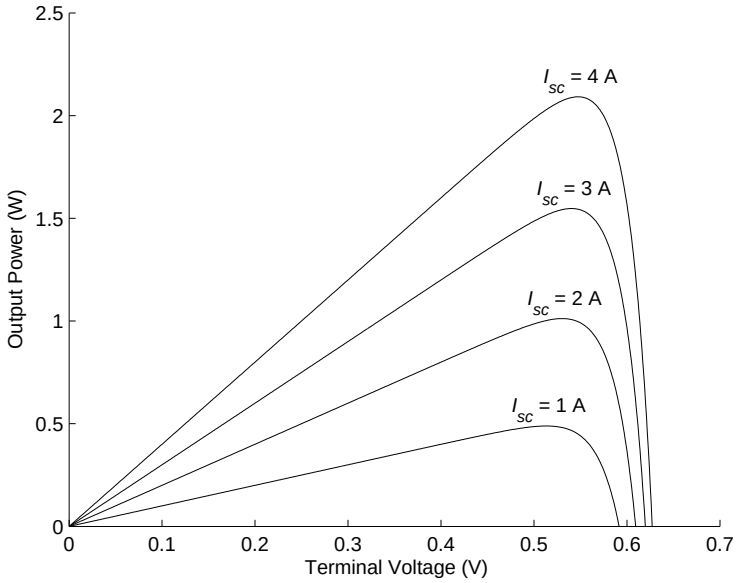

Figure 3.17: Power output of a PV cell

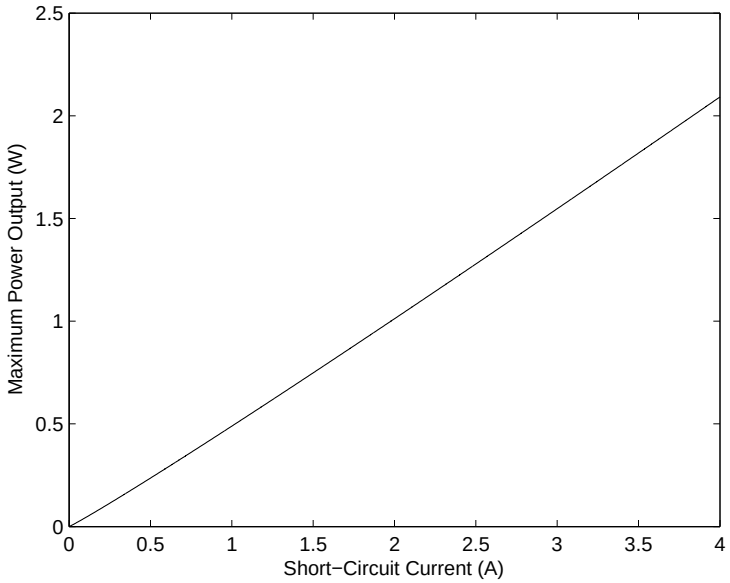

Figure 3.18: Maximum power output of a PV cell

3.2.2 Inverter

Since PV is a DC source, but the grid is an AC circuit, PVs employ inverters to connect their PV arrays to the grid. The inverter is also used to control the real and reactive power output of the PV independently. The inverter model consists of three models for three time scales, i.e., electromagnetic transient, electromechanical transient, and steady-state models. The PV inverter models are similar to the models of wind turbine converters.

Chapter 4

Multi-Time-Scale Approach for Distribution Circuit Simulation

This chapter describes the multi-time-scale simulation approach for distribution circuits with wind turbines and PVs. The following sections present the development of the steady-state, electromechanical transient, and electromagnetic transient models for each type of wind turbine and PV, followed by the integration of single-time-scale models into the multi-time-scale simulation, i.e., the approaches to determine which single-time-scale model to use in the multi-time-scale simulation, when to use each single-time-scale model, and when to switch to another single-time-scale model.

4.1 Single-Time-Scale Simulation Models

This section describes the approaches to develop the single-time-scale simulation models of distribution circuits with wind turbines and PVs. The steady-state, electromechanical transient, and electromagnetic transient models of each circuit equipment are developed based on the equations described earlier in Chapters 2 and 3. The circuit equipment that have fixed impedances or admittances (feeders, transformers, capacitor banks, and constant impedance loads) are connected to each other and form a distribution network represented by a nodal admittance matrix. The circuit equipment that contain voltage or current sources or have variable impedances or admittances (constant power loads, wind turbines, and PVs) are represented by

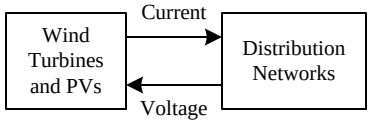

Figure 4.1: Interface of distribution network, wind turbine, and PV models

voltage or current sources connected to the distribution network as shown in Fig. 4.1. The following sections describe the approaches to connect the wind turbine and PV models to the distribution network models for quasi-steady-state, electromechanical transient, and electromagnetic transient simulations.

4.1.1 Steady-State Model

This section describes steady-state models for each type of wind turbine and PVs. The wind turbine and PV models obtain the terminal voltages from the distribution network model and feed the generator currents back to the network model as shown in Fig. 4.2. The network solution is obtained by using fixed-point iteration as follows: First, Phase A, B, and C voltages at the terminal of the wind turbines and PVs are estimated to be the voltage results obtained from previous simulation. If the previous simulation results are not available, the voltages for Phases A, B, and C are assumed to be $1\angle 0°$, $1\angle -120°$, and $1\angle 120°$ pu, respectively. Then, the wind turbine currents are calculated from the wind turbine model, and the PV currents are calculated from the PV model. After that, the wind turbine and PV voltages are calculated from the network equation (nodal admittance matrix). The calculations are repeated until the wind turbine and PV voltages and currents converge. Finally, the remaining voltages and currents at the other nodes are calculated using the nodal admittance matrix.

The approaches to calculate the wind turbine and PV currents from each type

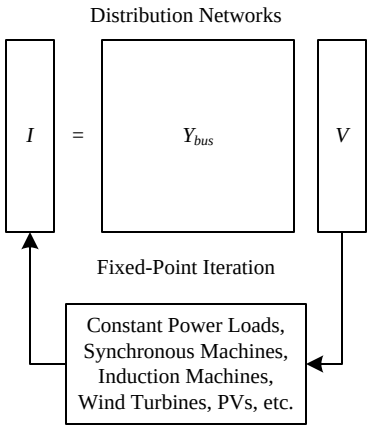

Figure 4.2: Interface of distribution network, wind turbine, and PV models for a steady-state simulation

of wind turbine and PV models are described as follows:

4.1.1.1 FSWT Model

An FSWT consists of a SCIG directly connected to the distribution circuit. The block diagram presenting the calculation process for the steady-state model of an FSWT is shown in Fig. 4.3. As can be seen from the figure, the inputs of the steady-state model of an FSWT are wind speed (v_{wind}), pitch angle (θ), stator voltage (V_{s1}, V_{s2}, and V_{s0}), and initial slip ($s_{1,init}$ and $s_{2,init}$). The model calculates stator and rotor currents (I_{s1}, I_{s2}, I_{s0}, I_{r1}, I_{r2}, and I_{r0}) by using (3.53)-(3.58). Note that rotor voltage (V_{r1}, V_{r2}, and V_{r0}) is zero for a SCIG. The generator torque (Γ_{gen}) is calculated by using (3.64), and the aerodynamic torque (Γ_{aero}) is calculated by using (3.1)-(3.5). If the generator torque matches the aerodynamic torque, i.e., $|\Gamma'_{aero} - \Gamma_{gen}| \leq \Gamma_{error,max}$, the output stator current will be fed to the distribution network model. However, if the generator torque does not match the aerodynamic torque, i.e., $|\Gamma'_{aero} - \Gamma_{gen}| > \Gamma_{error,max}$, the FSWT model will approximate new slip by

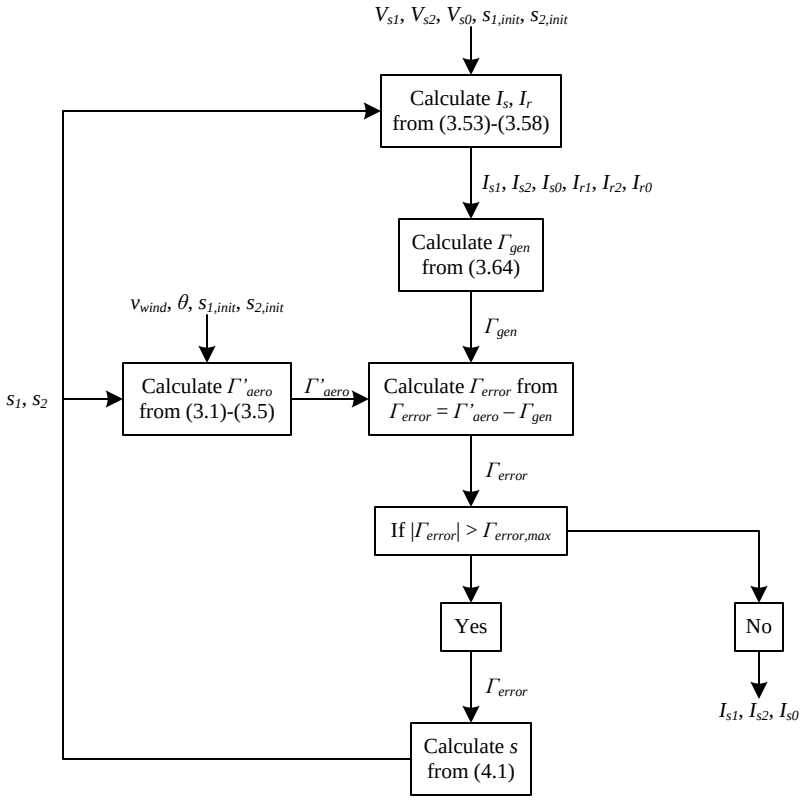

Figure 4.3: Block diagram for the steady-state model of an FSWT

$$s_{1,new} = s_{1,old} + k\left(\Gamma'_{aero} - \Gamma_{gen}\right) \tag{4.1}$$

where k is a constant (positive) chosen so that the results converge. Then, the FSWT model recalculates the currents and torques. The iteration process is repeated until the results converge.

4.1.1.2 WSWT Model

A WSWT consists of a WRIG with an external rotor resistor. The generator is directly connected to the distribution circuit. The block diagram presenting the calculation process for the steady-state model of a WSWT is shown in Fig. 4.4. As can be seen from the figure, the WSWT model is similar to the FSWT model.

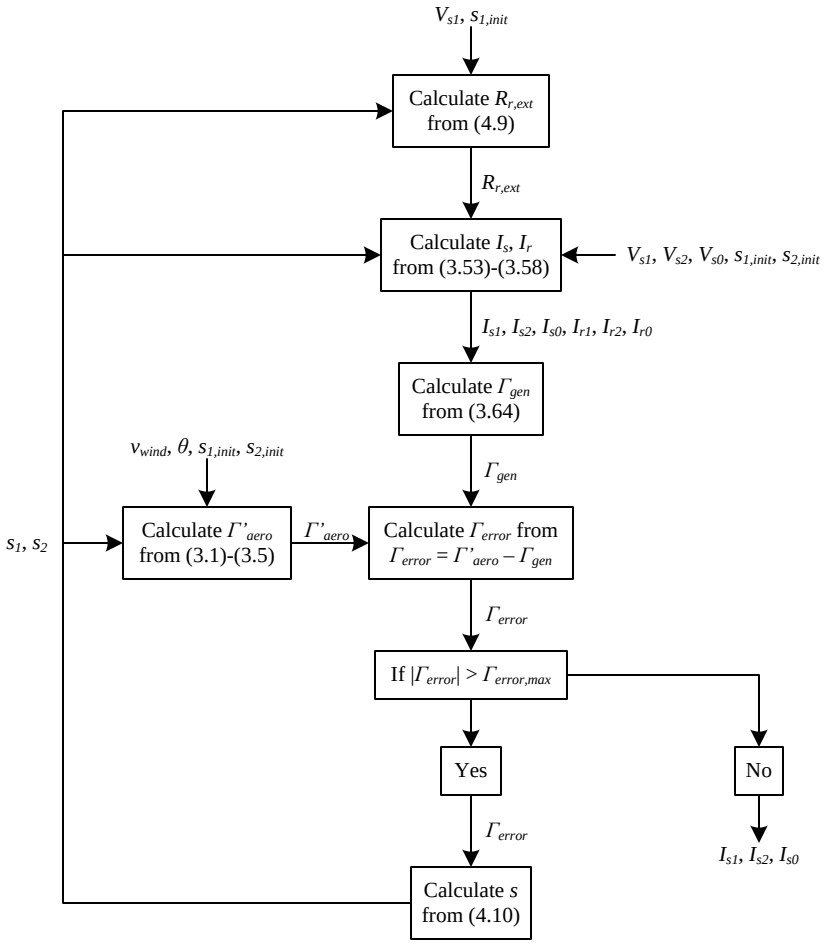

Figure 4.4: Block diagram for the steady-state model of a WSWT

However, the rotor resistance is the combination of the resistance of the rotor winding (R_r) and the external rotor resistance ($R_{r,ext}$). When wind speed is lower than the rated speed, the external rotor resistance is set to zero. However, when wind speed is higher than the rated speed, the external rotor resistance is set to obtain rated power (P_{rated}). The external rotor resistance is calculated as follows: From the equivalent circuit of a WRIG in Fig. 4.5, the positive-sequence real power produced by the WSWT is given by

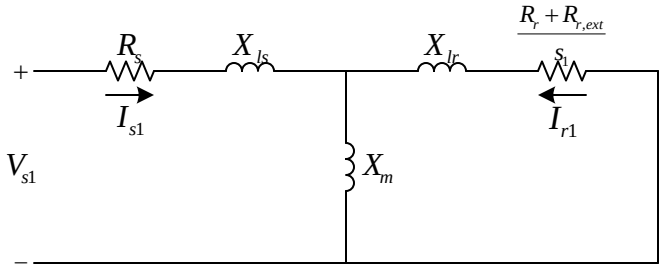

Figure 4.5: Positive-sequence steady-state model of a WRIG

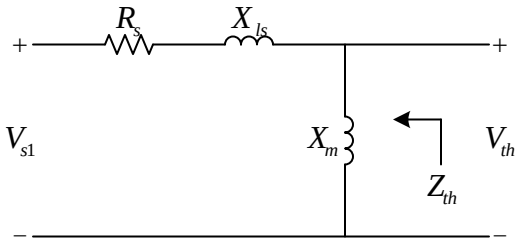

Figure 4.6: Positive-sequence Thevenin equivalent circuit of a WRIG stator

$$P_{s1} = 3\left|I_{r1}\right|^2 \frac{R_r + R_{r,ext}}{s_1} + 3\left|I_{s1}\right|^2 R_s \tag{4.2}$$

where P_{s1} is the positive-sequence real power at the stator. The external rotor resistance is set so that the real power produced by the WSWT is equal to the rated power. Thus,

$$P_{rated} = P_{s1} = 3\left|I_{r1}\right|^2 \frac{R_r + R_{r,ext}}{s_1} + 3\left|I_{s1}\right|^2 R_s \tag{4.3}$$

Note that the negative-sequence real power is much smaller than the positive-sequence real power. Hence, the negative-sequence real power is neglected in (4.3). The equivalent circuit of a WRIG in Fig. 4.5 can be simplified by using a Thevenin equivalent circuit to represent the stator circuit as shown in Figs. 4.6 and 4.7. According to Fig. 4.7, the rotor current in (4.2) and (4.3) is calculated by

$$I_{r1} = -\frac{V_{th}}{R_{th} + jX_{th} + \frac{R_r + R_{r,ext}}{s_1} + jX_{lr}} \tag{4.4}$$

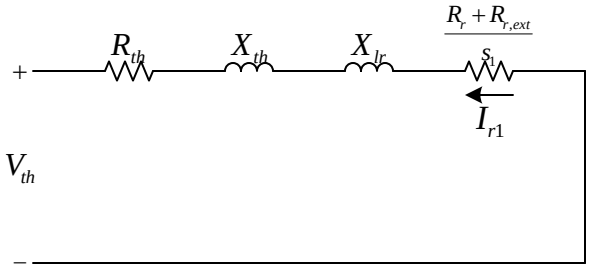

Figure 4.7: Simplified positive-sequence steady-state model of a WRIG

where the Thevenin voltage (V_{th}), resistance (R_{th}), and reactance (X_{th}) in (4.4) and (4.8) are calculated from Fig. 4.6 as follows:

$$V_{th} = \frac{jX_m V_{s1}}{R_s + jX_{ls} + jX_m} \tag{4.5}$$

$$R_{th} = \Re\left[\frac{(R_s + jX_{ls})\, jX_m}{R_s + jX_{ls} + jX_m}\right] \tag{4.6}$$

$$X_{th} = \Im\left[\frac{(R_s + jX_{ls})\, jX_m}{R_s + jX_{ls} + jX_m}\right] \tag{4.7}$$

The stator current in (4.2) and (4.3) is calculated from the equivalent circuit in Fig. 4.5 as follows:

$$I_{s1} = -\frac{jX_m}{\frac{R_r + R_{r,ext}}{s_1} + jX_{lr} + jX_m} I_{r1} \tag{4.8}$$

By solving (4.3), the external resistance when wind speed is higher than the rated speed is

$$\begin{aligned} R_{r,ext,new} = -s_1 \Bigg[& \left(\frac{3\,|V_{th}|^2}{2P_{rated}} + R_{th}\right)^2 - R_{th}^2 - (X_{th} + X_{lr})^2 \\ & + \frac{3R_s\left\{(X_m + X_{lr})^2 + \left(\frac{R_r + R_{r,ext,old}}{s_1}\right)^2\right\}|V_{th}|^2}{X_m^2 P_{rated}} \Bigg]^{\frac{1}{2}} \\ & - s_1\left(\frac{3\,|V_{th}|^2}{2P_{rated}} + R_{th}\right) - R_r \end{aligned} \tag{4.9}$$

The external rotor resistance is then used to calculate stator and rotor currents. If the generator torque matches the aerodynamic torque, i.e., $|\Gamma'_{aero} - \Gamma_{gen}| \leq \Gamma_{error,max}$, the output stator current will be fed to the distribution network model. However, if the generator torque does not match the aerodynamic torque, i.e., $|\Gamma'_{aero} - \Gamma_{gen}| > \Gamma_{error,max}$, the WSWT model will approximate new slip by

$$s_{1,new} = s_{1,old} - k\left(\Gamma'_{aero} - \Gamma_{gen}\right) \tag{4.10}$$

where k is a constant (positive) chosen so that the results converge. Notice the minus sign in front of the torque error. Then, the WSWT model recalculates the external resistance, currents, and torques. The iteration process is repeated until the results converge.

4.1.1.3 DFIG and Full Converter Wind Turbine Model

The DFIG wind turbine consists of a WRIG and a converter. The stator winding of the WRIG is directly connected to the distribution circuit, while the rotor winding is connected to the distribution circuit through a converter. The full converter wind turbine consists of a generator connected to the distribution circuit through a converter. The converter employed by both wind turbines enables decoupling of real and reactive power controls. Since both DFIG and full converter wind turbines employs a converter to control the real and reactive power output, both wind turbines can be represented by a constant power load in a steady-state condition. The block diagram presenting the calculation process for the steady-state model of DFIG and full converter wind turbines is shown in Fig. 4.8. As can be seen from the figure, the inputs of the model are real power reference (P_{ref}), reactive power reference (Q_{ref}), and terminal voltage of the wind turbine (V_1). The real power reference of the model is obtained from the maximum power tracking (real power control), while the reactive

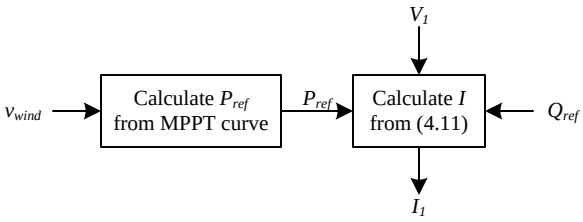

Figure 4.8: Block diagram for the steady-state model of DFIG and full converter wind turbines

power reference of the model is obtained from the reactive power control. Note that the real power reference in the constant power load model is negative because the wind turbines generates power. Because the converter produces only positive-sequence current, only positive-sequence voltages of the wind turbine are needed in the model. The constant power load model calculates the wind turbine currents from the real and reactive power references and terminal voltage as follows:

$$I_1 = -\frac{P_{ref} - jQ_{ref}}{3V_1^*} \tag{4.11}$$

where I_1 is the current flowing out of the wind turbine. Note that P_{ref} and Q_{ref} are negative when the wind turbine produces real and reactive power. The wind turbine output current obtained from the constant power load model will be fed to the distribution network model.

4.1.1.4 PV Model

PV consists of PV arrays connected to the distribution circuit via inverters. The inverters enables decoupling of real and reactive power controls. The real power output of the PV is controlled by the maximum power tracking approach (real power control), and the reactive power output of the PV is controlled by the reactive power control. The characteristic of PVs depends on the inverter real and reactive power

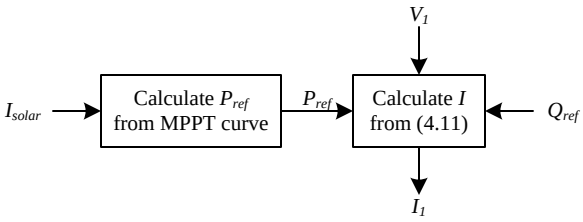

Figure 4.9: Block diagram for the steady-state model of a PV

controls, so PVs are modeled as a constant power load (Fig. 4.9) in a steady-state condition, similar to the steady-state model of DFIG and full converter wind turbines. The real and reactive power of the constant power load model is obtained from the set point of the controls. Note that the power in the constant power load model is negative because the PV generates power.

4.1.2 Electromechanical Transient Model

This section describes electromechanical transient models for each type of wind turbine and PV. The wind turbine and PV models consist of differential and algebraic equations. The differential equations are solved by the Runge-Kutta method (RK4), the linear algebraic equations are combined with the nodal admittance equation of the distribution network, and the nonlinear algebraic equations are solved by fixed-point iteration similar to the calculation approach for the steady-state simulation shown in Fig. 4.2. Note that the voltages and currents are recalculated every time step of the electromechanical transient simulation.

4.1.2.1 FSWT Model

The block diagram for the electromechanical transient model of an FSWT is shown in Fig. 4.10. The electromechanical transient model of an FSWT employs

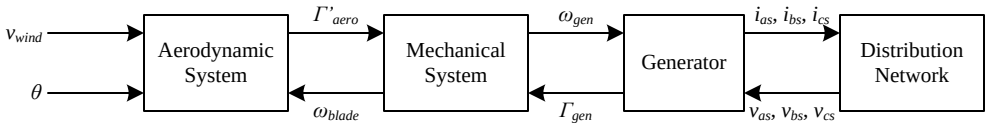

Figure 4.10: Block diagram for the electromechanical model of an FSWT

the reduced model of an induction generator described in (3.24)-(3.52). Because the stator transients of the induction generator are neglected, the stator equations in (3.34), (3.45), and (3.50) are algebraic equations and therefore can be included in the nodal admittance matrix of the distribution network. The positive-, negative-, and zero-sequence stator equations in (3.34), (3.45), and (3.50) can be written in a nodal admittance matrix form as follows:

$$\begin{bmatrix} i_{s0} \\ i_{s1} \\ i_{s2} \end{bmatrix} + \frac{1}{R_s + jX'_s} \begin{bmatrix} 0 \\ E'_1 \\ E'_2 \end{bmatrix} = \begin{bmatrix} \frac{1}{R_s+jX_{ls}} & 0 & 0 \\ 0 & \frac{1}{R_s+jX'_s} & 0 \\ 0 & 0 & \frac{1}{R_s+jX'_s} \end{bmatrix} \begin{bmatrix} v_{s0} \\ v_{s1} \\ v_{s2} \end{bmatrix} \tag{4.12}$$

Converting the positive-, negative-, and zero-sequence stator currents and voltages to Phase A, B, and C stator currents and voltages yields

$$\begin{bmatrix} i_{sa} \\ i_{sb} \\ i_{sc} \end{bmatrix} + \frac{1}{R_s + jX'_s} \begin{bmatrix} E'_1 + E'_2 \\ a^2E'_1 + aE'_2 \\ aE'_1 + a^2E'_2 \end{bmatrix}$$
$$= \begin{bmatrix} \frac{1}{R_s+jX_{ls}} + \frac{2}{R_s+jX'_s} & \frac{1}{R_s+jX_{ls}} - \frac{1}{R_s+jX'_s} & \frac{1}{R_s+jX_{ls}} - \frac{1}{R_s+jX'_s} \\ \frac{1}{R_s+jX_{ls}} - \frac{1}{R_s+jX'_s} & \frac{1}{R_s+jX_{ls}} + \frac{2}{R_s+jX'_s} & \frac{1}{R_s+jX_{ls}} - \frac{1}{R_s+jX'_s} \\ \frac{1}{R_s+jX_{ls}} - \frac{1}{R_s+jX'_s} & \frac{1}{R_s+jX_{ls}} - \frac{1}{R_s+jX'_s} & \frac{1}{R_s+jX_{ls}} + \frac{2}{R_s+jX'_s} \end{bmatrix} \begin{bmatrix} v_{sa} \\ v_{sb} \\ v_{sc} \end{bmatrix} \tag{4.13}$$

The stator equation in (4.13) will be added to the nodal admittance equation of the distribution network.

4.1.2.2 WSWT Model

The block diagram for the electromechanical transient model of a WSWT is shown in Fig. 4.11. Like an FSWT model, an electromechanical transient model of a

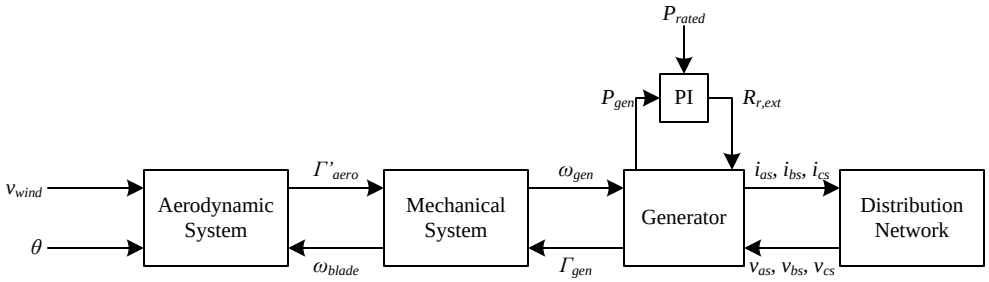

Figure 4.11: Block diagram for the electromechanical model of a WSWT

WSWT employs the reduced model of an induction generator. When wind speed is below the rated speed, external rotor resistance is set to zero. However, when wind speed is above the rated speed, the value of the external rotor resistance is calculated by using a PI controller as shown in Fig. 4.11. According to the figure, the difference between the rated power and the measured real power is fed to the PI controller. The PI controller then calculates the external rotor resistance as follows:

$$R_{r,ext} = R_{r,ext,p} + R_{r,ext,i} \tag{4.14}$$

$$R_{r,ext,p} = K_{p,r}\left(P_{rated} - P_{gen}\right) \tag{4.15}$$

$$\frac{d}{dt}R_{r,ext,i} = K_{i,r}\left(P_{rated} - P_{gen}\right) \tag{4.16}$$

where P_{rated} is the rated real power of the wind turbine, P_{gen} is the real power produced by the wind turbine, and $K_{p,r}$ and $K_{i,r}$ are the proportional and integral gains of the PI controller. The external rotor resistance is combined with the rotor resistance in the induction generator model.

4.1.2.3 DFIG and Full Converter Wind Turbine Model

In order to connect the generator of the DFIG and full converter wind turbines to the distribution network, a converter is employed. Since the converter is used to

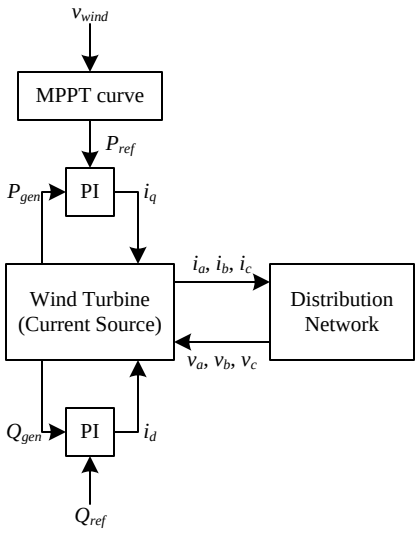

Figure 4.12: Block diagram for the electromechanical model of DFIG and full converter wind turbines

control the real and reactive power output of the wind turbine, the characteristic of the wind turbines depends on the control approaches used by the converter. As a result, for an electromechanical transient simulation, both wind turbines are represented by a current source model with the current controlled by the same approach as the converter controls. The block diagram for the electromechanical transient model of DFIG and full converter wind turbines is shown in Fig. 4.12. In order to control real and reactive power output of the wind turbines independently, the current of the current source model are separated into the components on q- and d-axes. Using the decoupled real and reactive power control approach, the real and reactive power of the wind turbines are obtained by

$$P_{gen} = \frac{3}{2} v_q i_q \tag{4.17}$$

$$Q_{gen} = \frac{3}{2} v_q i_d \tag{4.18}$$

where P_{gen} and Q_{gen} are the real and reactive power produced by the wind turbine, i_q and i_d are the wind turbine currents in q- and d-axes, and v_q is the wind turbine voltage in q-axis. Note that the wind turbine voltage in d-axis (v_d) is zero. From (4.17) and (4.18), the q-axis current component is used to control the real power output of the wind turbine, while the d-axis current component is used to control the reactive power output of the wind turbine. Each current component is controlled by a PI controller similar to the PI controller employed by the converter control. The equations for the control are as follows:

$$i_q = i_{q,p} + i_{q,i} \tag{4.19}$$

$$i_{q,p} = K_{p,p}\left(P_{ref} - P_{gen}\right) \tag{4.20}$$

$$\frac{d}{dt} i_{q,i} = K_{i,p}\left(P_{ref} - P_{gen}\right) \tag{4.21}$$

$$i_d = i_{d,p} + i_{d,i} \tag{4.22}$$

$$i_{d,p} = K_{p,q}\left(Q_{ref} - Q_{gen}\right) \tag{4.23}$$

$$\frac{d}{dt} i_{d,i} = K_{i,q}\left(Q_{ref} - Q_{gen}\right) \tag{4.24}$$

where P_{ref} and Q_{ref} are the reference real and reactive power of the wind turbine, $K_{p,p}$ and $K_{i,p}$ are the proportional and integral gains of the real power controller, and $K_{p,q}$ and $K_{i,q}$ are the proportional and integral gains of the reactive power controller.

4.1.2.4 PV Model

PV arrays are connected to the distribution circuit through inverters. The inverter is used to control the real and reactive power output of PVs, similar to the converter of DFIG and full converter wind turbines. Thus, the PV model for an electromechanical transient simulation is a current source model (Fig. 4.13) with the

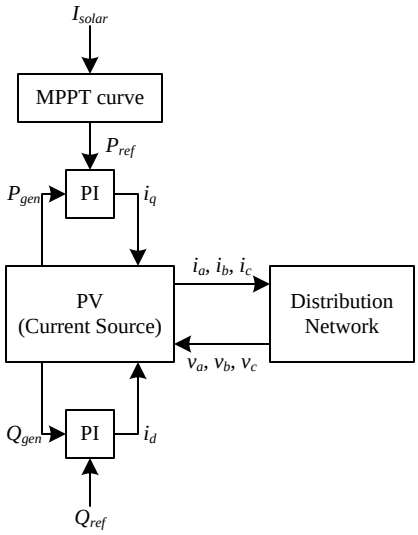

Figure 4.13: Block diagram for the electromechanical model of a PV

current controlled by the same approach as the converter control employed by DFIG and full converter wind turbines, i.e., the q-axis current is used to control the real power output of the PV, and the d-axis current is used to control the reactive power output of the PV. Note that the real and reactive power of three-phase PVs can be calculated by (4.17) and (4.18). However, the real and reactive power of single-phase PVs are given by

$$P_{gen} = \frac{1}{2} v_q i_q \tag{4.25}$$

$$Q_{gen} = \frac{1}{2} v_q i_d \tag{4.26}$$

4.1.3 Electromagnetic Transient Model

This section describes electromagnetic transient models for each type of wind turbine and PV. The differential equations of the wind turbine and PV models are integrated and converted to algebraic equations via trapezoidal method. The linear algebraic equations are combined with the nodal admittance equation of the distribu-

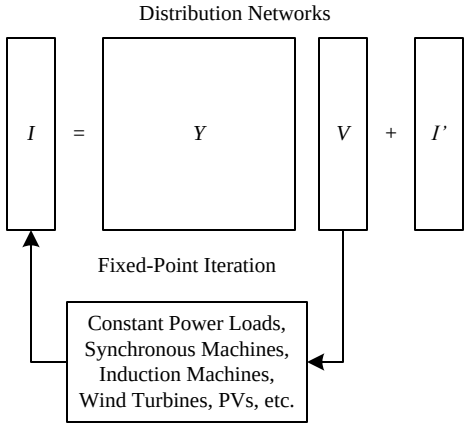

Figure 4.14: Interface of distribution network, wind turbine, and PV models for an electromagnetic transient simulation

tion network, and the nonlinear algebraic equations are solved by fixed-point iteration similar to the calculation approach for the steady-state simulation (Fig. 4.14). Note that the voltages and currents are recalculated every time step of the electromagnetic transient simulation.

4.1.3.1 FSWT Model

The electromagnetic transient model of an FSWT employs the full model of an induction generator described in (3.11)-(3.22). Since the simulation time is very short, the slip of the generator is assumed to be constant during the electromagnetic transient simulation. The voltage equations and flux linkage equations for an induction generator in (3.11)-(3.22) are combined and represented by

$$\frac{d}{dt}i_{qs} = -\frac{R_s}{L'_s}i_{qs} + \frac{R_r k_r}{L'_s}i_{qr} - \frac{\omega_s}{\sigma}\left[(i_{ds} + k_s i_{dr}) - s_1 k_s\left(i_{dr} + k_r i_{ds}\right)\right] + \frac{1}{L'_s}v_{qs} - \frac{1}{L'_m}v_{qr} \tag{4.27}$$

$$\frac{d}{dt}i_{ds} = -\frac{R_s}{L'_s}i_{ds} + \frac{R_r k_r}{L'_s}i_{dr} + \frac{\omega_s}{\sigma}\left[(i_{qs} + k_s i_{qr}) - s_1 k_s\left(i_{qr} + k_r i_{qs}\right)\right] + \frac{1}{L'_s}v_{ds} - \frac{1}{L'_m}v_{dr} \tag{4.28}$$

$$\frac{d}{dt}i_{os} = -\frac{R_s}{L_{ls}}i_{os} + \frac{1}{L_{ls}}v_{os} \tag{4.29}$$

$$\frac{d}{dt}i_{qr} = -\frac{R_r}{L'_r}i_{qr} + \frac{R_s k_s}{L'_r}i_{qs} - \frac{\omega_s}{\sigma}\left[s_1\left(i_{dr} + k_r i_{ds}\right) - k_r\left(i_{ds} + k_s i_{dr}\right)\right] + \frac{1}{L'_r}v_{qr} - \frac{1}{L'_m}v_{qs} \tag{4.30}$$

$$\frac{d}{dt}i_{dr} = -\frac{R_r}{L'_r}i_{dr} + \frac{R_s k_s}{L'_r}i_{ds} + \frac{\omega_s}{\sigma}\left[s_1\left(i_{qr} + k_r i_{qs}\right) - k_r\left(i_{qs} + k_s i_{qr}\right)\right] + \frac{1}{L'_r}v_{dr} - \frac{1}{L'_m}v_{ds} \tag{4.31}$$

$$\frac{d}{dt}i_{or} = -\frac{R_r}{L_{lr}}i_{or} + \frac{1}{L_{lr}}v_{or} \tag{4.32}$$

where L'_s, L'_r, L'_m, k_s, k_r, and σ are defined as follows:

$$L'_s = L_{ls} + \frac{L_{lr}L_m}{L_{lr} + L_m} \tag{4.33}$$

$$L'_r = L_{lr} + \frac{L_{ls}L_m}{L_{ls} + L_m} \tag{4.34}$$

$$L'_m = L_{ls} + L_{lr} + \frac{L_{ls}L_{lr}}{L_m} \tag{4.35}$$

$$k_s = \frac{L_m}{L_{ls} + L_m} \tag{4.36}$$

$$k_r = \frac{L_m}{L_{lr} + L_m} \tag{4.37}$$

$$\sigma = 1 - \frac{L_m^2}{\left(L_{ls} + L_m\right)\left(L_{lr} + L_m\right)} \tag{4.38}$$

The combined equations in (4.27)-(4.32) can be written in a vector form as

$$\frac{d}{dt}I = f\left(I\right) + g\left(V\right) \tag{4.39}$$

where f and g are functions of the induction generator currents (I) and voltages (V), respectively. The induction generator currents (I) and voltages (V) are defined as follows:

$$I = \begin{bmatrix} i_{qs} \\ i_{ds} \\ i_{os} \\ i_{qr} \\ i_{dr} \\ i_{or} \end{bmatrix} \tag{4.40}$$

$$V = \begin{bmatrix} v_{qs} \\ v_{ds} \\ v_{os} \\ v_{qr} \\ v_{dr} \\ v_{or} \end{bmatrix} \tag{4.41}$$

Integrating (4.39) by trapezoidal method yields

$$I(t) = I(t-\Delta t) + \frac{\Delta t}{2}\left[f(I(t)) + g(V(t)) + f(I(t-\Delta t)) + g(V(t-\Delta t))\right] \tag{4.42}$$

Rearranging (4.42) to describe the relation between the node voltage and injected current results in

$$I(t) = \frac{\Delta t}{2} g(V(t)) + I_h(t-\Delta t) \tag{4.43}$$

where the history term is defined as

$$I_h(t-\Delta t) = I(t-\Delta t) + \frac{\Delta t}{2}\left[f(I(t)) + f(I(t-\Delta t)) + g(V(t-\Delta t))\right] \tag{4.44}$$

The current $I(t-\Delta t)$ in (4.44) is calculated by using (4.43) as follows:

$$I(t-\Delta t) = \frac{\Delta t}{2} g(V(t-\Delta t)) + I_h(t-2\Delta t) \tag{4.45}$$

The current $I(t)$ in (4.44) is calculated by using the Euler method as follows:

$$I(t) = I(t-\Delta t) + \Delta t\left[f(I(t-\Delta t)) + g(V(t-\Delta t))\right] \tag{4.46}$$

Substituting $I(t-\Delta t)$ and $I(t)$ from (4.45) and (4.46) into (4.44) yields

$$I_h(t-\Delta t) = I_h(t-2\Delta t) + \frac{\Delta t}{2}\left[F_1 + F_2 + 2g(V(t-\Delta t))\right] \tag{4.47}$$

where F_1 and F_2 are defined as

$$F_1 = f(I(t-\Delta t)) = f\left(I_h(t-2\Delta t) + \frac{\Delta t}{2} g(V(t-\Delta t))\right) \tag{4.48}$$

$$F_2 = f(I(t)) = f\left(I_h(t-2\Delta t) + \frac{\Delta t}{2}\left[2F_1 + 3g(V(t-\Delta t))\right]\right) \tag{4.49}$$

4.1.3.2 WSWT Model

Like an FSWT model, an electromagnetic transient model of a WSWT employs (4.43) and (4.47). Since the simulation time is very short, the external rotor resistance, in addition to the slip, is assumed to be constant during the electromagnetic transient simulation. Thus, the external rotor resistance is set to its steady-state value calculated right before the electromagnetic transient simulation starts.

4.1.3.3 DFIG and Full Converter Wind Turbine Model

The model of DFIG and full converter wind turbines in an electromagnetic transient condition is similar to the model for an electromechanical transient simulation, i.e., the wind turbines are represented by a current source with decoupled real and reactive power controls. However, the equations for the PI controllers are integrated via the trapezoidal method as follows:

For the real power control, the PI controller calculates the q-axis current by

$$\begin{aligned} i_q(t) = K_{p,p}\left[P_{ref} - \frac{3}{2}v_q(t)\, i_q(t)\right] + K_{i,p}\int_{t-\Delta t}^{t}\left[P_{ref} - \frac{3}{2}v_q(t)\, i_q(t)\right]dt \\ + i_q(t-\Delta t) - K_{p,p}\left[P_{ref} - \frac{3}{2}v_q(t-\Delta t)\, i_q(t-\Delta t)\right] \end{aligned} \tag{4.50}$$

Applying the trapezoidal method yields

$$i_q(t) = \left(K_{p,p} + \frac{K_{i,p}\Delta t}{2}\right)\left[P_{ref} - \frac{3}{2}v_q(t)\, i_q(t)\right] + i'_q(t-\Delta t) \tag{4.51}$$

Hence, the q-axis current is calculated by

$$i_q(t) = \frac{\left(K_{p,p} + \frac{K_{i,p}\Delta t}{2}\right)P_{ref} + i'_q(t-\Delta t)}{1 + \frac{3}{2}\left(K_{p,p} + \frac{K_{i,p}\Delta t}{2}\right)v_q(t)} \tag{4.52}$$

where the history term is defined as

$$i'_q(t-\Delta t) = i_q(t-\Delta t) - \left(K_{p,p} - \frac{K_{i,p}\Delta t}{2}\right)\left[P_{ref} - \frac{3}{2}v_q(t-\Delta t)\, i_q(t-\Delta t)\right] \tag{4.53}$$

Substituting $v_q(t-\Delta t)$ from (4.51) into (4.53) yields

$$i'_q(t-\Delta t) = \frac{K_{p,p} - \frac{K_{i,p}\Delta t}{2}}{K_{p,p} + \frac{K_{i,p}\Delta t}{2}} i'_q(t-2\Delta t) + \left[1 - \frac{K_{p,p} - \frac{K_{i,p}\Delta t}{2}}{K_{p,p} + \frac{K_{i,p}\Delta t}{2}}\right] i_q(t-\Delta t) \tag{4.54}$$

For the reactive power control, the PI controller calculates the d-axis current by

$$\begin{aligned} i_d(t) = {} & K_{p,q}\left[Q_{ref} - \frac{3}{2}v_q(t)\, i_d(t)\right] + K_{i,q}\int_{t-\Delta t}^{t}\left[Q_{ref} - \frac{3}{2}v_q(t)\, i_d(t)\right] dt \\ & + i_d(t-\Delta t) - K_{p,q}\left[Q_{ref} - \frac{3}{2}v_q(t-\Delta t)\, i_d(t-\Delta t)\right] \end{aligned} \tag{4.55}$$

Applying the trapezoidal method yields

$$i_d(t) = \left(K_{p,q} + \frac{K_{i,q}\Delta t}{2}\right)\left[Q_{ref} - \frac{3}{2}v_q(t)\, i_d(t)\right] + i'_d(t-\Delta t) \tag{4.56}$$

Hence, the d-axis current is calculated by

$$i_d(t) = \frac{\left(K_{p,q} + \frac{K_{i,q}\Delta t}{2}\right) Q_{ref} + i'_d(t-\Delta t)}{1 + \frac{3}{2}\left(K_{p,q} + \frac{K_{i,q}\Delta t}{2}\right) v_q(t)} \tag{4.57}$$

where the history term is defined as

$$i'_d(t-\Delta t) = i_d(t-\Delta t) - \left(K_{p,q} - \frac{K_{i,q}\Delta t}{2}\right)\left[Q_{ref} - \frac{3}{2}v_q(t-\Delta t)\, i_d(t-\Delta t)\right] \tag{4.58}$$

Substituting $v_q(t-\Delta t)$ from (4.56) into (4.58) yields

$$i'_d(t-\Delta t) = \frac{K_{p,q} - \frac{K_{i,q}\Delta t}{2}}{K_{p,q} + \frac{K_{i,q}\Delta t}{2}} i'_d(t-2\Delta t) + \left[1 - \frac{K_{p,q} - \frac{K_{i,q}\Delta t}{2}}{K_{p,q} + \frac{K_{i,q}\Delta t}{2}}\right] i_d(t-\Delta t) \tag{4.59}$$

Since the simulation time is very short, the reference real and reactive power as well as the q-axis voltage in (4.52) and (4.57) are assumed to be constant during the electromagnetic transient simulation.

4.1.3.4 PV Model

The PV model for an electromagnetic transient simulation is a current source model, similar to the PV model for an electromechanical transient simulation. However, the trapezoidal method is used to integrate the equations for the PI controllers, similar to the model of DFIG and full converter wind turbines in an electromagnetic transient condition. Note that the real and reactive power of three-phase PVs can be calculated by (4.17) and (4.18), and the q- and d-axes currents of three-phase PVs are the same as those in (4.52) and (4.57). However, the real and reactive power of single-phase PVs can be calculated by (4.25) and (4.26). By following the similar calculation approach for DFIG and full converter wind turbines, the q- and d-axes currents of single-phase PVs are calculated by

$$i_q(t) = \frac{\left(K_{p,p} + \frac{K_{i,p}\Delta t}{2}\right) P_{ref} + i'_q(t - \Delta t)}{1 + \frac{1}{2}\left(K_{p,p} + \frac{K_{i,p}\Delta t}{2}\right) v_q(t)} \tag{4.60}$$

$$i_d(t) = \frac{\left(K_{p,q} + \frac{K_{i,q}\Delta t}{2}\right) Q_{ref} + i'_d(t - \Delta t)}{1 + \frac{1}{2}\left(K_{p,q} + \frac{K_{i,q}\Delta t}{2}\right) v_q(t)} \tag{4.61}$$

The history terms are the same as those described in (4.54) and (4.59).

Like the DFIG and full converter wind turbine model, the reference real and reactive power as well as the q-axis voltage in (4.60) and (4.61) are also assumed to be constant.

4.2 Model Selection and Switching between Models

The multi-time-scale simulation tool consists of three single-time-scale models, i.e., steady-state, electromechanical transient, and electromagnetic transient models. This section describes the integration of three single-time-scale models into the multi-time-scale simulation including the approaches to determine which single-time-scale

Table 4.1: Selected models for sample disturbances

Sample disturbance	Selected model
Wind and solar variation	Steady-state
Fault	Electromechanical transient
Capacitor switching	Electromagnetic transient

model to use in the multi-time-scale simulation, when to use each single-time-scale model, and when to switch to another single-time-scale model.

The single-time-scale models are pre-selected according to the types of each disturbance (Table 4.1) occur in the distribution circuit before the simulation starts. Fig. 4.15 shows the sample time line for a multi-time-scale simulation with multiple disturbances. The sequence of the single-time-scale models used in the multi-time-scale simulation in Fig. 4.15 is summarized in Fig. 4.16. As shown in Fig. 4.16, the multi-time-scale simulation involves switching between two single-time-scale model, i.e., between the steady-state and electromechanical transient models, and between the steady-state and electromagnetic transient models. In order to smoothly switch between two single-time-scale models, the energy stored in each storage element (inductor, capacitor, inertia, and spring) in both single-time-scale models must be the same. This condition suggests that the voltages, currents, torques, and rotational speeds of every elements must be the same before and after switching between the models. This condition also implies that when the simulation switches from the steady-state model to the electromechanical or electromagnetic transient models or vice versa, the electromechanical or electromagnetic transient models must rest in a steady-state condition, i.e., the electromechanical or electromagnetic transients have already died down.

The simulation is performed by the steady-state model when quasi-steady-state disturbances such as wind speed and solar irradiance variations occur. Wind

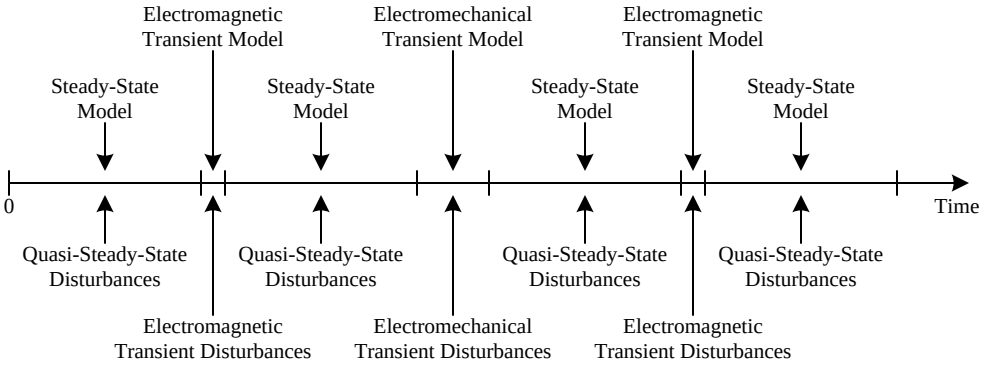

Figure 4.15: Time line for a multi-time-scale simulation

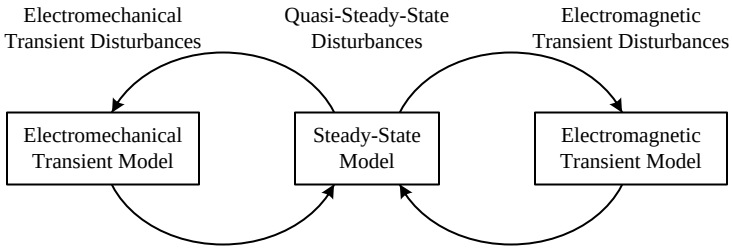

Figure 4.16: Multi-time-scale simulation diagram

speed and solar irradiance variations are considered as quasi-steady-state disturbances because the typical resolution of wind speed and solar irradiance data is much longer than the transient period.

The electromechanical transient model is used to simulate electromechanical transient disturbances such as short-circuit faults. The simulation starts by performing a steady-state simulation at the time right before the disturbance occurs. Then, the steady-state results are used to initialize the electromechanical transient model. Thus, the electromechanical transient simulation begins from the last quasi-steady-state condition before the disturbance occurs. When the disturbance occurs, the electromechanical transient model is used to obtain the simulation results in the

electromechanical transient period. When the power system reaches steady-state, the electromechanical transient results at the last time step are used to initialize the steady-state model so that the system conditions before and after switching are the same.

For electromagnetic transient disturbances such as capacitor switching, the steady-state model is used first to obtain results at the last quasi-steady-state condition before the disturbance occurs. Then, the steady-state results are used to initialize the electromagnetic transient model. Therefore, the electromagnetic transient simulation starts from the quasi-steady-state condition at the time right before the disturbance occurs. When the disturbance occurs, the electromagnetic transient model is used to simulate results in the electromagnetic transient period. After the electromagnetic transient dies down and the system reaches a steady-state condition, the electromagnetic transient results are used to initialize the steady-state model so that the system conditions before and after switching are the same.

Chapter 5

Simulation of Distribution Circuits

This chapter describes the case studies for the multi-time-scale simulations including the test circuits, simulation results, and discussions. The models of distribution circuits including wind turbines and PVs are developed in MATLAB^{TM}. Quasi-steady-state and multi-time-scale simulations are performed for four types of renewable energy sources, i.e., an FSWT, a WSWT, DFIG and full converter wind turbines, and a PV.

5.1 Test Circuits

This section describes the test circuits used to evaluate the performance of the multi-time-scale simulation. There are two test circuits used in this research: the four-node test circuit for wind turbine simulations and the three-node test circuit for PV simulations.

5.1.1 Four-Node Test Circuit for Wind Turbine Simulation

The test circuit used for the wind turbine simulations is modified from IEEE four-node test feeder [78]. The one-line diagram of the four-node test circuit is shown in Fig. 5.1.

The test circuit is a four-node unbalanced distribution circuit consisting of a 12.47-kV infinite bus, two unbalanced four-wire distribution lines, a 6-MVA three-phase wye-grounded and wye-grounded transformer, a 0.7-Mvar three-phase capacitor

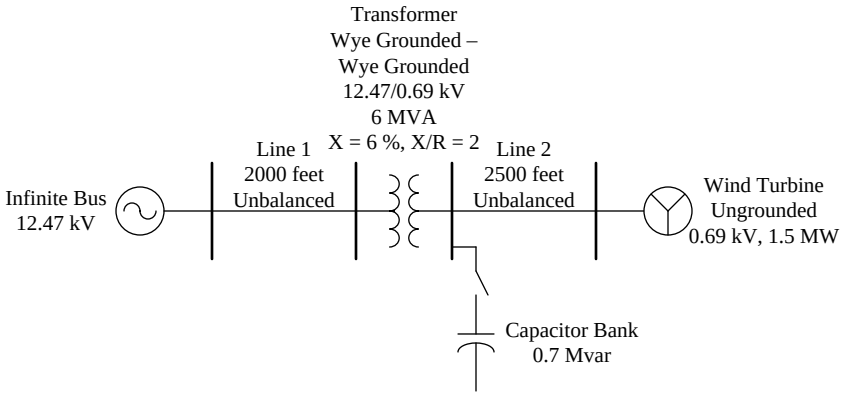

Figure 5.1: One-line diagram of the four-node test circuit for wind turbine simulations

bank, and a 1.5-MW ungrounded wind turbine. Line 1 is connected to the infinite bus and the transformer while Line 2 is connected to the transformer and the wind turbine. The capacitor bank is connected to the low voltage side of the transformer. The wind turbine consists of FSWTs, WSWTs, DFIG wind turbines, and full converter wind turbines. The radius of the wind turbine blade is 36 m, and the air density is 1.225 kg/m^2. The parameters of the mechanical system are given in Table 5.1. The ratings of the wind turbine generators of the wind turbine are 1.8 MVA and 690 V. The generators have six poles (three pole pairs). The parameters of the SCIG and WRIG are shown in Tables 5.2 and 5.3, respectively. The transformer resistance and reactance are 3 % and 6 %, respectively. The lengths of Lines 1 and 2 are 2000 and 2500 feet, respectively. The series resistance, series reactance, and shunt admittance matrices of Lines 1 and 2 are

$$r_{l1} = \begin{bmatrix} 0.4013 & 0.0953 & 0.0953 & 0.0953 \\ 0.0953 & 0.4013 & 0.0953 & 0.0953 \\ 0.0953 & 0.0953 & 0.4013 & 0.0953 \\ 0.0953 & 0.0953 & 0.0953 & 0.6873 \end{bmatrix} \Omega/\text{mile} \tag{5.1}$$

Table 5.1: Parameters of the mechanical system

Parameters	Blade	Generator
Inertia (kgm^2)	4940500	82.62
Shaft damping constant (Nms/rad)	13446	30.48
Shaft spring constant (Nm/rad)	97789000	2930000
Gear ratio	70.2	1

Table 5.2: Parameters of the SCIG

Parameters	Resistance	Reactance
Stator impedance (pu)	0.00540	0.102
Rotor impedance (pu)	0.00607	0.110
Magnetizing impedance (pu)	0	4.362

$$x_{l1} = \begin{bmatrix} j1.4133 & j0.8515 & j0.7266 & j0.7524 \\ j0.8515 & j1.4133 & j0.7802 & j0.7865 \\ j0.7266 & j0.7802 & j1.4133 & j0.7674 \\ j0.7524 & j0.7865 & j0.7674 & j1.5465 \end{bmatrix} \Omega/\text{mile} \tag{5.2}$$

$$y_{l1} = \begin{bmatrix} j5.6711 & -j1.8362 & -j0.7033 & -j0.8450 \\ -j1.8362 & j5.9774 & -j1.1690 & -j1.0745 \\ -j0.7033 & -j1.1690 & j5.3910 & -j1.0805 \\ -j0.8450 & -j1.0745 & -j1.0805 & j5.3411 \end{bmatrix} \mu\text{S/mile} \tag{5.3}$$

$$r_{l2} = \begin{bmatrix} 0.01104 & 0.00262 & 0.00262 & 0.00262 \\ 0.00262 & 0.01104 & 0.00262 & 0.00262 \\ 0.00262 & 0.00262 & 0.01104 & 0.00262 \\ 0.00262 & 0.00262 & 0.02062 & 0.01891 \end{bmatrix} \Omega/\text{mile} \tag{5.4}$$

$$x_{l2} = \begin{bmatrix} j0.03888 & j0.02343 & j0.01999 & j0.02070 \\ j0.02343 & j0.03888 & j0.02146 & j0.02164 \\ j0.01999 & j0.02146 & j0.03888 & j0.02111 \\ j0.02070 & j0.02164 & j0.02111 & j0.04255 \end{bmatrix} \Omega/\text{mile} \tag{5.5}$$

$$y_{l2} = \begin{bmatrix} j0.20614 & -j0.06674 & -j0.02556 & -j0.03071 \\ -j0.06674 & j0.21727 & -j0.04249 & -j0.03906 \\ -j0.02556 & -j0.04249 & j0.19596 & -j0.03927 \\ -j0.03071 & -j0.03906 & -j0.03927 & j0.19414 \end{bmatrix} \text{mS/mile} \tag{5.6}$$

Table 5.3: Parameters of the WRIG

Parameters	Resistance	Reactance
Stator impedance (pu)	0.00473	0.0802
Rotor impedance (pu)	0.02389	0.0476
Magnetizing impedance (pu)	0	6.8318

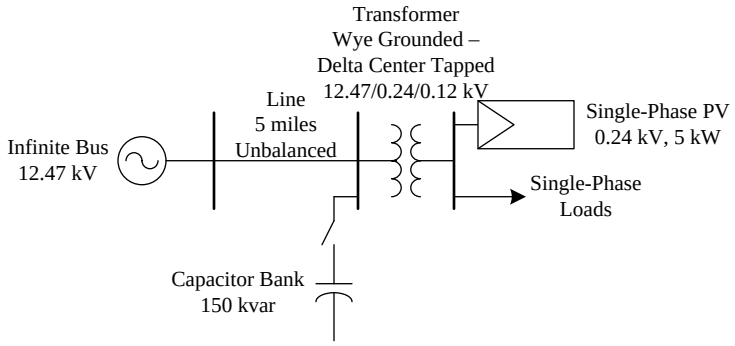

Figure 5.2: One-line diagram of the three-node test circuit for PV simulations

where r_{l1} and r_{l2} are the series resistance matrices of Lines 1 and 2, x_{l1} and x_{l2} are the series reactance matrices of Lines 1 and 2, and y_{l1} and y_{l2} are the shunt admittance matrices of Lines 1 and 2. Note that the matrices r_{l1}, x_{l1}, y_{l1}, r_{l2}, x_{l2}, and y_{l2} are not symmetrical because Lines 1 and 2 are unbalanced.

5.1.2 Three-Node Test Circuit for PV Simulation

The test circuit used for the PV simulations is modified from IEEE four-node test feeder [79–82]. The one-line diagram of the three-node test circuit is shown in Fig. 5.2.

The test circuit is a three-node unbalanced distribution circuit consisting of a 12.47-kV infinite bus, an unbalanced four-wire distribution line, a three-phase wye-grounded and delta-center-tapped transformer, a 150-kvar three-phase capaci-

Table 5.4: Transformer data

Phase	Rated voltage (V)	Rated power (kVA)	Resistance (%)	Reactance (%)
AN-ABN	7200/120/120	25	Primary: 1.2 Secondary 1: 2.4 Secondary 2: 2.4	Primary-Secondary 1: 2.04 Primary-Secondary 2: 2.04 Secondary 1-Secondary 2: 1.36
BN-BC	7200/240	10	3.2	1.4
CN-CA	7200/240	10	3.2	1.4

Table 5.5: Load data

Phase	Rated voltage (V)	Rated power (kVA)	Power factor
AN	120	3	0.95 (lagging)
BN	120	5	0.85 (lagging)
AB	240	10	0.90 (lagging)
BC	240	8	0.88 (lagging)
CA	240	13	0.93 (lagging)

tor bank, single-phase loads, and a 5-kW single-phase PV. The distribution line is connected to the infinite bus and the high voltage side of the transformer, the capacitor bank is connected to the high voltage side of the transformer, the loads are connected to the low voltage side of the transformer, and the PV is connected to Phases A and B of the low voltage side of the transformer. The lengths of the distribution line is 5 miles. The series resistance, series reactance, and shunt admittance matrices of the line are identical to the line parameters given in (5.1)-(5.3). The transformer and load data are given in Tables 5.4 and 5.5, respectively.

5.2 Verification of Test Circuit Models

This section describes the verification of the test circuit models developed in MATLAB^{TM} for wind turbine and PV simulations. In order to verify the models, the steady-state results and the electromagnetic transient results obtained from the proposed multi-time-scale simulation tool developed in MATLAB^{TM} are compared to the

Table 5.6: Load data for the test circuit verification

Phase	Rated voltage (V)	Rated power (kW)	Power factor
A	398	255	0.85 (lagging)
B	398	360	0.90 (lagging)
C	398	475	0.95 (lagging)

Table 5.7: Comparison of node voltage results for the four-node test circuit when the capacitor is offline

Simulation tool		MATLAB^{TM}	OpenDSS^{TM}
Voltage at the load bus (pu)	Phase A	$0.9789\angle -0.5°$	$0.9789\angle -0.5°$
	Phase B	$0.9656\angle -121.1°$	$0.9656\angle -121.1°$
	Phase C	$0.9678\angle 117.6°$	$0.9678\angle 117.6°$
Voltage at the low voltage side of the transformer (pu)	Phase A	$0.9905\angle -0.3°$	$0.9905\angle -0.3°$
	Phase B	$0.9876\angle -120.5°$	$0.9876\angle -120.5°$
	Phase C	$0.9865\angle 119.2°$	$0.9865\angle 119.2°$
Voltage at the high voltage side of the transformer (pu)	Phase A	$0.9990\angle 0.0°$	$0.9990\angle 0.0°$
	Phase B	$0.9980\angle -120.1°$	$0.9980\angle -120.1°$
	Phase C	$0.9983\angle 119.9°$	$0.9983\angle 119.9°$

results obtained from commercially available simulation tools, i.e., OpenDSS^{TM} for quasi-steady-state simulations and PSCAD/EMTDC^{TM} for electromagnetic transient simulations.

5.2.1 Verification of Test Circuit Model for Wind Turbine Simulation

For verification purposes, the wind turbine in the four-node test circuit in Fig. 5.1 is switched offline, and three single-phase loads described in Table 5.6 are installed at the end of the feeder. The node voltage results from MATLAB^{TM} and OpenDSS^{TM} in steady-state conditions when the capacitor bank is offline and online are compared in Tables 5.7 and 5.8, respectively. In order to verify the test circuit in an electromagnetic transient condition, the capacitor bank is switched on at time = 0. Figs. 5.3 and 5.4 illustrate the electromagnetic transient voltages at the load from MATLAB^{TM} and PSCAD/EMTDC^{TM}, respectively.

Table 5.8: Comparison of node voltage results for the four-node test circuit when the capacitor is online

Simulation tool		MATLAB™	OpenDSS™
Voltage at the load bus (pu)	Phase A	$0.9868\angle -0.8°$	$0.9868\angle -0.8°$
	Phase B	$0.9733\angle -121.3°$	$0.9733\angle -121.3°$
	Phase C	$0.9756\angle 117.3°$	$0.9756\angle 117.3°$
Voltage at the low voltage side of the transformer (pu)	Phase A	$0.9985\angle -0.6°$	$0.9985\angle -0.6°$
	Phase B	$0.9955\angle -120.7°$	$0.9955\angle -120.7°$
	Phase C	$0.9944\angle 119.0°$	$0.9944\angle 119.0°$
Voltage at the high voltage side of the transformer (pu)	Phase A	$1.0000\angle -0.1°$	$1.0000\angle -0.1°$
	Phase B	$0.9990\angle -120.1°$	$0.9990\angle -120.1°$
	Phase C	$0.9994\angle 119.8°$	$0.9994\angle 119.8°$

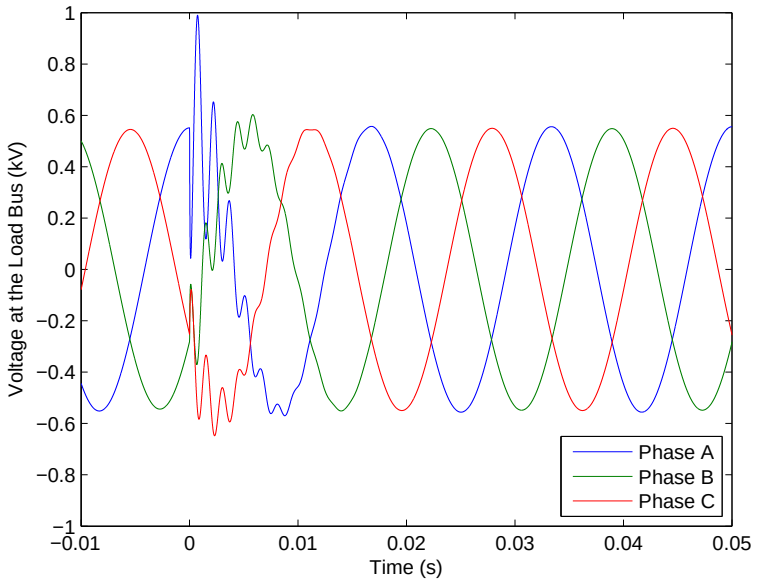

Figure 5.3: Load voltage of the four-node test circuit in MATLAB™

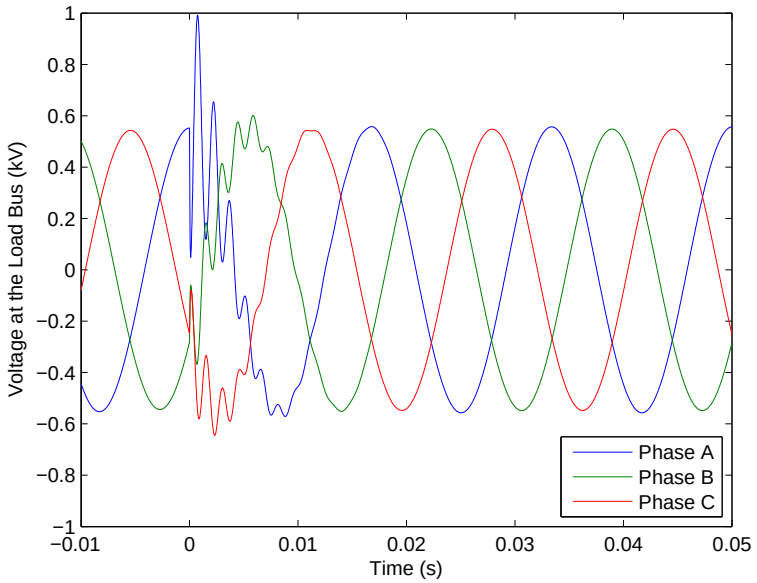

Figure 5.4: Load voltage of the four-node test circuit in PSCAD/EMTDC™

As can be seen in Tables 5.7 and 5.8, the steady-state voltage results from MATLAB™ and OpenDSS™ are exactly the same. In addition, the electromagnetic results of load voltages from MATLAB™ in Fig. 5.3 match the results from PSCAD/EMTDC™ in Fig. 5.4. Hence, the model of the four-node test circuit is verified.

5.2.2 Verification of Test Circuit Model for PV Simulation

For verification purposes, the PV in the three-node test circuit in Fig. 5.2 is switched offline. The node voltage results from MATLAB™ and OpenDSS™ in steady-state conditions when the capacitor bank is offline and online are compared in Tables 5.9 and 5.10, respectively. In order to verify the test circuit in an electromagnetic transient condition, the capacitor bank is switched on at time = 0. Figs. 5.5 and 5.6 illustrate the electromagnetic transient voltages at the load from MATLAB™

Table 5.9: Comparison of node voltage results for the three-node test circuit when the capacitor is offline

Simulation tool		MATLAB™	OpenDSS™
Voltage at the load bus (pu)	Phase A	$0.9761\angle -0.1°$	$0.9761\angle -0.1°$
	Phase B	$0.9743\angle -179.9°$	$0.9743\angle -179.9°$
	Phase C	$0.9651\angle 89.7°$	$0.9651\angle 89.7°$
Voltage at the high voltage side of the transformer (pu)	Phase A	$0.9983\angle -0.1°$	$0.9983\angle -0.1°$
	Phase B	$1.0003\angle -120.0°$	$1.0003\angle -120.0°$
	Phase C	$0.9996\angle 120.0°$	$0.9996\angle 120.0°$

Table 5.10: Comparison of node voltage results for the three-node test circuit when the capacitor is online

Simulation tool		MATLAB™	OpenDSS™
Voltage at the load bus (pu)	Phase A	$0.9790\angle -0.3°$	$0.9790\angle -0.3°$
	Phase B	$0.9773\angle -179.8°$	$0.9773\angle -179.8°$
	Phase C	$0.9681\angle 89.6°$	$0.9681\angle 89.6°$
Voltage at the high voltage side of the transformer (pu)	Phase A	$1.0014\angle -0.2°$	$1.0014\angle -0.2°$
	Phase B	$1.0031\angle -120.1°$	$1.0031\angle -120.1°$
	Phase C	$1.0028\angle 119.9°$	$1.0028\angle 119.9°$

and PSCAD/EMTDC™, respectively.

As can be seen in Tables 5.9 and 5.10, the steady-state voltage results from MATLAB™ and OpenDSS™ are exactly the same. In addition, the electromagnetic results of load voltages from MATLAB™ in Fig. 5.5 match the results from PSCAD/EMTDC™ in Fig. 5.6. Hence, the model of the three-node test circuit is verified.

5.3 Verification of Approach Used to Switch between Models

This section describes the verification of the approach used to switch between single-time-scale models. Four case studies are simulated for each type of wind turbine and PV. In order to verify the switching approach, two simulations are performed for each case.

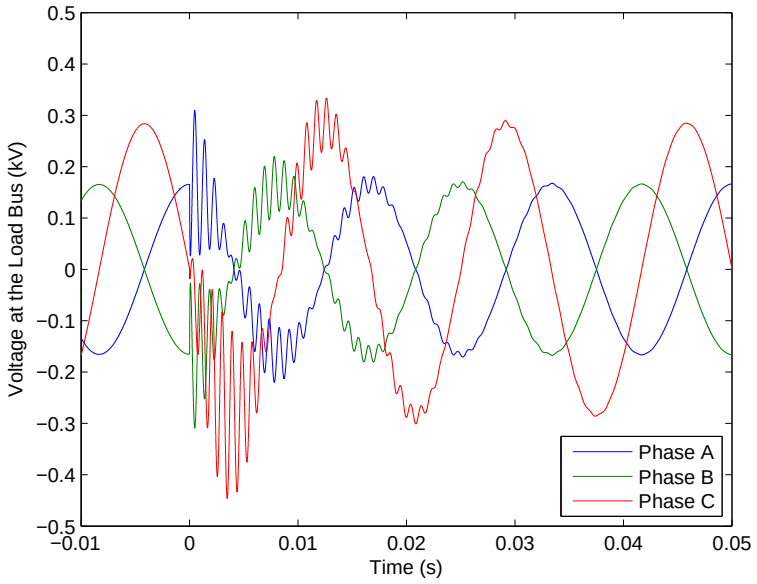

Figure 5.5: Load voltage of the three-node test circuit in MATLAB™

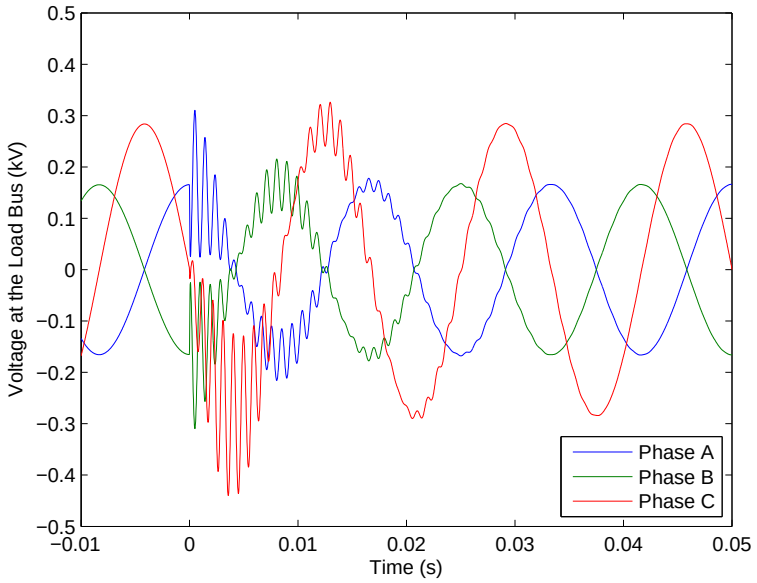

Figure 5.6: Load voltage of the three-node test circuit in PSCAD/EMTDC™

For the first simulation (switching between the steady-state and electromagnetic transient models), the simulation starts with the steady-state model. At time = 0, the simulation switches to the electromagnetic transient model. The simulation is then performed by using the electromagnetic transient model for 0.1 s. After that, the simulation switches back to the steady-state model again.

For the second simulation (switching between the steady-state and electromechanical transient models), the simulation starts with the steady-state model. At time = 0, the simulation switches to the electromechanical transient model. The simulation is then performed by using the electromechanical transient model for 1 s. After that, the simulation switches back to the steady-state model again.

5.3.1 Switching between Models for an FSWT

Figs. 5.7 and 5.8 describe the voltages and output currents of the wind turbine when switching between the steady-state and electromagnetic transient models. The voltages and output currents of the wind turbine before and after switching between the steady-state and electromechanical transient models are presented in Figs. 5.9 and 5.10.

According to Figs. 5.7 and 5.8, the voltage and current results from the steady-state and electromagnetic transient models are exactly the same. In addition, the voltages and currents continue smoothly after the switching. For switching between the steady-state and electromechanical transient models, the voltages and currents of the wind turbine are also the same (Figs. 5.9 and 5.10), and the simulation smoothly continues after the time of switching. These results indicate that the energy stored in the storage element before and after switching are the same.

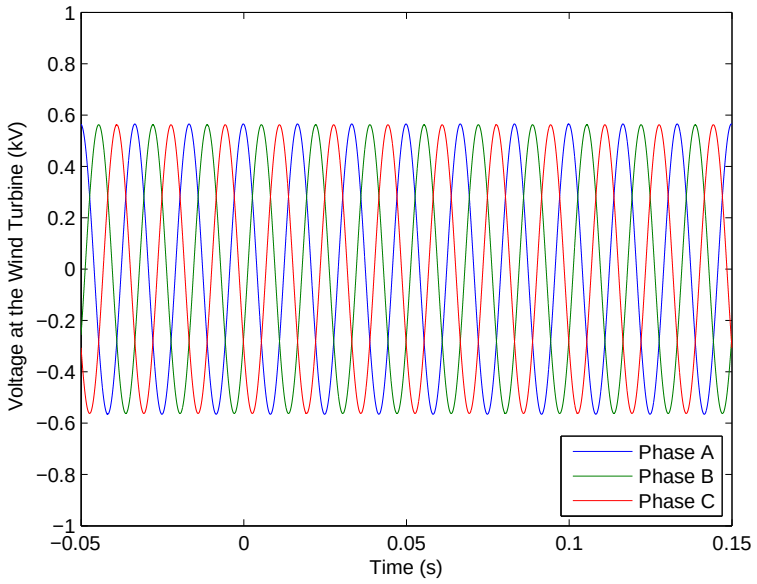

Figure 5.7: Voltages at the FSWT when switching between the steady-state and electromagnetic transient models

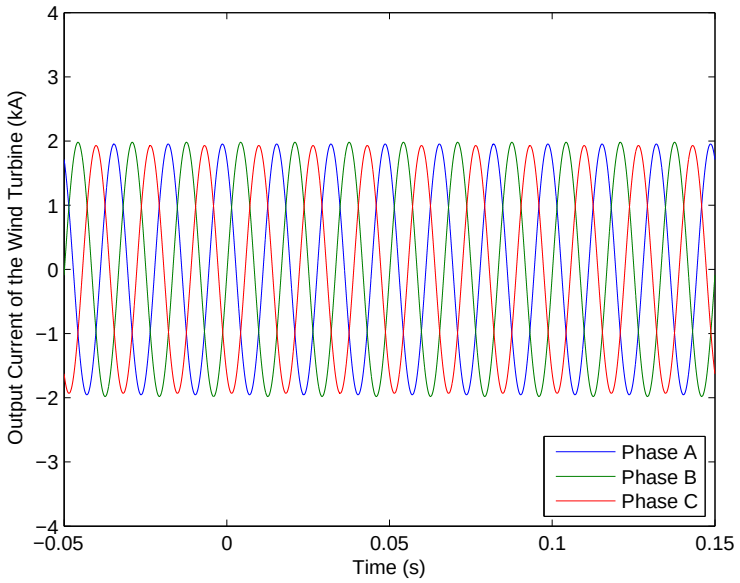

Figure 5.8: Output currents of the FSWT when switching between the steady-state and electromagnetic transient models

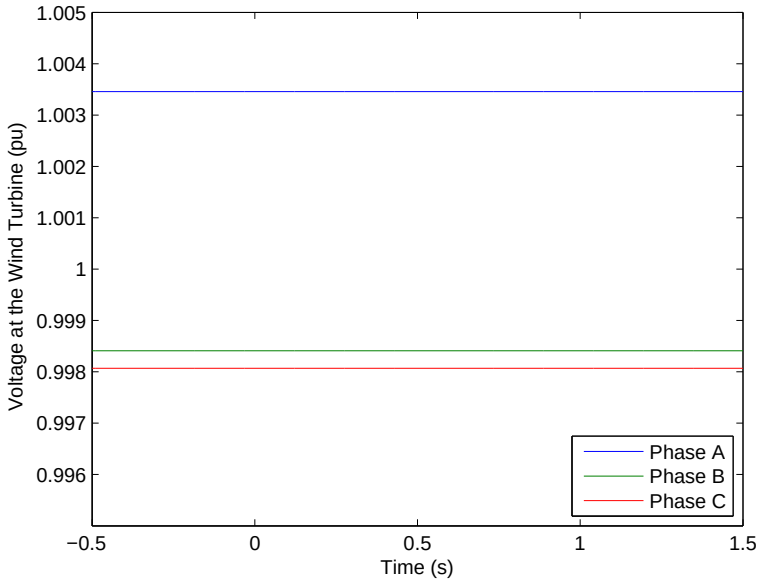

Figure 5.9: Voltages at the FSWT when switching between the steady-state and electromechanical transient models

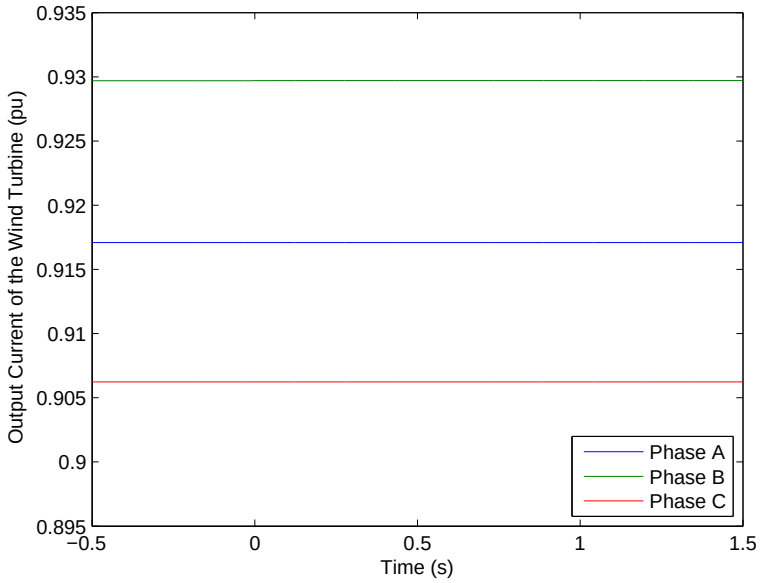

Figure 5.10: Output currents of the FSWT when switching between the steady-state and electromechanical transient models

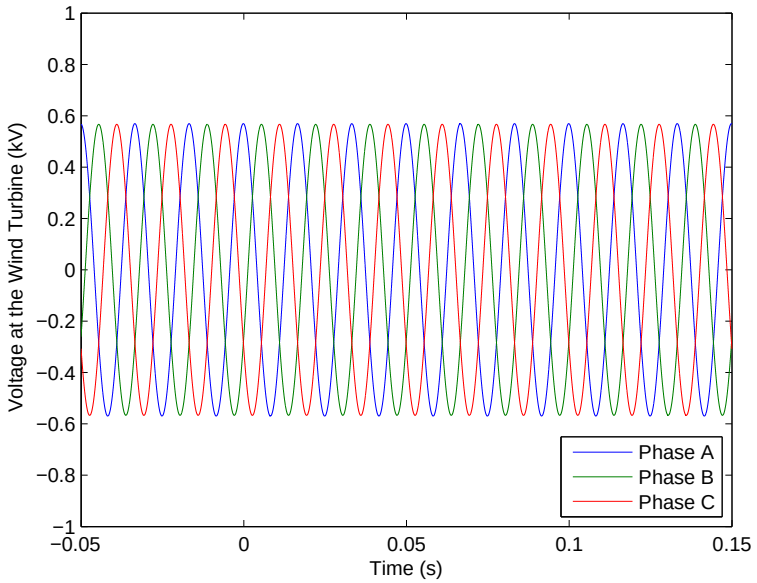

Figure 5.11: Voltages at the WSWT when switching between the steady-state and electromagnetic transient models

5.3.2 Switching between Models for a WSWT

The wind turbine voltage and current results before and after switching between the steady-state and electromagnetic transient models are shown in Figs. 5.11 and 5.12. Figs. 5.13 and 5.14 illustrate the voltages and output currents of the wind turbine when switching between the steady-state and electromechanical transient models.

As presented in Figs. 5.11 and 5.12, the simulation smoothly switches from the steady-state model to the electromagnetic transient model and vice versa. The results obtained from both steady-state and electromagnetic transient models are the same. Figs. 5.13 and 5.14 show that the simulation also continues smoothly when switching between the steady-state and electromechanical transient models, and the steady-state and electromechanical transient results are exactly the same. The results

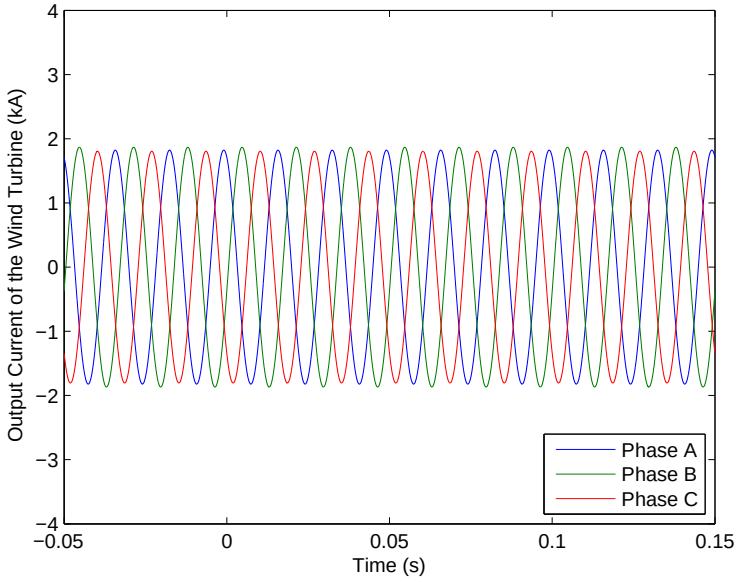

Figure 5.12: Output currents of the WSWT when switching between the steady-state and electromagnetic transient models

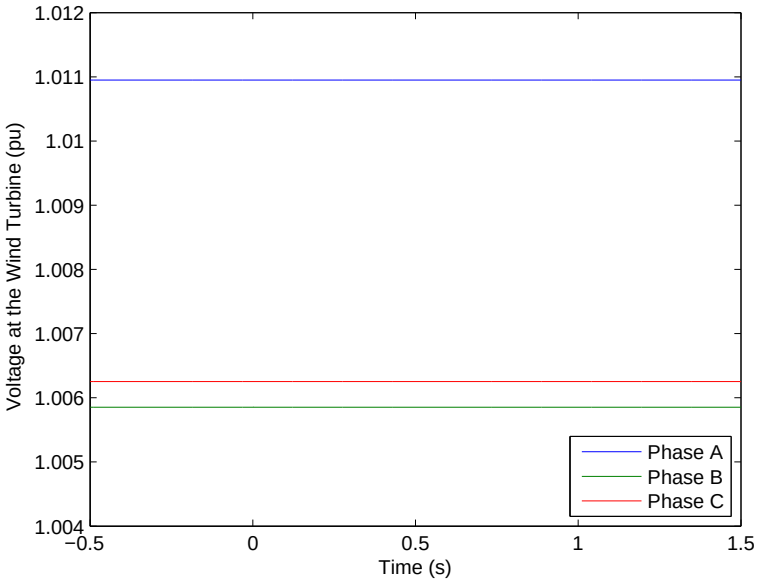

Figure 5.13: Voltages at the WSWT when switching between the steady-state and electromechanical transient models

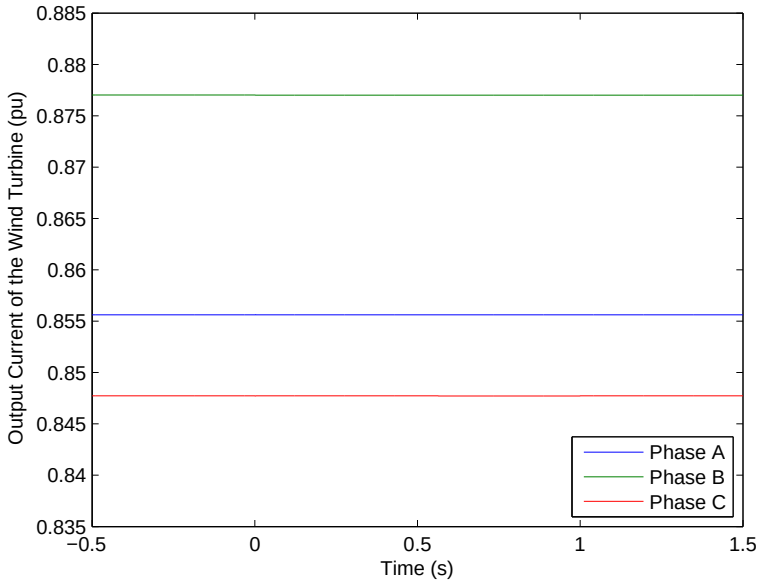

Figure 5.14: Output currents of the WSWT when switching between the steady-state and electromechanical transient models

imply that the energy in the storage element before and after the simulation switches between models are the same.

5.3.3 Switching between Models for DFIG and Full Converter Wind Turbines

Figs. 5.15 and 5.16 illustrate the voltages and currents of the wind turbine from the steady-state and electromagnetic transient models, and Figs. 5.17 and 5.18 present the wind turbine voltages and currents before and after switching between the steady-state and electromechanical transient models.

Figs. 5.15 and 5.16 show that the voltage and current results obtained from the steady-state and electromagnetic transient models are the same. The results also show that the simulation smoothly switches between the steady-state and electromagnetic transient models. The switching between the steady-state and electromechanical

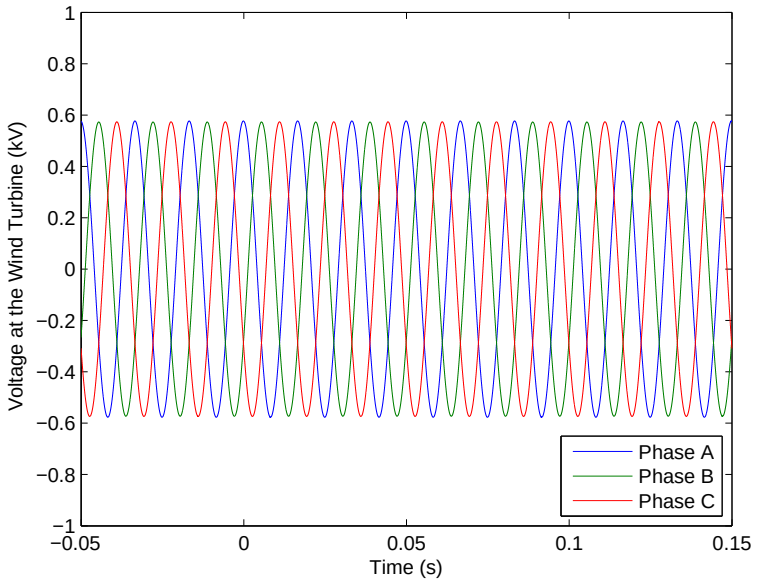

Figure 5.15: Voltages at the wind turbine when switching between the steady-state and electromagnetic transient models

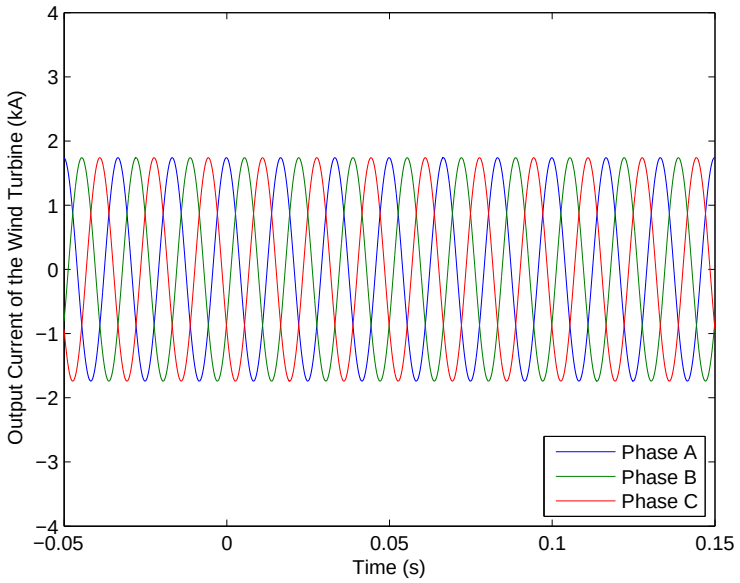

Figure 5.16: Output currents of the wind turbine when switching between the steady-state and electromagnetic transient models

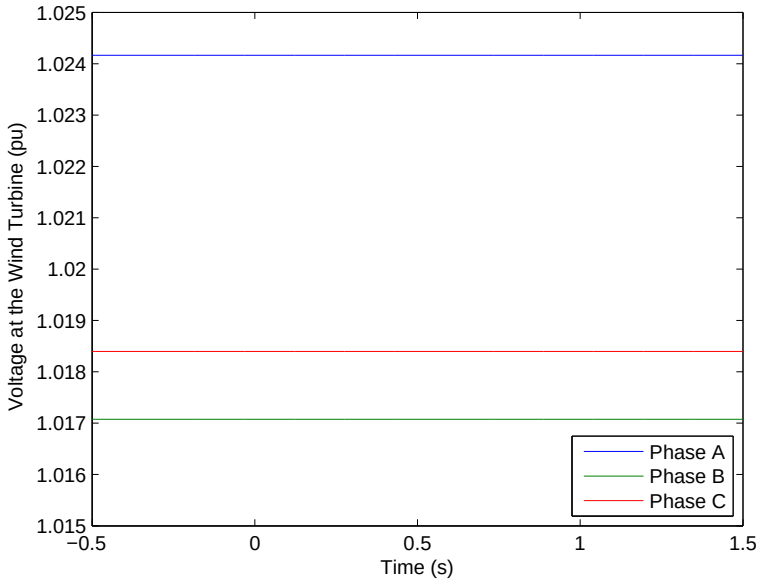

Figure 5.17: Voltages at the wind turbine when switching between the steady-state and electromechanical transient models

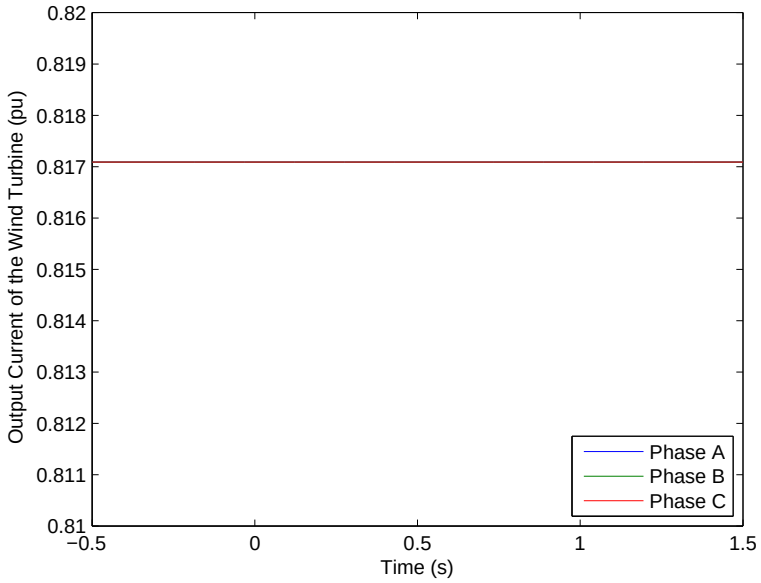

Figure 5.18: Output currents of the wind turbine when switching between the steady-state and electromechanical transient models

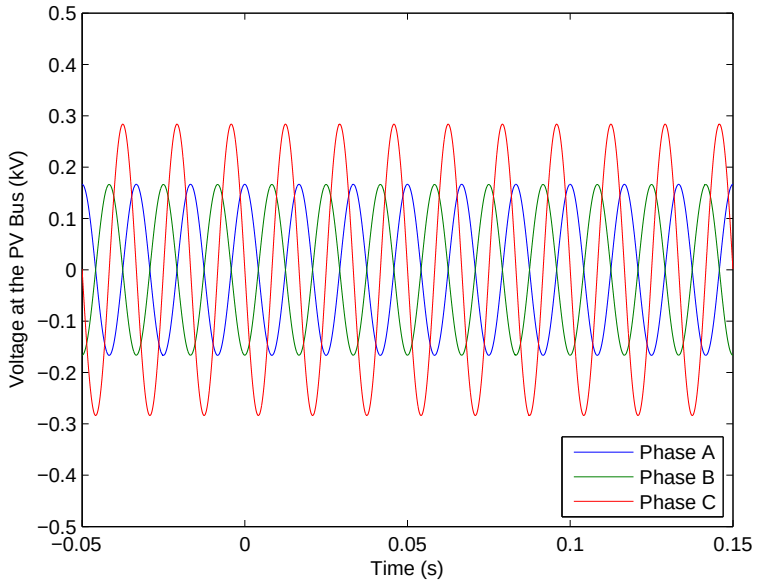

Figure 5.19: Voltages at the PV bus when switching between the steady-state and electromagnetic transient models

transient models also occurs smoothly, and the steady-state and electromechanical transient results are exactly the same as shown in Figs. 5.17 and 5.18. Thus, the energy in the storage element before and after switching between the models are preserved.

5.3.4 Switching between Models for a PV

The voltages and injected currents at the PV bus when switching between the steady-state and electromagnetic transient models are shown in Figs. 5.19 and 5.20, and the PV voltages and currents when switching from the steady-state model to the electromechanical transient model and vice versa are described in Figs. 5.21 and 5.22.

As described in Figs. 5.19 and 5.20, the simulation smoothly switches between the steady-state and electromagnetic transient models, and the steady-state

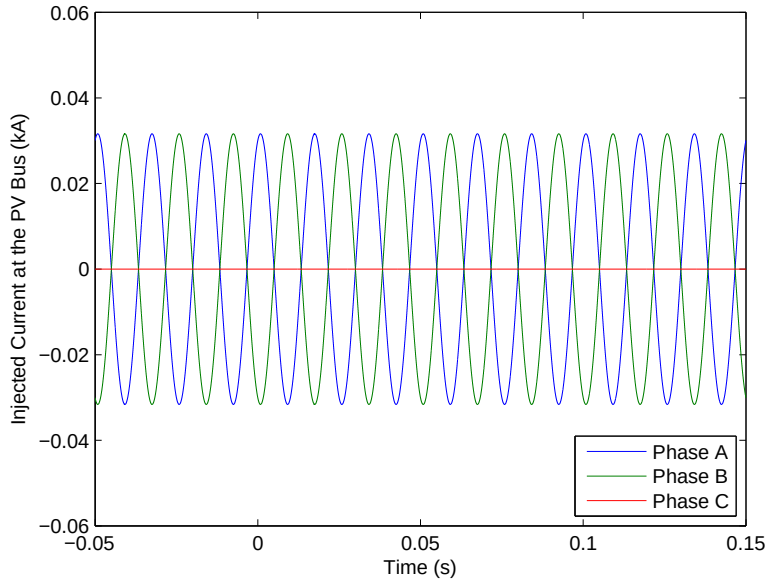

Figure 5.20: Injected currents at the PV bus when switching between the steady-state and electromagnetic transient models

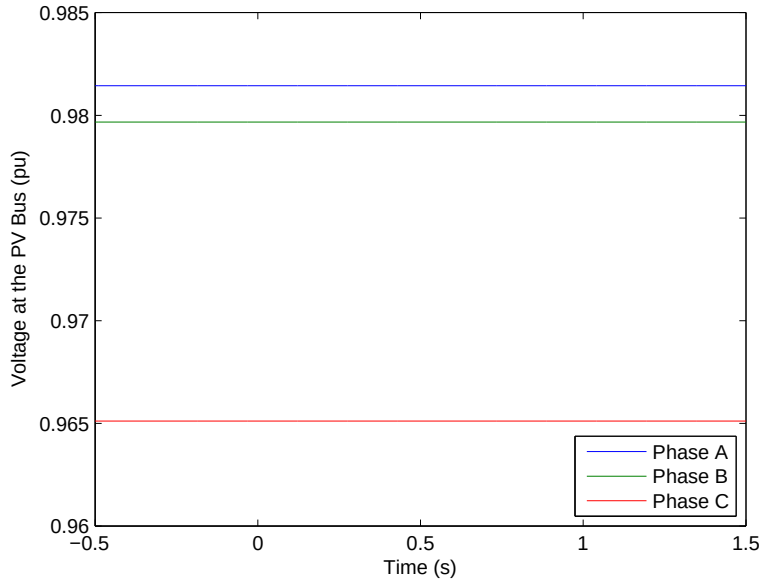

Figure 5.21: Voltages at the PV bus when switching between the steady-state and electromechanical transient models

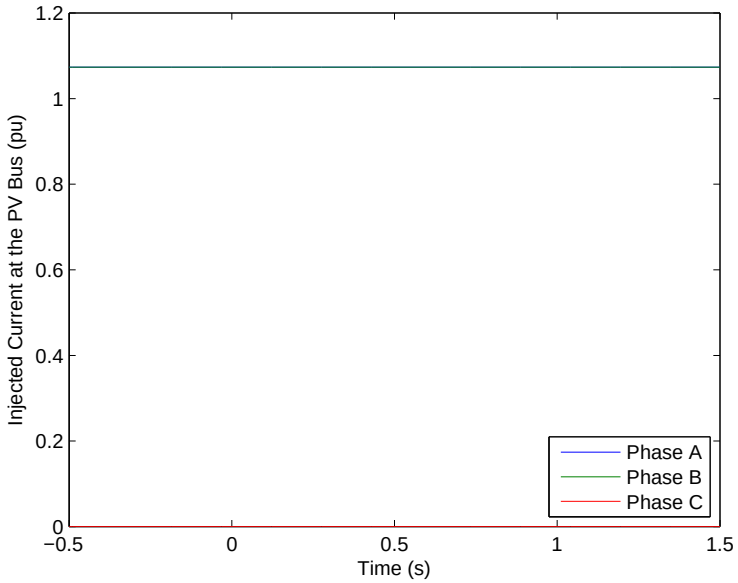

Figure 5.22: Injected currents at the PV bus when switching between the steady-state and electromechanical transient models

and electromagnetic transient results are the same. According to Figs. 5.21 and 5.22, the simulation also switches smoothly between the steady-state and electromechanical transient models, and the results from both models are the same. Therefore, the energy stored in the storage element before and after switching between the steady-state and electromagnetic transient models, and between electromechanical the steady-state and transient models are preserved.

5.4 Simulation Results and Discussion

This section describes the results and discussion of the multi-time-scale simulation models. The simulations are performed for each type of wind turbine and PV in MATLAB^{TM}.

Table 5.11: Quasi-steady-state results of the FSWT simulation

Wind speed (m/s)	Slip (%)	Real power produced by the wind turbine (MW)	Reactive power produced by the wind turbine (Mvar)
6	−0.029	0.080	−0.396
7	−0.091	0.254	−0.405
8	−0.177	0.493	−0.430
9	−0.272	0.758	−0.474
10	−0.364	1.015	−0.533
11	−0.441	1.223	−0.593
12	−0.499	1.377	−0.645
13	−0.536	1.471	−0.680
14	−0.547	1.500	−0.692
15	−0.541	1.484	−0.686
16	−0.515	1.417	−0.660
17	−0.484	1.337	−0.631
18	−0.438	1.215	−0.590
19	−0.395	1.095	−0.555
20	−0.356	0.990	−0.526

5.4.1 Simulation of an FSWT

Two case studies for an FSWT are simulated in this section: a quasi-steady-state simulation of an FSWT and a multi-time-scale simulation of an FSWT.

5.4.1.1 Quasi-Steady-State Simulation of an FSWT

This case considers a wind turbine consisting of an FSWT operating in the four-node test circuit in Fig. 5.1 in quasi-steady-state conditions. The capacitor bank in the test circuit is offline. The wind speed varies from the cut-in speed (6 m/s) to the cut-out speed (20 m/s) with an increment of 1 m/s. The wind turbine slip, and the real and reactive power produced by the wind turbine are shown in Table 5.11. The voltages at the wind turbine, the low voltage side of the transformer, and the high voltage side of the transformer are presented in Table 5.12.

As shown in Table 5.11, the wind turbine operates in the range where the

Table 5.12: Node voltage results of the FSWT simulation

Wind speed (m/s)	Voltage at the wind turbine (pu)			Voltage at the low voltage side of the transformer (pu)			Voltage at the high voltage side of the transformer (pu)		
	Phase A	Phase B	Phase C	Phase A	Phase B	Phase C	Phase A	Phase B	Phase C
6	0.990∠ 0.5°	0.990∠ −119.6°	0.989∠ 120.4°	0.996∠ 0.2°	0.996∠ −119.8°	0.996∠ 120.2°	0.999∠ 0.0°	0.999∠ −120.0°	0.999∠ 120.0°
7	0.992∠ 0.8°	0.992∠ −119.3°	0.991∠ 120.7°	0.997∠ 0.3°	0.997∠ −119.7°	0.997∠ 120.3°	1.000∠ 0.0°	1.000∠ −120.0°	1.000∠ 120.0°
8	0.995∠ 1.2°	0.994∠ −118.9°	0.994∠ 121.2°	0.998∠ 0.5°	0.998∠ −119.5°	0.998∠ 120.5°	1.000∠ 0.1°	1.000∠ −119.9°	1.000∠ 120.1°
9	0.998∠ 1.7°	0.996∠ −118.5°	0.996∠ 121.6°	0.999∠ 0.7°	0.999∠ −119.3°	0.999∠ 120.7°	1.000∠ 0.1°	1.000∠ −119.9°	1.000∠ 120.1°
10	1.001∠ 2.2°	0.997∠ −118.0°	0.997∠ 122.1°	0.999∠ 0.9°	0.999∠ −119.2°	0.999∠ 120.8°	1.000∠ 0.1°	1.000∠ −119.9°	1.000∠ 120.1°
11	1.002∠ 2.6°	0.998∠ −117.6°	0.998∠ 122.5°	1.000∠ 1.0°	1.000∠ −119.0°	1.000∠ 121.0°	1.000∠ 0.1°	1.000∠ −119.9°	1.000∠ 120.1°
12	1.003∠ 2.9°	0.998∠ −117.4°	0.998∠ 122.8°	1.000∠ 1.1°	1.000∠ −118.9°	1.000∠ 121.1°	1.000∠ 0.2°	1.000∠ −119.9°	1.000∠ 120.1°
13	1.003∠ 3.1°	0.998∠ −117.2°	0.998∠ 123.0°	1.000∠ 1.2°	1.000∠ −118.8°	1.000∠ 121.2°	1.000∠ 0.2°	1.000∠ −119.9°	1.000∠ 120.2°
14	1.003∠ 3.2°	0.998∠ −117.1°	0.998∠ 123.0°	1.000∠ 1.2°	1.000∠ −118.8°	1.000∠ 121.2°	1.000∠ 0.2°	0.998∠ −119.9°	1.000∠ 120.2°
15	1.003∠ 3.1°	0.998∠ −117.2°	0.998∠ 123.0°	1.000∠ 1.2°	1.000∠ −118.8°	1.000∠ 121.2°	1.000∠ 0.2°	1.000∠ −119.9°	1.000∠ 120.2°
16	1.003∠ 3.0°	0.998∠ −117.3°	0.998∠ 122.9°	1.000∠ 1.2°	1.000∠ −118.8°	1.000∠ 121.1°	1.000∠ 0.2°	1.000∠ −119.9°	1.000∠ 120.2°
17	1.003∠ 2.8°	0.998∠ −117.4°	0.998∠ 122.7°	1.000∠ 1.1°	1.000∠ −118.9°	1.000∠ 121.1°	1.000∠ 0.2°	1.000∠ −119.9°	1.000∠ 120.1°
18	1.002∠ 2.6°	0.998∠ −117.6°	0.998∠ 122.5°	1.000∠ 1.0°	1.000∠ −119.0°	1.000∠ 121.0°	1.000∠ 0.1°	1.000∠ −119.9°	1.000∠ 120.1°
19	1.001∠ 2.4°	0.998∠ −117.9°	0.997∠ 122.3°	0.999∠ 0.9°	0.999∠ −119.1°	0.999∠ 120.9°	1.000∠ 0.1°	1.000∠ −119.9°	1.000∠ 120.1°
20	1.001∠ 2.1°	0.997∠ −118.0°	0.997∠ 122.1°	0.999∠ 0.8°	0.999∠ −119.2°	0.999∠ 120.8°	1.000∠ 0.1°	1.000∠ −119.9°	1.000∠ 120.1°

slip is negative. The magnitude of the slip is less than 1% for all wind speeds, so the generator speed is almost constant. The generated real power increases when the wind speed increases from the cut-in to the rated speed, but the real power decreases when the wind speed is higher than the rated speed because of the stall control. Additionally, the wind turbine consumes reactive power for all wind speeds. From Table 5.12, the steady-state voltages are in an acceptable range (0.95-1.05 pu). Therefore, it can be concluded that the system operates in stable conditions.

5.4.1.2 Multi-Time-Scale Simulation of an FSWT

This case considers a wind turbine consisting of an FSWT in quasi-steady-state, electromechanical transient, and electromagnetic transient conditions. The simulation is performed for a 24-hour period. During this simulation period, wind speed changes every ten minutes. The ten-minute resolution wind speed data obtained from NREL [83] are shown in Fig. 5.23. When the simulation starts at 12:00 am, the capacitor bank is out of service. The capacitor bank is switched on at 8:00 am and switched off at 10:00 pm. A temporary bolted single-line-to-ground fault occurs on Phase A of the high voltage side of the transformer at 2:00 pm. The fault clears itself in 0.1 seconds. The simulation is performed by the steady-state model when wind speed changes because the resolution of wind speed data is ten minutes, which is much longer than the transient period. When the capacitor is turned on at 8:00 am, the simulation switches to the electromagnetic transient model because the capacitor switching is an electromagnetic transient phenomenon. As soon as the simulation reaches a steady-state condition, the simulation switches back to the steady-state model. At 2:00 pm, the fault occurs, so the simulation switches to the electromechanical transient model since the fault period of 0.1 seconds is in the electromechanical transient time scale. After the fault is cleared and the circuit reaches a steady-state condition, the

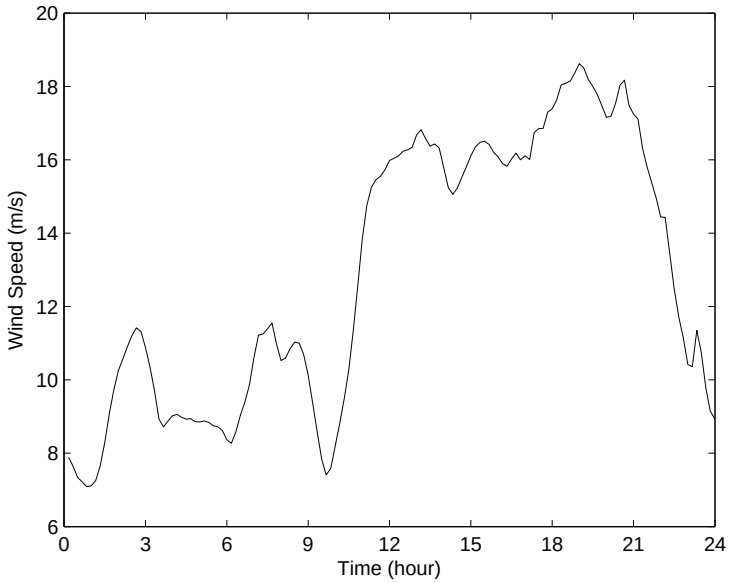

Figure 5.23: Wind speed for the multi-time-scale simulation

steady-state model is employed again. The capacitor is turned off at 10:00 pm, so the simulation switches to the electromagnetic transient model and switches back to the steady-state model when the simulation reaches a steady-state condition. Fig. 5.24 presents the steady-state voltages at the wind turbine. The transient voltages at the wind turbine when the capacitor is turned on at 8:00 am, when the fault occurs at 2:00 pm, and when the capacitor is turned off at 10:00 pm are shown in Figs. 5.25-5.27, respectively. Note that Fig. 5.24 is obtained from the steady-state simulation, Fig. 5.26 (time > 0) is produced by the electromechanical transient simulation, and Figs. 5.25 and 5.27 (time > 0) are the results of the electromagnetic transient simulation.

In Fig. 5.24, the steady-state voltages at the wind turbine between 12:00 am and 8:00 am, between 8:00 am and 10:00 pm, and between 10:00 pm and 12:00 am vary due to voltage drops across the lines and transformer, which are proportional to the currents flowing through them. The variations of the currents are caused by

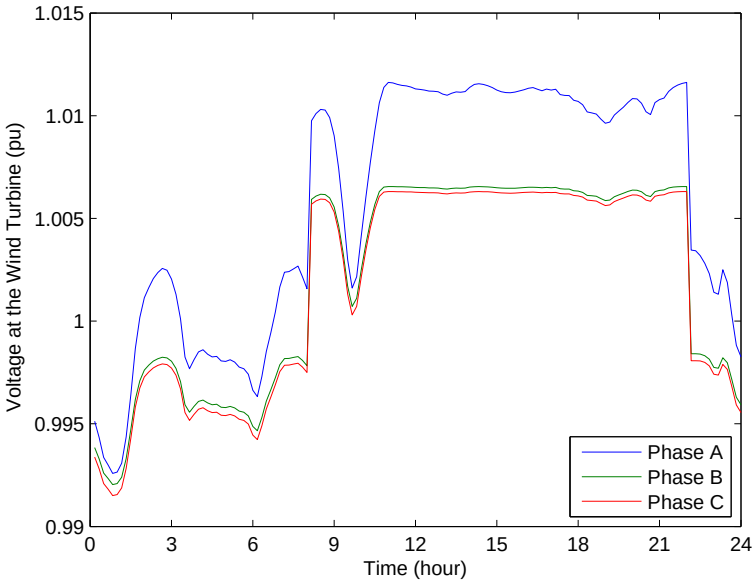

Figure 5.24: Steady-state voltages at the FSWT

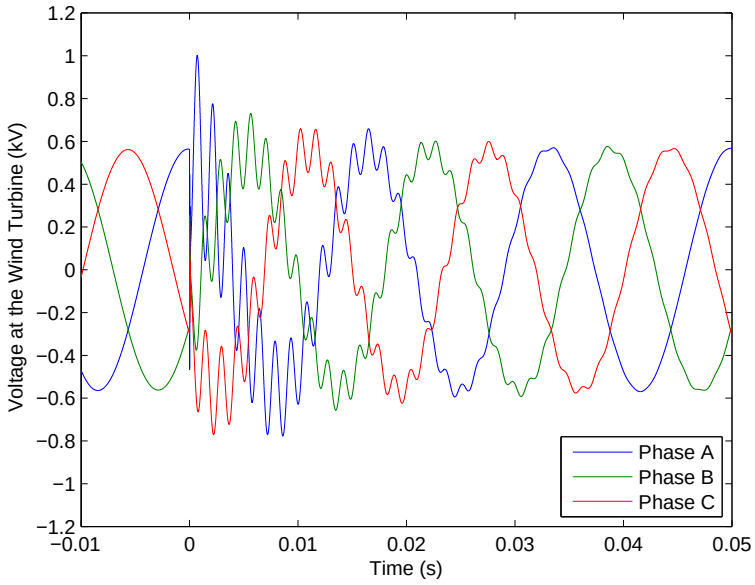

Figure 5.25: Transient voltages at the FSWT when the capacitor bank is turned on at 8:00 am

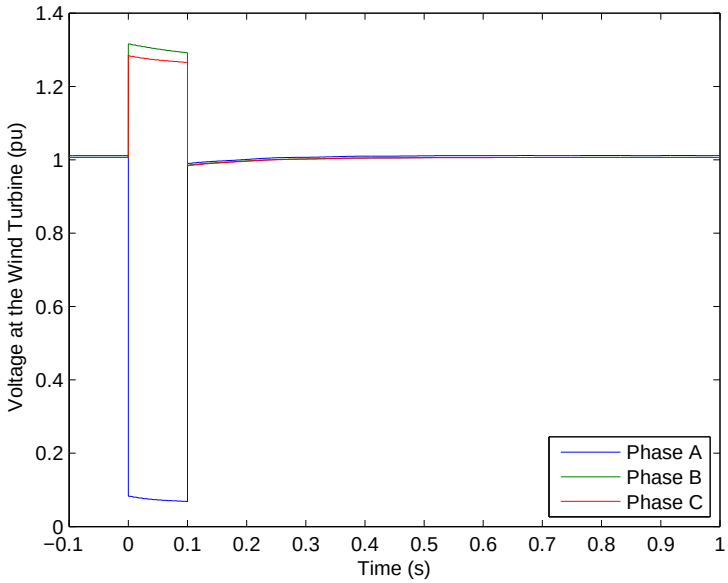

Figure 5.26: Transient voltages at the FSWT when the fault occurs at 2:00 pm

the change of the wind power. At 8:00 am, the capacitor is switched on; therefore, Phases A, B, and C voltages (steady-state) significantly increase from 1.0016, 0.9978, and 0.9975 to 1.0098, 1.0059, and 1.0057 pu, respectively. However, the capacitor is switched off at 10:00 pm, so the steady-state voltages dramatically decrease from 1.0116, 1.0066, and 1.0063 to 1.0035, 0.9984, and 0.9981 pu.

As shown in Fig. 5.25, when the capacitor bank is energized at 8:00 am, the electromagnetic transient voltage oscillation occurs because the capacitor bank briefly pulls the voltage at its location down to zero (the capacitor voltage before energizing is zero). The voltage oscillation disappears after a few cycles due to the damping in the circuit.

As can be seen from Fig. 5.26, when the single-line-to-ground fault occurs on Phase A of the high voltage side of the transformer at 2:00 pm, Phase A voltage at the wind turbine drops to 0.07 pu. However, Phases B and C voltages rise to 1.29

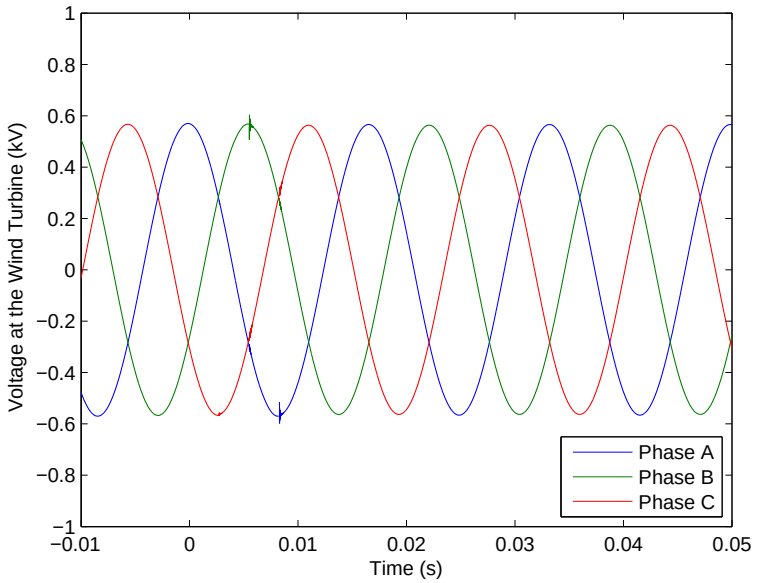

Figure 5.27: Transient voltages at the FSWT when the capacitor bank is turned off at 10:00 pm

and 1.27 pu, respectively. The voltages at the wind turbine return to their initial values when the fault clears itself.

When the capacitor bank is de-energized at 10:00 pm, the voltage magnitudes slightly decrease as shown in Fig. 5.27. There are small transients since the capacitor is not de-energized at the exact current zero-crossing.

5.4.2 Simulation of a WSWT

Two case studies for a WSWT are simulated in this section: a quasi-steady-state simulation of a WSWT and a multi-time-scale simulation of a WSWT.

Table 5.13: Quasi-steady-state results of the WSWT simulation

Wind speed (m/s)	Slip (%)	External rotor resistance (Ω)	Real power produced by the wind turbine (MW)	Reactive power produced by the wind turbine (Mvar)
6	−0.097	0	0.070	−0.258
7	−0.332	0	0.242	−0.263
8	−0.653	0	0.479	−0.277
9	−1.006	0	0.742	−0.302
10	−1.349	0	0.998	−0.336
11	−1.635	0	1.211	−0.371
12	−1.848	0	1.371	−0.401
13	−1.976	0	1.466	−0.421
14	−2.022	0	1.500	−0.428
15	−2.444	0.0013	1.500	−0.428
16	−3.895	0.0058	1.500	−0.428
17	−6.062	0.0126	1.500	−0.428
18	−8.069	0.0189	1.500	−0.428
19	−10.445	0.0263	1.500	−0.428
20	−13.185	0.0349	1.500	−0.428

5.4.2.1 Quasi-Steady-State Simulation of a WSWT

This case considers a wind turbine consisting of a WSWT operating in the four-node test circuit in Fig. 5.1 in quasi-steady-state conditions. The capacitor bank in the test circuit is offline. The wind speed varies from the cut-in speed (6 m/s) to the cut-out speed (20 m/s) with an increment of 1 m/s. The wind turbine slip, the external rotor resistance, and the real and reactive power produced by the wind turbine are shown in Table 5.13. The voltages at the wind turbine, the low voltage side of the transformer, and the high voltage side of the transformer are presented in Table 5.14.

As shown in Table 5.13, the wind turbine operates in the range where the slip is negative. The magnitude of the slip is small when the wind speed is less than the rated speed. However, the magnitude of the slip increases when the wind speed is above the rated speed. The generated real power increases when the wind speed

Table 5.14: Node voltage results of the WSWT simulation

Wind speed (m/s)	Voltage at the wind turbine (pu)			Voltage at the low voltage side of the transformer (pu)			Voltage at the high voltage side of the transformer (pu)		
	Phase A	Phase B	Phase C	Phase A	Phase B	Phase C	Phase A	Phase B	Phase C
6	0.994∠ 0.4°	0.994∠ −119.7°	0.993∠ 120.3°	0.997∠ 0.1°	0.997∠ −119.9°	0.997∠ 120.1°	1.000∠ 0.0°	1.000∠ −120.0°	1.000∠ 120.0°
7	0.996∠ 0.7°	0.996∠ −119.4°	0.995∠ 120.6°	0.998∠ 0.2°	0.998∠ −119.8°	0.998∠ 120.2°	1.000∠ 0.0°	1.000∠ −120.0°	1.000∠ 120.0°
8	1.000∠ 1.1°	0.998∠ −119.0°	0.998∠ 121.0°	0.999∠ 0.4°	0.999∠ −119.6°	0.999∠ 120.4°	1.000∠ 0.1°	1.000∠ −120.0°	1.000∠ 120.1°
9	1.003∠ 1.5°	1.001∠ −118.6°	1.001∠ 121.5°	1.001∠ 0.6°	1.001∠ −119.4°	1.001∠ 120.6°	1.000∠ 0.1°	1.000∠ −119.9°	1.000∠ 120.1°
10	1.006∠ 2.0°	1.003∠ −118.2°	1.003∠ 121.9°	1.001∠ 0.8°	1.002∠ −119.2°	1.002∠ 120.8°	1.000∠ 0.1°	1.000∠ −119.9°	1.000∠ 120.1°
11	1.008∠ 2.3°	1.004∠ −117.8°	1.004∠ 122.3°	1.002∠ 0.9°	1.002∠ −119.1°	1.002∠ 120.9°	1.000∠ 0.1°	1.000∠ −119.9°	1.000∠ 120.1°
12	1.010∠ 2.6°	1.005∠ −117.5°	1.005∠ 122.6°	1.003∠ 1.0°	1.003∠ −119.0°	1.003∠ 121.0°	1.001∠ 0.1°	1.000∠ −119.9°	1.000∠ 120.1°
13	1.011∠ 2.8°	1.006∠ −117.4°	1.006∠ 122.7°	1.003∠ 1.1°	1.003∠ −118.9°	1.003∠ 121.1°	1.001∠ 0.2°	1.000∠ −119.9°	1.000∠ 120.1°
14	1.011∠ 2.9°	1.006∠ −117.3°	1.006∠ 122.8°	1.003∠ 1.1°	1.003∠ −118.9°	1.003∠ 121.1°	1.001∠ 0.2°	1.000∠ −119.9°	1.000∠ 120.2°
15	1.011∠ 2.9°	1.006∠ −117.3°	1.006∠ 122.8°	1.003∠ 1.1°	1.003∠ −118.9°	1.003∠ 121.1°	1.001∠ 0.2°	1.000∠ −119.9°	1.000∠ 120.2°
16	1.011∠ 2.9°	1.006∠ −117.3°	1.006∠ 122.8°	1.003∠ 1.1°	1.003∠ −118.9°	1.003∠ 121.1°	1.001∠ 0.2°	1.000∠ −119.9°	1.000∠ 120.2°
17	1.011∠ 2.9°	1.006∠ −117.3°	1.006∠ 122.8°	1.003∠ 1.1°	1.003∠ −118.9°	1.003∠ 121.1°	1.001∠ 0.2°	1.000∠ −119.9°	1.000∠ 120.2°
18	1.011∠ 2.9°	1.006∠ −117.3°	1.006∠ 122.8°	1.003∠ 1.1°	1.003∠ −118.9°	1.003∠ 121.1°	1.001∠ 0.2°	1.000∠ −119.9°	1.000∠ 120.2°
19	1.011∠ 2.9°	1.006∠ −117.3°	1.006∠ 122.8°	1.003∠ 1.1°	1.003∠ −118.9°	1.003∠ 121.1°	1.001∠ 0.2°	1.000∠ −119.9°	1.000∠ 120.2°
20	1.011∠ 2.9°	1.006∠ −117.3°	1.006∠ 122.8°	1.003∠ 1.1°	1.003∠ −118.9°	1.003∠ 121.1°	1.001∠ 0.2°	1.000∠ −119.9°	1.000∠ 120.2°

increases from the cut-in to the rated speed, but the real power remains at the rated power when the wind speed is higher than the rated speed because of the power control. Additionally, the wind turbine consumes reactive power for all wind speeds. From Table 5.14, the steady-state voltages are in an acceptable range (0.95-1.05 pu). Therefore, it can be concluded that the system operates in stable conditions.

5.4.2.2 Multi-Time-Scale Simulation of a WSWT

This case considers a wind turbine consisting of a WSWT in quasi-steady-state, electromechanical transient, and electromagnetic transient conditions. The simulation scenario is similar to the scenario for the multi-time-scale simulation of an FSWT. The steady-state voltages at the wind turbine are shown in Fig. 5.28. Figs. 5.29-5.31 describe the transient voltages at the wind turbine when the capacitor is turned on (8:00 am), when the fault occurs (2:00 pm), and when the capacitor is turned off (10:00 pm), respectively. Note that the steady-state model is employed when wind speed changes (Fig. 5.28), the electromechanical transient model is used when the fault occurs (Fig. 5.30), and the electromagnetic transient model is required when the capacitor switches (Figs. 5.29 and 5.31).

The steady-state voltages at the wind turbine between 12:00 am and 8:00 am, between 8:00 am and 10:00 pm, and between 10:00 pm and 12:00 am (Fig. 5.28) vary due to the change of the wind power. From 11:00 am to 10:00 pm, wind speed is above the rated speed, so the wind turbine produces rated power output. Therefore, Phases A, B, and C voltages at the wind turbine are flat at 1.0142, 1.0091, and 1.0095 pu, respectively. At 8:00 am, Phases A, B, and C voltages rise from 1.0073, 1.0037, and 1.0038 to 1.0155, 1.0118, and 1.0120 pu because the capacitor is turned on. However, when the capacitor is turned off (at 10:00 pm), the voltages drop from 1.0190, 1.0141,

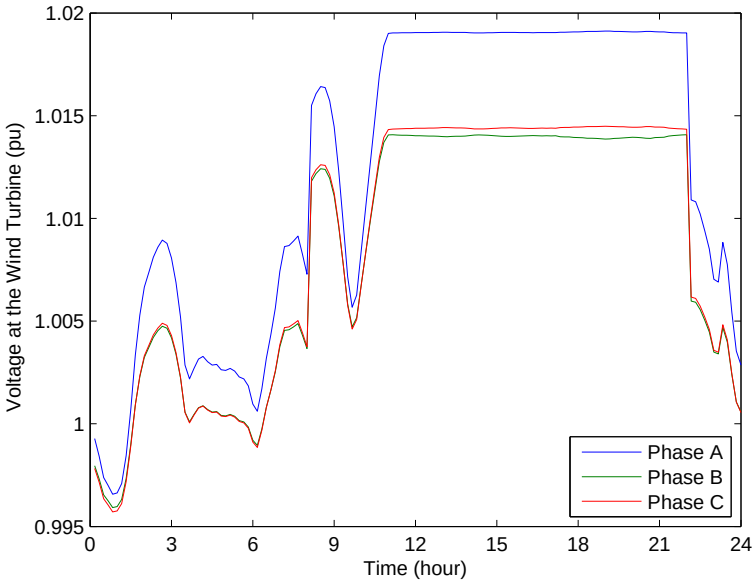

Figure 5.28: Steady-state voltages at the WSWT

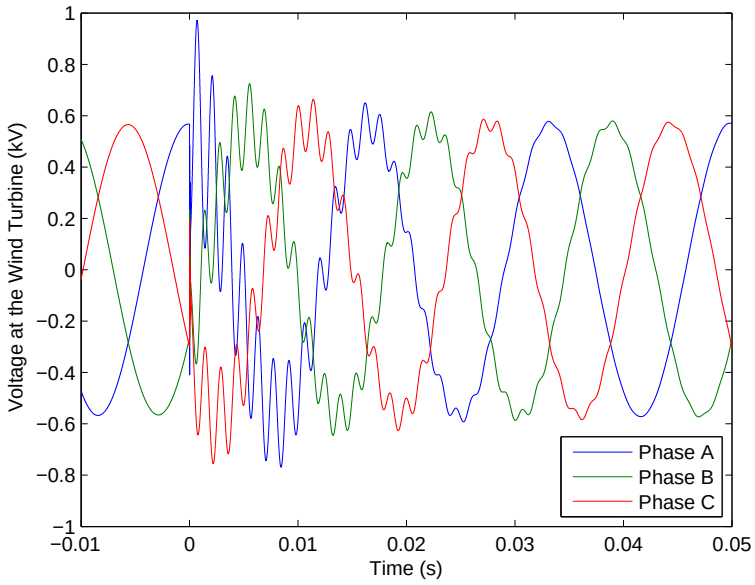

Figure 5.29: Transient voltages at the WSWT when the capacitor bank is turned on at 8:00 am

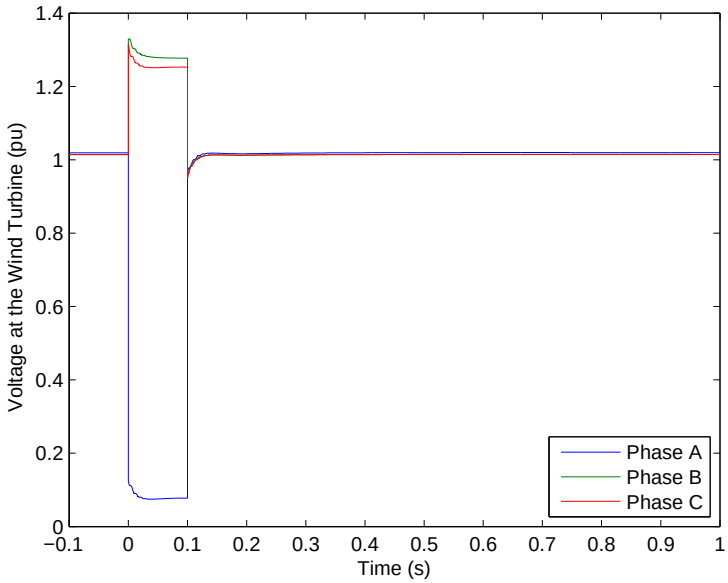

Figure 5.30: Transient voltages at the WSWT when the fault occurs at 2:00 pm

and 1.0143 to 1.0109, 1.0060, and 1.0062 pu.

When the capacitor bank is energized (at 8:00 am), the electromagnetic transient voltage oscillation occurs as presented in Fig. 5.29. The voltage oscillation disappears after a few cycles.

When the fault occurs at 2:00 pm, Phase A voltage at the wind turbine suddenly drops to 0.08 pu (Fig. 5.30). However, Phases B and C voltages rise to 1.28 and 1.25 pu. The voltages return to their initial values when the fault is cleared.

At 10:00 pm, the capacitor bank is de-energized, so the voltage magnitudes slightly decrease (Fig. 5.31).

5.4.3 Simulation of DFIG and Full Converter Wind Turbines

Two case studies for DFIG and full converter wind turbines are simulated in this section: a quasi-steady-state simulation of DFIG and full converter wind turbines,

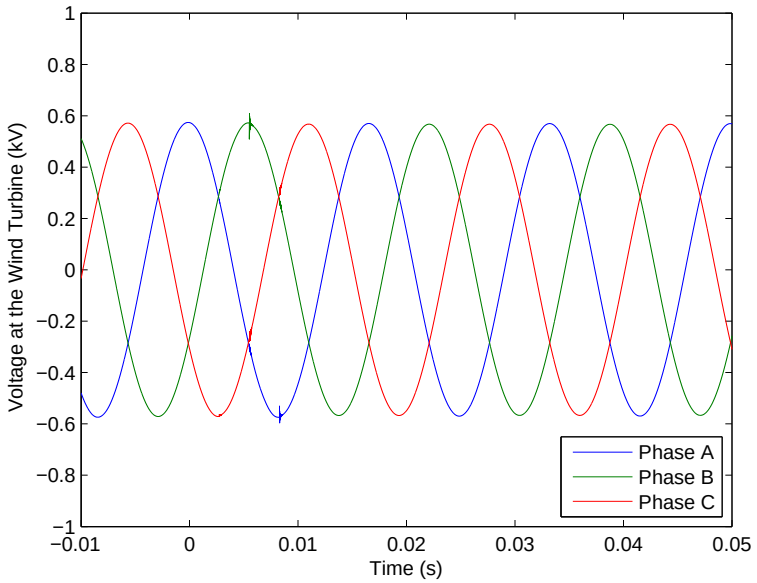

Figure 5.31: Transient voltages at the WSWT when the capacitor bank is turned off at 10:00 pm

and a multi-time-scale simulation of DFIG and full converter wind turbines.

5.4.3.1 Quasi-Steady-State Simulation of DFIG and Full Converter Wind Turbines

This case considers a wind turbine consisting of a DFIG and full converter wind turbines operating in the four-node test circuit in Fig. 5.1 in quasi-steady-state conditions. The capacitor bank in the test circuit is offline. The wind speed varies from the cut-in speed (6 m/s) to the cut-out speed (20 m/s) with an increment of 1 m/s. The real and reactive power produced by the wind turbine are shown in Table 5.15. The voltages at the wind turbine, the low voltage side of the transformer, and the high voltage side of the transformer are presented in Table 5.16.

As shown in Table 5.15, the generated real power increases when the wind speed increases from the cut-in to the rated speed, but the real power remains at the

Table 5.15: Quasi-steady-state results of the DFIG and full converter wind turbine simulation

Wind speed (m/s)	Real power produced by the wind turbine (MW)	Reactive power produced by the wind turbine (Mvar)
6	0.255	0
7	0.405	0
8	0.605	0
9	0.862	0
10	1.182	0
11	1.500	0
12	1.500	0
13	1.500	0
14	1.500	0
15	1.500	0
16	1.500	0
17	1.500	0
18	1.500	0
19	1.500	0
20	1.500	0

rated power when the wind speed is higher than the rated speed because of the real power control. Additionally, the wind turbine does not produce or consume reactive power (unity power factor) for all wind speeds due to the reactive power control. From Table 5.16, the steady-state voltages are in an acceptable range (0.95-1.05 pu). Therefore, it can be concluded that the system operates in stable conditions.

5.4.3.2 Multi-Time-Scale Simulation of DFIG and Full Converter Wind Turbines

This case considers a wind turbine consisting of DFIG and full converter wind turbines in quasi-steady-state, electromechanical transient, and electromagnetic transient conditions. The simulation scenario is similar to the scenario for the multi-time-scale simulation of an FSWT and a WSWT. Fig. 5.32 illustrates the steady-state voltages at the wind turbine for a 24-hour period. Figs. 5.33-5.35 present the tran-

Table 5.16: Node voltage results of the DFIG and full converter wind turbine simulation

Wind speed (m/s)	Voltage at the wind turbine (pu)			Voltage at the low voltage side of the transformer (pu)			Voltage at the high voltage side of the transformer (pu)		
	Phase A	Phase B	Phase C	Phase A	Phase B	Phase C	Phase A	Phase B	Phase C
6	1.004∠ 0.4°	1.003∠ −119.6°	1.003∠ 120.4°	1.002∠ 0.2°	1.001∠ −119.8°	1.001∠ 120.2°	1.000∠ 0.0°	1.000∠ −120.0°	1.000∠ 120.0°
7	1.007∠ 0.7°	1.005∠ −119.4°	1.005∠ 120.7°	1.002∠ 0.3°	1.002∠ −119.7°	1.002∠ 120.3°	1.000∠ 0.0°	1.000∠ −120.0°	1.000∠ 120.0°
8	1.010∠ 1.0°	1.007∠ −119.1°	1.008∠ 121.0°	1.003∠ 0.4°	1.003∠ −119.6°	1.003∠ 120.4°	1.001∠ 0.1°	1.000∠ −120.0°	1.000∠ 120.1°
9	1.014∠ 1.4°	1.010∠ −118.7°	1.011∠ 121.5°	1.005∠ 0.6°	1.005∠ −119.4°	1.005∠ 120.6°	1.001∠ 0.1°	1.000∠ −119.9°	1.001∠ 120.1°
10	1.019∠ 1.9°	1.014∠ −118.2°	1.015∠ 122.0°	1.007∠ 0.8°	1.006∠ −119.2°	1.006∠ 120.8°	1.001∠ 0.1°	1.001∠ −119.9°	1.001∠ 120.1°
11	1.024∠ 2.4°	1.017∠ −117.7°	1.084∠ 122.5°	1.008∠ 1.0°	1.008∠ −119.0°	1.008∠ 121.0°	1.001∠ 0.1°	1.001∠ −119.9°	1.001∠ 120.1°
12	1.024∠ 2.4°	1.017∠ −117.7°	1.084∠ 122.5°	1.008∠ 1.0°	1.008∠ −119.0°	1.008∠ 121.0°	1.001∠ 0.1°	1.001∠ −119.9°	1.001∠ 120.1°
13	1.024∠ 2.4°	1.017∠ −117.7°	1.084∠ 122.5°	1.008∠ 1.0°	1.008∠ −119.0°	1.008∠ 121.0°	1.001∠ 0.1°	1.001∠ −119.9°	1.001∠ 120.1°
14	1.024∠ 2.4°	1.017∠ −117.7°	1.084∠ 122.5°	1.008∠ 1.0°	1.008∠ −119.0°	1.008∠ 121.0°	1.001∠ 0.1°	1.001∠ −119.9°	1.001∠ 120.1°
15	1.024∠ 2.4°	1.017∠ −117.7°	1.084∠ 122.5°	1.008∠ 1.0°	1.008∠ −119.0°	1.008∠ 121.0°	1.001∠ 0.1°	1.001∠ −119.9°	1.001∠ 120.1°
16	1.024∠ 2.4°	1.017∠ −117.7°	1.084∠ 122.5°	1.008∠ 1.0°	1.008∠ −119.0°	1.008∠ 121.0°	1.001∠ 0.1°	1.001∠ −119.9°	1.001∠ 120.1°
17	1.024∠ 2.4°	1.017∠ −117.7°	1.084∠ 122.5°	1.008∠ 1.0°	1.008∠ −119.0°	1.008∠ 121.0°	1.001∠ 0.1°	1.001∠ −119.9°	1.001∠ 120.1°
18	1.024∠ 2.4°	1.017∠ −117.7°	1.084∠ 122.5°	1.008∠ 1.0°	1.008∠ −119.0°	1.008∠ 121.0°	1.001∠ 0.1°	1.001∠ −119.9°	1.001∠ 120.1°
19	1.024∠ 2.4°	1.017∠ −117.7°	1.084∠ 122.5°	1.008∠ 1.0°	1.008∠ −119.0°	1.008∠ 121.0°	1.001∠ 0.1°	1.001∠ −119.9°	1.001∠ 120.1°
20	1.024∠ 2.4°	1.017∠ −117.7°	1.084∠ 122.5°	1.008∠ 1.0°	1.008∠ −119.0°	1.008∠ 121.0°	1.001∠ 0.1°	1.001∠ −119.9°	1.001∠ 120.1°

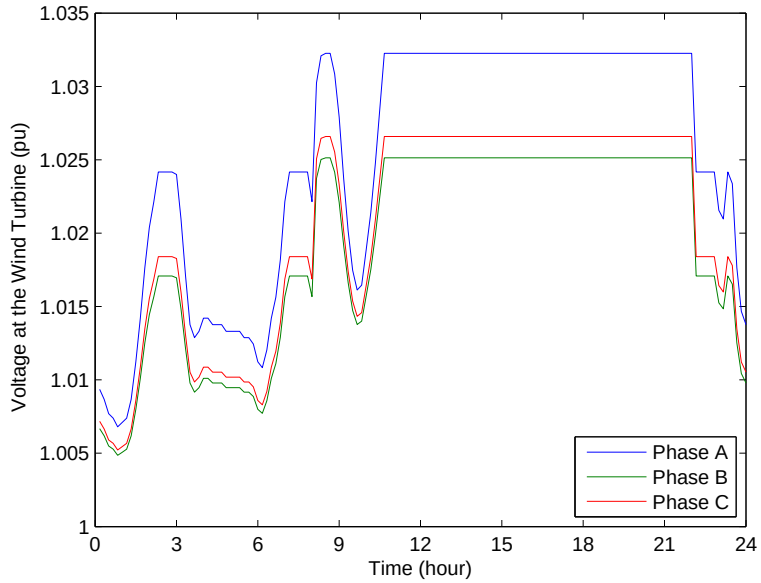

Figure 5.32: Steady-state voltages at the wind turbine

sient voltages at the wind turbine when the capacitor bank is switched on, when the fault occurs, and when the capacitor bank is switched off, respectively.

The change of wind speed causes the variation of steady-state voltages at the wind turbine between 12:00 am and 8:00 am, between 8:00 am and 10:00 pm, and between 10:00 pm and 12:00 am as presented in Fig. 5.32. Phases A, B, and C voltages at the wind turbine are flat at 1.0322, 1.0251, and 1.0266 pu between 11:00 am and 10:00 pm because the wind turbine produces rated power output. Phases A, B, and C voltages rise from 1.0221, 1.0157, and 1.0169 to 1.0302, 1.0237, and 1.0251 pu at 8:00 am because the capacitor is turned on. However, the voltages drop from 1.0322, 1.0251, and 1.0266 to 1.0242, 1.0171, and 1.0184 pu at 10:00 pm because the capacitor is turned off.

Fig. 5.33 illustrates the electromagnetic transient oscillation due to the capacitor being energized. The voltage magnitudes slightly rise after the capacitor is

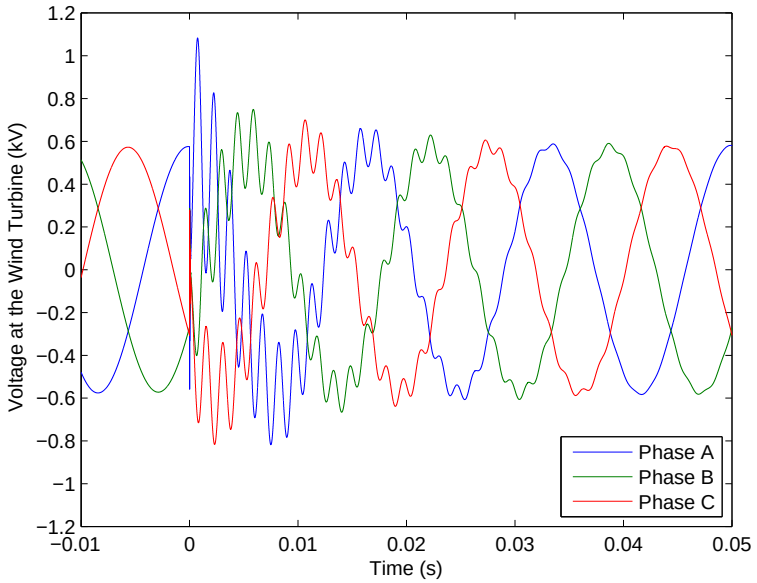

Figure 5.33: Transient voltages at the wind turbine when the capacitor bank is turned on at 8:00 am

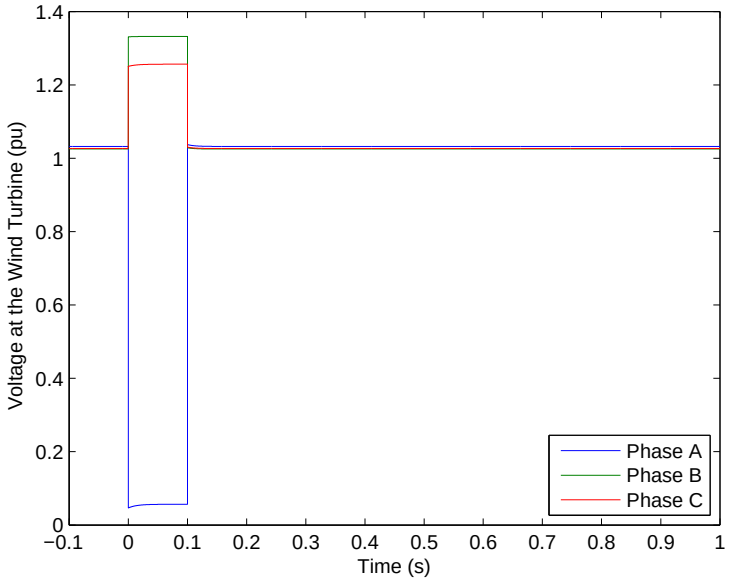

Figure 5.34: Transient voltages at the wind turbine when the fault occurs at 2:00 pm

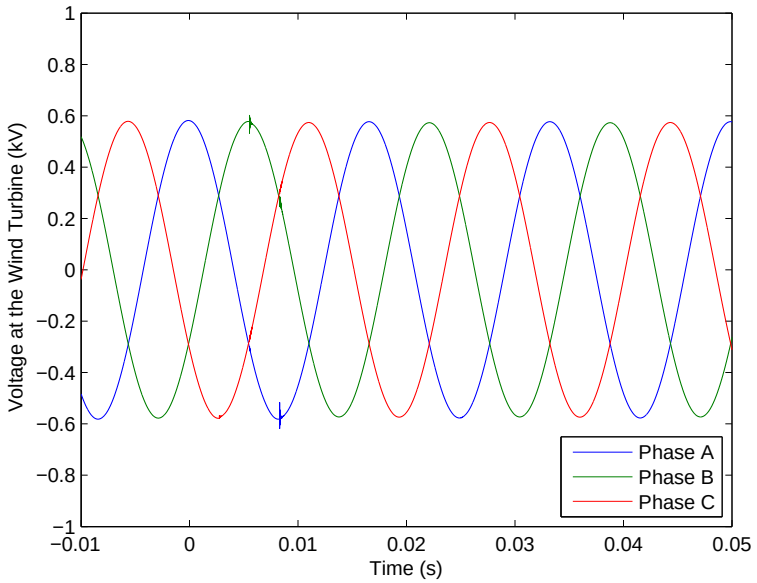

Figure 5.35: Transient voltages at the wind turbine when the capacitor bank is turned off at 10:00 pm

switched on.

Fig. 5.34 shows that Phase A voltage at the wind turbine drops to 0.05 pu when the single-line-to-ground fault occurs on Phase A. However, Phases B and C voltages at the wind turbine rise to 1.33 and 1.25 pu, respectively. After the fault is cleared, the voltages return to their initial values.

Because the capacitor is not de-energized at the exact current zero-crossing, small transients occur at the capacitor switching as illustrated in Fig. 5.35. The voltage magnitudes slightly drop after the capacitor is switched off.

5.4.4 Simulation of a PV

Two case studies for a PV are simulated in this section: a quasi-steady-state simulation of a PV and a multi-time-scale simulation of a PV.

Table 5.17: Quasi-steady-state results of the PV simulation

Solar irradiance (pu)	Real power produced by the PV (kW)	Reactive power produced by the PV (kvar)
0	0	0
0.1	0.500	0.164
0.2	1.000	0.329
0.3	1.500	0.493
0.4	2.000	0.657
0.5	2.500	0.822
0.6	3.000	0.986
0.7	3.500	1.150
0.8	4.000	1.315
0.9	4.500	1.479
1.0	5.000	1.643

5.4.4.1 Quasi-Steady-State Simulation of a PV

This case considers a PV operating in the three-node test circuit in Fig. 5.2 in quasi-steady-state conditions. The capacitor bank in the test circuit is online. The solar irradiance varies from 0 pu to 1 pu with an increment of 0.1 pu. The real and reactive power produced by the PV are shown in Table 5.17. The voltages at the PV and the high voltage side of the transformer are presented in Table 5.18.

As shown in Table 5.17, the generated real power is proportional to the solar irradiance. The PV produces the rated power when the irradiance is 1 pu. Additionally, the PV also produces reactive power according to the reactive power control. Note that the power factor of the PV is controlled to 0.95. From Table 5.18, the steady-state voltages are in an acceptable range (0.95-1.05 pu). Therefore, it can be concluded that the system operates in stable conditions.

Table 5.18: Node voltage results of the PV simulation

Solar irradiance (pu)	Voltage at the PV Bus (pu)			Voltage at the high voltage side of the transformer (pu)		
	Phase A	Phase B	Phase C	Phase A	Phase B	Phase C
0	0.979∠ −0.3°	0.977∠ 179.8°	0.968∠ 89.6°	1.001∠ −0.2°	1.003∠ −120.1°	1.003∠ 119.9°
0.1	0.980∠ −0.2°	0.978∠ 179.8°	0.968∠ 89.6°	1.001∠ −0.2°	1.003∠ −120.1°	1.003∠ 119.9°
0.2	0.980∠ −0.2°	0.978∠ 179.8°	0.968∠ 89.6°	1.001∠ −0.2°	1.003∠ −120.1°	1.003∠ 119.9°
0.3	0.981∠ −0.2°	0.979∠ 179.8°	0.968∠ 89.6°	1.002∠ −0.2°	1.003∠ −120.1°	1.003∠ 119.9°
0.4	0.981∠ −0.2°	0.979∠ 179.9°	0.968∠ 89.6°	1.002∠ −0.2°	1.003∠ −120.1°	1.003∠ 119.9°
0.5	0.982∠ −0.2°	0.980∠ 179.9°	0.968∠ 89.6°	1.002∠ −0.2°	1.003∠ −120.1°	1.003∠ 119.9°
0.6	0.982∠ −0.2°	0.980∠ 179.9°	0.968∠ 89.6°	1.002∠ −0.2°	1.003∠ −120.1°	1.003∠ 119.9°
0.7	0.983∠ −0.2°	0.981∠ 179.9°	0.968∠ 89.6°	1.002∠ −0.2°	1.003∠ −120.1°	1.003∠ 119.9°
0.8	0.983∠ −0.2°	0.982∠ 179.9°	0.968∠ 89.6°	1.002∠ −0.2°	1.003∠ −120.1°	1.003∠ 119.9°
0.9	0.984∠ −0.2°	0.982∠ 179.9°	0.968∠ 89.6°	1.002∠ −0.2°	1.003∠ −120.1°	1.003∠ 119.9°
1.0	0.984∠ −0.2°	0.983∠ 179.9°	0.968∠ 89.6°	1.002∠ −0.2°	1.003∠ −120.1°	1.003∠ 119.9°

5.4.4.2 Multi-Time-Scale Simulation of a PV

This case considers a PV in quasi-steady-state, electromechanical transient, and electromagnetic transient conditions. The simulation is performed for a 24-hour period. During this simulation period, solar irradiance changes every one second. The one-second resolution solar irradiance data obtained from EPRI [84] are shown in Fig. 5.36. When the simulation starts at 12:00 am, the capacitor bank is in service. The capacitor bank is switched off at 8:00 am and switched on again at 4:00 pm. A temporary bolted single-line-to-ground fault occurs on Phase A of the high voltage side of the transformer at 12:00 pm. The fault clears itself in 0.1 seconds. The steady-

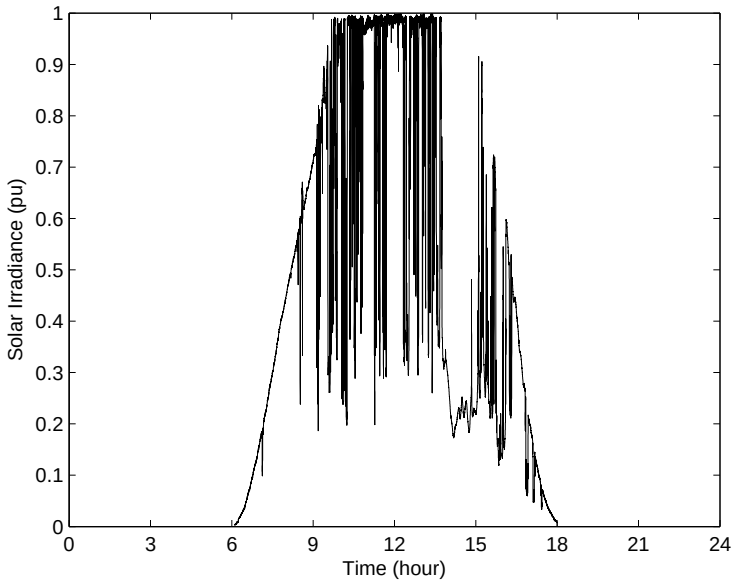

Figure 5.36: Solar irradiance for the multi-time-scale simulation

state voltages at the PV for a 24-hour period is presented in Fig. 5.37. The transient voltages at the PV when the capacitor is switched off, when the fault occurs, and when the capacitor is switched on are illustrated in Figs. 5.38-5.40, respectively.

The variation of the steady-state voltages at the PV between 6:00 am and 8:00 am, between 8:00 am and 4:00 pm, and between 4:00 pm and 6:00 am (Fig. 5.37) is caused by the change of the solar irradiance. From 12:00 am to 6:00 am and from 6:00 pm to 12:00 am, the solar irradiance is zero, so Phases A, B, and C voltages at the PV are flat at 0.9790, 0.9773, and 0.9681 pu, respectively. When the capacitor is turned off, Phases A, B, and C voltages decrease from 0.9814, 0.9797, and 0.9681 to 0.9785, 0.9767, and 0.9651 pu. However, when the capacitor is turned on, the voltages increase from 0.9774, 0.9756, and 0.9651 to 0.9805, 0.9787, and 0.9681 pu.

According to Fig. 5.38, after the capacitor bank is de-energized, the voltage magnitudes slightly drop.

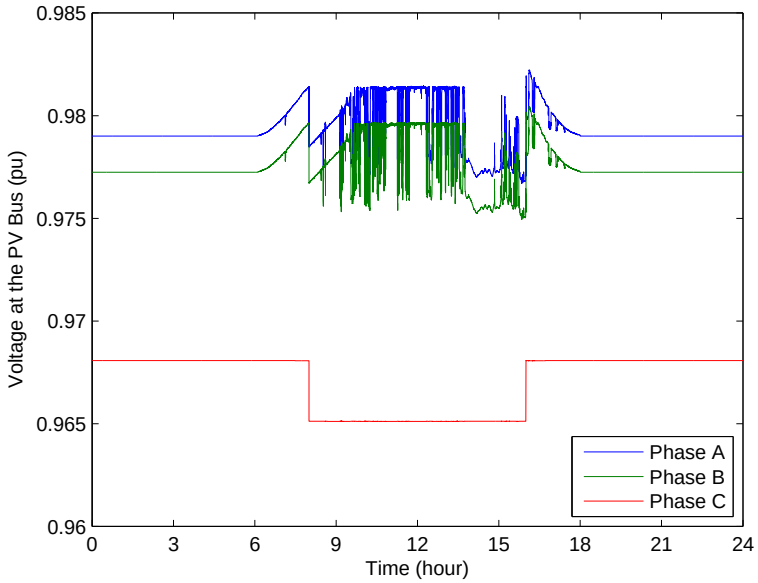

Figure 5.37: Steady-state voltages at the PV

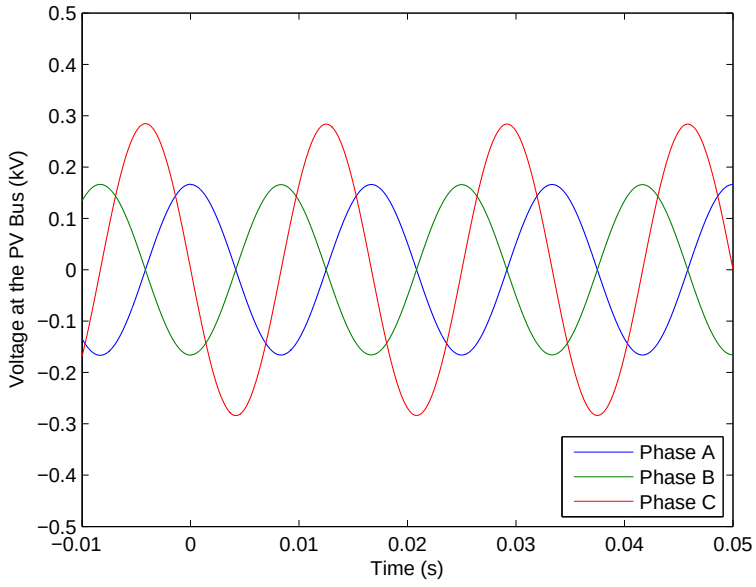

Figure 5.38: Transient voltages at the PV when the capacitor bank is turned off at 8:00 am

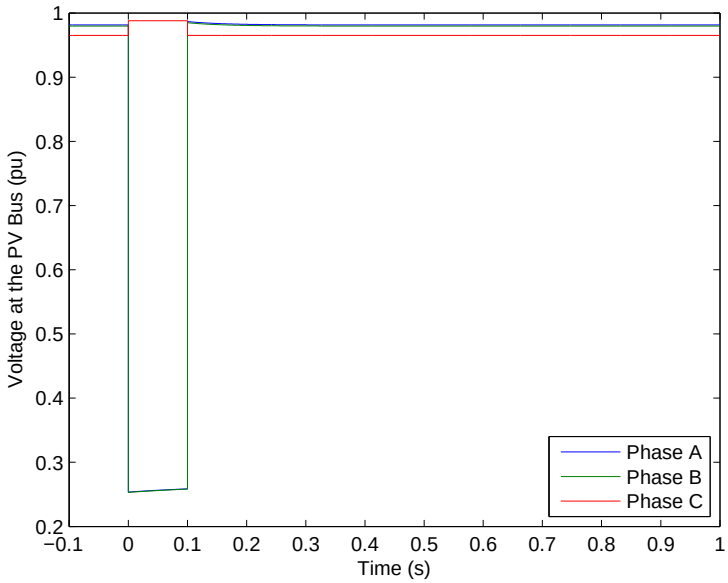

Figure 5.39: Transient voltages at the PV when the fault occurs at 12:00 pm

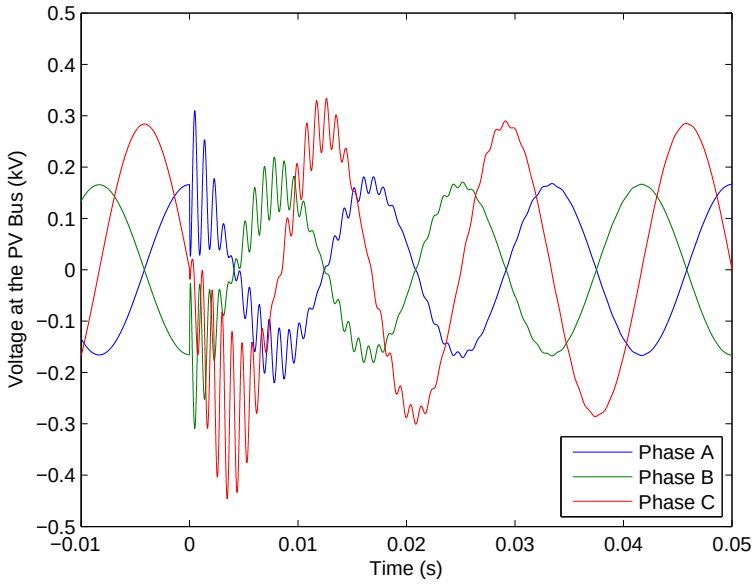

Figure 5.40: Transient voltages at the PV when the capacitor bank is turned on at 4:00 pm

When the single-line-to-ground fault occurs on Phase A of the high voltage side of the transformer, Phases A and B voltages at the PV suddenly drops to 0.26 pu as illustrated in Fig. 5.39. However, Phase C voltage at the PV slightly rises to 0.99 pu. The voltages return to their initial values after the fault is cleared.

After the capacitor bank is energized, the electromagnetic transient voltage oscillation occurs as described in Fig. 5.40. The voltage oscillation disappears after a few cycles. The voltage magnitudes slightly increase after the capacitor is turned on.

Chapter 6

Conclusion

This research develops an integrated multi-time-scale simulation tool for distribution circuits designed specifically for applications in wind turbine and PV analysis. The proposed multi-time-scale simulation tool developed in MATLAB^{TM} consists of steady-state, electromechanical transient, and electromagnetic transient models for analyzing quasi-steady-state, electromechanical transient, and electromagnetic transient power system phenomena. The novel contribution of this proposed tool is the ability to switch from one single-time scale model to another single-time scale model when power system phenomena with different time scales occur. Therefore, this tool is capable of performing a long-term simulation involving power system phenomena spreading across time scales. Because the proposed tool employs models of distribution circuits with all three phases represented, the tool is able to analyze distribution circuits operating in unbalanced conditions due to single-phase loads and single-phase circuits in the systems.

The proposed multi-time-scale simulation tool includes voltage sources, lines, transformers, loads, capacitor banks, FSWTs, WSWTs, DFIG wind turbines, full converter wind turbines, and PVs. These circuit components can be classified into two types. The first type is distribution network components (lines, transformers, capacitor banks, and constant impedance loads). These equipment are represented by a nodal admittance matrix. The second type is wind turbines and PVs. These equipment are represented by voltage or current sources connected to a distribution

Table 6.1: Summary of distribution network, wind turbine, and PV models

Model		Electromagnetic	Electromechanical	Steady-state
Distribution network		Complete	Steady-state	Steady-state
Wind turbine	Aerodynamic	Steady-state	Steady-state	Steady-state
	Mechanical	Constant speed	Two-mass	Steady-state
	SCIG, WRIG	Complete	Reduced	Steady-state
	PMSG	Complete	Complete	Steady-state
	Converter	Current source	Current source	Constant power
PV	PV array	Steady-state	Steady-state	Steady-state
	Inverter	Current source	Current source	Constant power

network. The models of distribution networks, wind turbines, and PVs are summarized in Table 6.1.

For distribution networks (feeders, transformers, capacitor banks, and constant impedance loads), the electromagnetic transient models are the complete model containing dynamics of inductors and capacitors in power systems. However, the electromechanical transient and steady-state models of distribution networks are identical because distribution networks do not have any state variables related to electromechanical transients.

Wind turbine models consist of four major components, i.e., aerodynamic, mechanical, generator, and converter components. The models for the aerodynamic system in electromagnetic transient, electromechanical transient, and steady-state conditions are the same because the aerodynamic system does not have any state variables. For the mechanical system, the electromagnetic transient models are simply constant speed model because the simulation time is very short, so the generator speed does not change. The electromechanical transient models employ a two-mass model. The steady-state models are models neglecting all dynamics by setting all derivative terms to zero. The electromagnetic transient models of the wind generator (SCIG, WRIG, and PMSG) employ a complete model. The electromechanical

transient models of the SCIG and WRIG employ a reduced order dynamic model disregarding the transients in the stator. However, the models of the PMSG in electromechanical transient conditions are the same as the models in electromagnetic transient conditions because the electromagnetic transient models do not include the dynamics of the damper windings. The wind generator (SCIG, WRIG, and PMSG) models in steady-state conditions are the models with all derivative terms neglected. The converters of the wind turbines are represented by current sources for electromagnetic and electromechanical transient simulation. However, the converters of the wind turbines are modeled by a constant power load model in a steady-state condition.

PV models consist of two components, i.e., PV array and inverter. The PV array models for electromagnetic transient, electromechanical transient, and steady-state simulations are identical because the model of PV arrays no dynamics. The PV inverters are represented by current sources for electromagnetic and electromechanical transient simulations. However, the PV inverters are modeled by a constant power load model in a steady-state condition.

For a quasi-steady-state simulation, the wind turbine and PV models are connected to the distribution network models by using the fixed-point iteration method. The wind turbine and PV models obtain the terminal voltages from the distribution network model and calculate the output currents. Then, the currents are passed to the distribution network model to calculate new terminal voltages from the distribution network equation. The calculation process is repeated until the wind turbine and PV voltages and currents converge.

For an electromechanical transient simulation, the wind turbine and PV models consist of differential and algebraic equations. The differential equations are solved by the Runge-Kutta method, the linear algebraic equations are combined with the

nodal admittance equation of the distribution network, and the nonlinear algebraic equations are solved by fixed-point iteration.

For an electromagnetic transient simulation, the differential equations of the wind turbine and PV models are integrated via trapezoidal method and converted to algebraic equations. The linear algebraic equations obtained from the integration are combined with the nodal admittance equation of the distribution network, and the nonlinear algebraic equations resulting from the integration are solved by fixed-point iteration.

Currently, the proposed tool does not have the ability to detect the circuit conditions and select which single-time-scale model to use in the multi-time-scale simulation, when to use each single-time-scale model, and when to switch to another single-time-scale model. Therefore, the single-time-scale models are pre-selected according to the disturbances in the test circuit before the simulation starts. The simulation is performed by the steady-state model when quasi-steady-state disturbances such as wind, solar, and load variations occur. The simulation switches to the electromechanical transient model when electromechanical transient disturbances such as short-circuit faults occur. After the transient dies down and the circuit reaches a steady-state condition, the simulation switches back to the steady-state model. When electromagnetic transient disturbances such as capacitor switching and lightning strikes occur, the simulation switches to the electromagnetic transient model. As soon as the simulation reaches a steady-state condition, the steady-state model is employed again.

In order to smoothly switch between two single-time-scale models, the energy stored in each storage element in both models must be the same, so the voltages, currents, torques, and rotational speeds of every elements must be the same before and after switching between the models. As a result, when the simulation switches

between the steady-state model and the electromechanical or electromagnetic transient models, the electromechanical or electromagnetic transient models must rest in a steady-state condition with no existing electromechanical or electromagnetic transient dynamics.

The test circuit used to demonstrate the multi-time-scale simulation is modified from the IEEE four-node test feeder. The simulations are performed for each type of wind turbine and PV in MATLAB^{TM}. The simulation results show that the proposed multi-time-scale simulation tool can be used to analyze long-term power system phenomena spreading across time scales. The proposed tool is verified by comparing the results with those obtained from single-time-scale models developed in OpenDSS^{TM} and PSCAD/EMTDC^{TM}. Applications of the multi-time-scale simulation tool in wind and solar power integration include analysis and control of voltage regulation due to wind speed, solar irradiance, and load variation, determining the maximum penetration of wind turbines and PVs, and determining the size of required energy storage systems for peak load shaving and power variability control.

Bibliography

[1] M. Thomson and D. G. Infield, "Impact of widespread photovoltaics generation on distribution systems," *IET Renewable Power Generation*, vol. 1, no. 1, pp. 33–40, March 2007.

[2] J. Aramizu and J. C. M. Vieira, "Analysis of PV generation impacts on voltage imbalance and on voltage regulation in distribution networks," in *Proceedings of 2013 IEEE Power and Energy Society General Meeting*, Vancouver, BC, July 2013, pp. 1–5.

[3] L. Bittencourt, A. M. Schetinger, B. S. M. C. Borba, D. H. N. Dias, and R. S. Maciel, "Impact of photovoltaic integration on voltage variation of brazilian secondary network distribution system," in *Proceedings of 2015 International Conference on Renewable Energy Research and Applications*, Palermo, November 2015, pp. 134–138.

[4] D. Cheng, B. A. Mather, R. Seguin, J. Hambrick, and R. P. Broadwater, "Photovoltaic (PV) impact assessment for very high penetration levels," *IEEE Journal of Photovoltaics*, vol. 6, no. 1, pp. 295–300, January 2016.

[5] R. C. Dugan, M. F. McGranaghan, S. Santoso, and H. W. Beaty, *Electrical Power Systems Quality*, 3rd ed. New York: McGraw-Hill, 2012.

[6] Z. Lubosny, *Wind Turbine Operation in Electric Power Systems*. Berlin: Springer-Verlag, 2003.

[7] A. Woyte, V. Van Thong, R. Belmans, and J. Nijs, "Voltage fluctuations on distribution level introduced by photovoltaic systems," *IEEE Transactions on Energy Conversion*, vol. 21, no. 1, pp. 202–209, March 2006.

[8] L. Meegahapola, B. Fox, and D. Flynn, "Flicker mitigation strategy for DFIGs during variable wind conditions," in *Proceedings of 2010 IEEE Power and Energy Society General Meeting*, Minneapolis, MN, July 2010, pp. 1–8.

[9] Z. Saad-Saoud and N. Jenkins, "Models for predicting flicker induced by large wind turbines," *IEEE Transactions on Energy Conversion*, vol. 14, no. 3, pp. 743–748, September 1999.

[10] L. M. Cipcigan and P. C. Taylor, "Investigation of the reverse power flow requirements of high penetrations of small-scale embedded generation," *IET Renewable Power Generation*, vol. 1, no. 3, pp. 160–166, September 2007.

[11] D. F. Howard, T. G. Habetler, and R. G. Harley, "Improved sequence network model of wind turbine generators for short-circuit studies," *IEEE Transactions on Energy Conversion*, vol. 27, no. 4, pp. 968–977, December 2012.

[12] J. Morren and S. W. H. de Haan, "Short-circuit current of wind turbines with doubly fed induction generator," *IEEE Transactions on Energy Conversion*, vol. 22, no. 1, pp. 174–180, March 2007.

[13] N. Mourad and B. Mohamed, "Short circuit current contribution of distributed photovoltaic integration on radial distribution networks," in *Proceedings of 2015 4th International Conference on Electrical Engineering*, Boumerdes, December 2015, pp. 1–4.

[14] E. Muljadi, N. Samaan, V. Gevorgian, J. Li, and S. Pasupulati, "Short circuit current contribution for different wind turbine generator types," in *Proceedings of 2010 IEEE Power and Energy Society General Meeting*, Minneapolis, MN, July 2010, pp. 1–8.

[15] G. Pannell, D. J. Atkinson, and B. Zahawi, "Analytical study of grid-fault response of wind turbine doubly fed induction generator," *IEEE Transactions on Energy Conversion*, vol. 25, no. 4, pp. 1081–1091, December 2010.

[16] F. Sulla, J. Svensson, and O. Samuelsson, "Symmetrical and unsymmetrical short-circuit current of squirrel-cage and doubly-fed induction generators," *Electric Power Systems Research*, vol. 81, no. 7, pp. 1610–1618, July 2011.

[17] H. Bao, S. Ying, and H. Schwarz, "Harmonic impact of decentralized photovoltaic systems and limitation of photovoltaic capacity in low voltage grid," in *Proceedings of 2014 14th International Conference on Environment and Electrical Engineering*, Krakow, May 2014, pp. 1–4.

[18] M. Bradt, B. Badrzadeh, E. H. Camm, D. Mueller, J. Schoene, T. Siebert, T. Smith, M. Starke, and R. Walling, "Harmonics and resonance issues in wind power plants," in *Proceedings of 2011 IEEE Power and Energy Society General Meeting*, Detroit, MI, July 2011, pp. 1–8.

[19] W. Chen, J. Xu, N. Zhu, C. Liu, M. Chen, and D. Xu, "Stator harmonic current suppression for DFIG wind power system under distorted grid voltage," in *Proceedings of 2012 3rd IEEE International Symposium on Power Electronics for Distributed Generation Systems*, Aalborg, June 2012, pp. 307–314.

[20] S. Djurovic and S. Williamson, "Influence of supply harmonic voltages on DFIG stator current and power spectrum," in *Proceedings of XIX International Conference on Electrical Machines*, Rome, September 2010, pp. 1–6.

[21] L. Fan, S. Yuvarajan, and R. Kavasseri, "Harmonic analysis of a DFIG for a wind energy conversion system," *IEEE Transactions on Energy Conversion*, vol. 25, no. 1, pp. 181–190, March 2010.

[22] S. Schostan, K.-D. Dettmann, T. D. Thanh, and D. Schulz, "Harmonic propagation in a doubly fed induction generator of a wind energy converter," in *Proceedings of 2009 Compatibility and Power Electronics*, Badajoz, May 2009, pp. 101–108.

[23] J. Tsai and K. Tan, "H APF harmonic mitigation technique for PMSG wind energy conversion system," in *Proceedings of 2007 Australasian Universities Power Engineering Conference*, Perth, WA, December 2007, pp. 1–6.

[24] *American National Standard for Electric Power Systems and Equipment–Voltage Ratings (60 Hz)*, ANSI C84.1-2011.

[25] *IEEE Recommend Practice for Utility Interface of Photovoltaic (PV) Systems*, IEEE Std. 929-2000.

[26] *IEEE Recommend Practice for Utility Interconnection of Small Wind Energy Conversion System*, IEEE Std. 1021-1998.

[27] *IEEE Standard for Interconnecting Distributed Resources with Electric Power System*, IEEE Std. 1547-2003.

[28] H. Li, V. Singhvi, A. Maitra, S. Rajagopalan, B. Enayati, S. Santoso, and R. Patterson, "Analysis of PV generation impacts on voltage imbalance and on voltage

regulation in distribution networks," in *Proceedings of 2014 IEEE Power and Energy Society General Meeting*, National Harbor, MD, July 2014, pp. 1–5.

[29] P. Wang, Z. Gao, and L. B. Tjernberg, "Operational adequacy studies of power systems with wind farms and energy storages," *IEEE Transactions on Power Systems*, vol. 27, no. 4, pp. 2377–2384, November 2012.

[30] S. Eftekharnejad, V. Vittal, G. T. Heydt, B. Keel, and J. Loehr, "Impact of increased penetration of photovoltaic generation on power systems," *IEEE Transactions on Power Systems*, vol. 28, no. 2, pp. 893–901, May 2013.

[31] ——, "Small signal stability assessment of power systems with increased penetration of photovoltaic generation: A case study," *IEEE Transactions on Power Systems*, vol. 28, no. 2, pp. 893–901, May 2013.

[32] K. Kawabe and K. Tanaka, "Impact of dynamic behavior of photovoltaic power generation systems on short-term voltage stability," *IEEE Transactions on Power Systems*, vol. 30, no. 6, pp. 3416–3424, November 2015.

[33] K. Coogan, M. J. Reno, S. Grijalva, and R. J. Broderick, "Locational dependence of PV hosting capacity correlated with feeder load," in *Proceedings of 2014 IEEE PES Transmission and Distribution Conference and Exposition*, Chicago, IL, April 2014, pp. 1–5.

[34] A. Hoke, R. Butler, J. Hambrick, and B. Kroposki, "Steady-state analysis of maximum photovoltaic penetration levels on typical distribution feeders," *IEEE Transactions on Sustainable Energy*, vol. 4, no. 2, pp. 350–357, April 2013.

[35] I. D. Margaris, J. C. Mantzaris, M. E. Karystianos, A. I. Tsouchnikas, C. D. Vournas, N. D. Hatziargyriou, and I. C. Vitellas, "Methods for evaluating pene-

tration levels of wind generation in autonomous systems," in *Proceedings of 2009 IEEE Bucharest Power Tech Conference*, Bucharest, Romania, June 2009, pp. 1–7.

[36] R. A. Shayani and M. A. G. de Oliveira, "Photovoltaic generation penetration limits in radial distribution systems," *IEEE Transactions on Power Systems*, vol. 26, no. 3, pp. 1625–1631, August 2011.

[37] B. H. Chowdhury and S. Chellapilla, "Double-fed induction generator control for variable speed wind power generation," *Electric Power Systems Research*, vol. 76, no. 9–10, pp. 786–800, June 2006.

[38] M. Fazeli, G. M. Asher, C. Klumpner, and L. Yao, "Novel integration of DFIG-based wind generators within microgrids," *IEEE Transactions on Energy Conversion*, vol. 26, no. 3, pp. 840–850, September 2011.

[39] P. Jahangiri and D. C. Aliprantis, "Distributed volt/var control by PV inverters," *IEEE Transactions on Power Systems*, vol. 28, no. 3, pp. 3429–3439, August 2013.

[40] A. Tapia, G. Tapia, J. X. Ostolaza, and J. R. Saenz, "Modeling and control of a wind turbine driven doubly fed induction generator," *IEEE Transactions on Energy Conversion*, vol. 18, no. 2, pp. 194–204, June 2003.

[41] B. H. Chowdhury, H. T. Ma, and N. Ardeshna, "The challenge of operating wind power plants within a microgrid framework," in *Proceedings of 2010 Power and Energy Conference at Illinois*, Urbana-Champaign, IL, February 2010, pp. 93–98.

[42] M. Fazeli, G. M. Asher, C. Klumpner, and L. Yao, "Novel integration of wind generator-energy storage systems within microgrids," *IEEE Transactions on Smart Grid*, vol. 3, no. 2, pp. 728–737, June 2012.

[43] N. P. W. Strachan and D. Jovcic, "Dynamic modelling, simulation and analysis of an offshore variable-speed directly-driven permanent-magnet wind energy conversion and storage system (WECSS)," in *Proceedings of OCEANS 2007-Europe*, Aberdeen, June 2007, pp. 1–6.

[44] R. Ahshan, M. T. Iqbal, G. K. I. Mann, and J. E. Quaicoe, "Micro-grid system based on renewable power generation units," in *Proceedings of 2010 23rd Canadian Conference on Electrical and Computer Engineering*, Calgary, AB, May 2010, pp. 1–4.

[45] R. Fadaeinedjad, G. Moschopoulos, and M. Moallem, "Using STATCOM to mitigate voltage fluctuations due to aerodynamic aspects of wind turbines," in *Proceedings of 2008 IEEE Power Electronics Specialists Conference*, Rhodes, June 2008, pp. 3648–3654.

[46] A. Jamshidi, M. M. Ghahderijani, and S. M. Barakati, "Power quality improvement in stand-alone microgrid including fixed-speed wind farm: Role of dynamic voltage restorer," in *Proceedings of 2012 11th International Conference on Environment and Electrical Engineering*, Venice, May 2012, pp. 206–211.

[47] N. R. Watson and J. Arrillaga, Eds., *Power Systems Electromagnetic Transients Simulation*. London: The Institution of Electrical Engineers, 2003.

[48] H. W. Dommel, "Digital computer solution of electromagnetic transients in single- and multiphase networks," *IEEE Transactions on Power Apparatus and Systems*, vol. 88, no. 4, pp. 388–399, April 1969.

[49] ——, *EMTP Theory Book*, 2nd ed. Vancouver: Microtran Power System Analysis Corporation, 1992.

[50] *User's Guide: A Comprehensive Resource for EMTDC*, Manitoba HVDC Research Centre, Manitoba, Canada.

[51] *User's Guide on the Use of PSCAD*, Manitoba HVDC Research Centre, Manitoba, Canada.

[52] R. C. Dugan, *Reference Guide: The Open Distribution System Simulator^{TM} (OpenDSS)*, Electric Power Research Institute, Inc., March 2016.

[53] *DIgSILENT PowerFactory User Manual*, DIgSILENT GmbH, Gomaringen, Germany, December 2014.

[54] J. J. Grainger and W. D. Stevenson, Jr., *Power System Analysis*. New York: McGraw-Hill, 1994.

[55] G. W. Stagg and A. H. El-Abiad, *Computer Methods in Power System Analysis*. New York: McGraw-Hill, 1968.

[56] W. I. Bowman and McNamee, "Development of equivalent Pi and T matrix circuits for long untransposed transmission lines," *IEEE Transactions on Power Apparatus and Systems*, vol. 83, no. 6, pp. 625–632, June 1964.

[57] W. H. Kersting, *Distribution System Modeling and Analysis*, 3rd ed. Florida: CRC Press, 2012.

[58] R. C. Dugan, "A perspective on transformer modeling for distribution system analysis," in *Proceedings of 2003 IEEE Power Engineering Society General Meeting*, Toronto, ON, July 2003, pp. 114–119.

[59] R. C. Dugan and S. Santoso, "An example of 3-phase transformer modeling for distribution system analysis," in *Proceedings of 2003 IEEE PES Transmission and Distribution Conference and Exposition*, Dallas, TX, September 2003, pp. 1028–1032.

[60] J. Arrillaga and B. Smith, Eds., *AC-DC Power System Analysis*. London: The Institution of Electrical Engineers, 1998.

[61] P. C. Krause, O. Wasynczuk, S. D. Sudhoff, and S. Pekarek, *Analysis of Electric Machinery and Drive Systems*, 3rd ed. New Jersey: IEEE Press, 2013.

[62] C.-M. Ong, *Dynamic Simulation of Electric Machinery Using Matlab/Simulink*. New Jersey: Prentice Hall, 1997.

[63] T. Ackermann, Ed., *Wind Power in Power System*. Chichester: Wiley, 2005.

[64] E. H. Camm, M. R. Behnke, O. Bolado, M. Bollen, M. Bradt, C. Brooks, W. Dilling, M. Edds, W. J. Hejdak, D. Houseman, S. Klein, J. Li, F. Li, P. Maibach, T. Nicolai, J. Patio, S. V. Pasupulati, N. Samaan, S. Saylors, T. Siebert, T. Smith, M. Starke, and R. Walling, "Characteristics of wind turbine generators for wind power plants," in *Proceedings of 2009 IEEE Power and Energy Society General Meeting*, Calgary, AB, July 2009, pp. 1–5.

[65] G. M. Masters, *Renewable and Efficient Electric Power Systems*, 2nd ed. New Jersey: Wiley, 2013.

[66] B. Wu, Y. Lang, N. Zargari, and S. Kouro, *Power Conversion and Control of Wind Energy Systems*. New Jersey: Wiley, 2011.

[67] J. F. Manwell, J. G. McGowan, and A. L. Rogers, *Wind Energy Explained: Theory, Design and Application*, 2nd ed. Chichester: Wiley, 2010.

[68] M. R. Patel, *Wind and Solar Power Systems: Design, Analysis, and Operation*, 2nd ed. Florida: CRC Press, 2006.

[69] F. M. Vanek, L. D. Albright, and L. T. Angenent, *Energy Systems Engineering: Evaluation and Implementation*, 2nd ed. New York: McGraw-Hill, 2012.

[70] P. Kundur, *Power System Stability and Control*. New York: McGraw-Hill, 1994.

[71] J. W. Smith, R. C. Dugan, and W. Sunderman, "Distribution modeling and analysis of high penetration PV," in *Proceedings of 2011 IEEE Power and Energy Society General Meeting*, Detroit, MI, July 2011, pp. 1–7.

[72] W. Sunderman, R. C. Dugan, and J. W. Smith, "Open source modeling of advanced inverter functions for solar photovoltaic installations," in *Proceedings of 2014 IEEE PES Transmission and Distribution Conference and Exposition*, Chicago, IL, April 2014, pp. 1–5.

[73] R. C. Dugan, W. Sunderman, and B. Seal, "Advanced inverter controls for distributed resources," in *Proceedings of 22nd International Conference and Exhibition on Electricity Distribution*, Stockholm, June 2013, pp. 1–4.

[74] J. W. Smith, W. Sunderman, R. C. Dugan, and B. Seal, "Smart inverter volt/var control functions for high penetration of PV on distribution systems," in *Proceedings of 2011 IEEE PES Power Systems Conference and Exposition*, Phoenix, AZ, March 2011, pp. 1–6.

[75] J. W. Smith, B. Seal, W. Sunderman, and R. C. Dugan, "Simulation of solar generation with advanced volt-var control," in *Proceedings of 21st International Conference and Exhibition on Electricity Distribution*, Frankfurt, June 2011, pp. 1–4.

[76] A. Mki, S. Valkealahti, and T. Suntio, "Dynamic terminal characteristics of a photovoltaic generator," in *Proceedings of 2010 14th International Power Electronics and Motion Control Conference*, Ohrid, September 2010, pp. T12–76–T12–80.

[77] J. Puukko, T. Messo, and T. Suntio, "Effect of photovoltaic generator on a typical VSI-based three-phase grid-connected photovoltaic inverter dynamics," in *Proceedings of 2011 IET Conference on Renewable Power Generation*, Edinburgh, September 2011, pp. 1–6.

[78] *IEEE 4 Node Test Feeder*, IEEE PES DSASC Test Feeder Working Group, September 2006.

[79] R. C. Dugan, "Experiences with the center-tapped wye-delta transformer test case," in *Proceedings of 2004 IEEE Power Engineering Society General Meeting*, Denver, CO, June 2004, pp. 867–871.

[80] *4 Node Test Feeder: Experiences with the Center-Tapped Wye-Delta Transformer Test Case*, IEEE PES DSASC Test Feeder Working Group, June 2004.

[81] *IEEE Wye-Delta Center Tapped Transformer Test Feeder*, IEEE PES DSASC Test Feeder Working Group, November 2004.

[82] S. Santoso and R. C. Dugan, "Experiences with the new open-wye/open-delta transformer test cases for distribution system analysis," in *Proceedings of 2005 IEEE Power Engineering Society General Meeting*, San Francisco, CA, June 2005, pp. 884–889.

[83] Western Wind Resources Dataset. National Renewable Energy Laboratory. [Online]. Available: http://wind.nrel.gov/Web_nrel/.

[84] Smart Grid Resource Center: Simulation Tool–OpenDSS. Electric Power Research Institute. [Online]. Available: http://smartgrid.epri.com/SimulationTool.aspx.